Dottorato in Fisica
Dipartimento di Fisica e Chimica
FIS-03

Strong field phenomena: Atoms, Molecules and Nanostructures

IL DOTTORE
Biagio Frusteri

IL COORDINATORE
Prof. Gioacchino Massimo Palma

IL TUTOR
Prof. Emilio Fiordilino

CICLO XXX
ANNO CONSEGUIMENTO TITOLO 2018

Strong field phenomena: Atoms, Molecules, Nanostructures

Biagio Frusteri

Dipartimento di Fisica e Chimica
Via Archirafi 36
90123 Palermo

Università degli studi di Palermo

A thesis submitted for the degree of

Doctor of Phylosophy

February 2018

Contents

Glossary

ALDA	Adiabatic local-density approximation 108
ARPES	Angular resolved photoelectron spectrum 27, 58, 115, 116, 118, 119, 121
ATI	Above threshold ionization 13, 15, 17, 18, 19, 20, 22, 24, 115
CCD	Charge-coupled device 104
CF_3I	Trifluoromethyl iodide 69, 71, 104, 105, 107, 108, 111, 115, 131, 132
DFT	Density functional theory 33, 51, 67, 69, 71
ELSEPA	Elastic electron-atom scattering code 111
FHI	Fritz-Haber Institute 108
HEG	Homogeneous electron gas 45, 67, 69, 71
HHG	High harmonic generation 5, 13, 18, 19, 20, 22, 24, 73, 123, 129, 130, 131, 133
HOMO	Highest occupied molecular orbital 30, 67, 69, 71, 107, 108, 109, 111, 115, 119, 120, 121, 122, 131, 132
LDA	Local density approximation 45, 67, 69, 71
LIED	Laser induced electron diffraction technique 104, 132
MPI	Multiphoton ionization 13, 14, 24
o.c.	Optical cycles 77, 80, 86, 83, 84, 86
OCS	Carbonyl sulfide 67, 69, 71, 115, 123, 132, 133

PAD	Photoelectron angular distribution 13, 28, 30, 104, 105, 106, 107, 109, 111, 115, 118, 119, 120, 122, 131, 132
PES	Photoelectron spectum 121, 132
QR	Quantum Ring 66, 95, 98, 99, 133
QRT	Quantitative rescattering theory 25, 27, 28, 71, 104, 111
RG	Runge-Gross 51, 54, 55
SAE	Single active electron 14, 20, 31, 33, 121, 122
SFA	Strong field approximation 15, 16, 17, 23
SFA2	Strong field approximation 2 15, 23
SFI	Strong field ionization 33, 51, 61
SIC	Self-interacting corretion 67, 69, 71, 108
SQR	Structured quantum ring 34, 36, 50, 62, 72, 80, 129, 130, 133
TD	Time dependent 51, 55
TDDFT	Time dependent density functional theory 50, 54, 58, 104, 108, 109, 111, 116, 119, 121, 122, 123, 132
TDSE	Time dependent Schroedinger equation 15, 19, 20, 22, 24, 33, 59, 77, 80, 105
TISE	Time independent Schroedinger equation 14, 15, 28, 30, 31, 33, 34, 41, 44, 80, 130
VMI	Velocity map imaging 104, 108

This thesis is dedicated to my grand-parents which watch over me from here and from up there and to my parents for all the sacrifices they made for my studies.

Acknowledgements

I would like to thank Professor Emilio Fiordilino to be a mentor to me and for all his advice. I wish to express my sincere gratitude to Professor Angel Rubio for providing me the oppurtunity to work with the ETFS, Nanobio spectroscopy group in Donostia San Sebastian. I sincerely thank Dr. Umberto De Giovannini and Dr. Philipp Woppeper for their guidance, help and suggestions in the Multiple Orbital Photoelectron Angular distribution project. And finally, the University of Palermo that gave me the possibility to spent 6 months working in Donostia.

1

Introduction

Scientists and scientific research have been guided by imagination and curiosity since the beginning. When we think about the fathers of the modern science, the first images, that we see in our mind, are the pictures of Newton and Galileo. As a matter of fact, the history of scientific knowledge started when the first man, looking at the constellations, imagined animals and objects. Nowadays, the questions to be answered by scientists are many, admittedly the more phenomena we understand the more open questions we find.

The idea of relating the motion of the smallest part of the matter with macroscopic properties has been fascinating since the time of Ancient Greece. Understanding the electronic motion and seeing its signatures in quantities that we can measure was unthinkable only 200 years ago, and now there are many sectors of scientific research focused on it. One of this is the Strong Field area, in other words the branch of physics which analyses the interactions between atoms, molecules, clusters, nanostructures and strong electric fields.

It has been a long road since Einstein formulated the theoretical basis of the *light amplification by stimulated emission of radiation* (laser), indeed the state of art allows the realisation of attosecond and femtosecond laser with very high intensities ($10^{10} \leftrightarrow 10^{17}$ $\mathrm{W/cm^2}$). The need of having laser with this duration is due to the fact that attoseconds and femtoseconds are the timescales of electronic and nuclear motion. At the same time, a high intensity permits to study nonlinear phenomena of matter-radiation interaction such as: above threshold ionization (ATI), multiphoton ionization (MPI), rescattering, high harmonic generation (HHG). By looking at each of this phenomena we are able to study different properties of the target system. For example, we are able to reconstruct the atomic and molecular orbitals, to know the ionization energies of molecules, ions and atoms, to study the symmetry of a target system, the motion of electrons and ions [1, 2, 3, 4, 5, 6, 7, 8, 9].

The aim of this thesis is the study of these phenomena by using various systems as targets. We are going to analyse in particular: HHG spectra from atoms, molecules and quantum rings and the dual process photoelectron angular distribution (PAD). In the study of the latter, we will distinguish features of different phenomena as, in the low energy region, ATI and MPI and in the high energy part, rescattering.

1.1 Multiphoton Ionization

When a target system is driven by a weak laser field, a bounded electron can absorb a photon. At a later time, it might go into a virtual state and later come back into a bound state or, if the photon energy $\hbar\omega_L$ is higher than the ionization energy I_p, it will run away. This phenomenon is named photoelectric effect and it is shown in Fig.1.1.

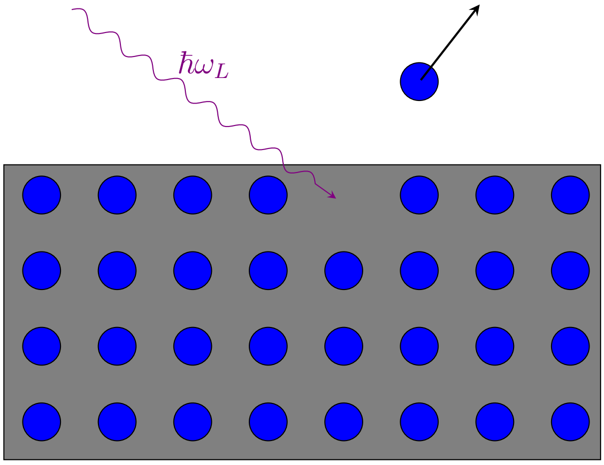

Figure 1.1: Picture of the photoelectric effect (photon in violet, electrons in blue).

On the other hand, when the probability of ionization is high, we are in the presence of a strong laser field and our bounded electron can absorb more than one photon and ionize also if $\hbar\omega_L < I_p$. This phenomenon is named MPI.

A bounded electron in a target is described by the time independent Schroedinger equation (TISE):

$$\mathbb{H}\,|\phi\rangle = E\,|\phi\rangle\,. \tag{1.1}$$

If we solve Eq. 1.1 for the groundstate $|\phi_0\rangle$, we find the eigenenergy E_0 that by definition is $E_0 = -I_p$. There are many ways and many levels of approximation that can be used to solve this equation. For explaining some aspects of MPI (Fig. 1.2), we do not need to use many body models thus we may safely consider that we have only one electron in the presence of a mean potential field due to the other particles in the system. This approach is named single active electron (SAE) approximation and in what follows we will use this approximation many times.

The standard approach for building $\mathbb{H}$ is to reproduce some experimental properties. For the purposes of this work, we mainly take into account the geometry and the ionization energy of the system. The former is very important in recollision processes, on the other hand the latter is essential for a good understanding of the ionization one. Note, in order to study our target systems, we consider laser field, thus we include in

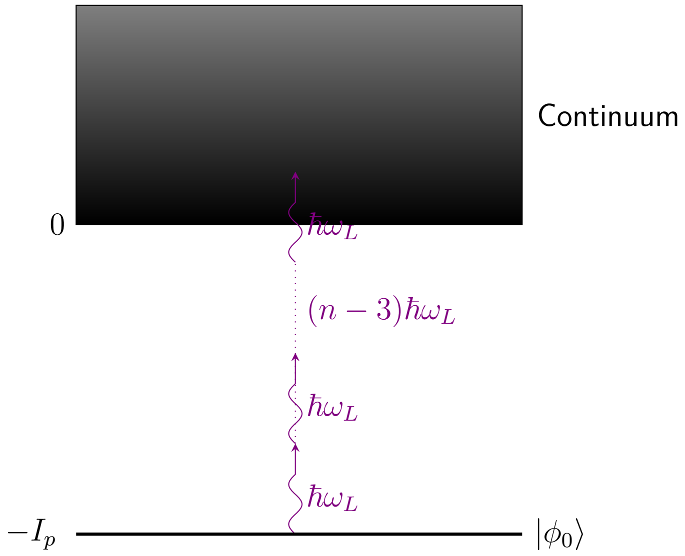

Figure 1.2: Picture of the MPI process, from the ground state to the continuum.

the equations the contribution of periodic electric field $\vec{\mathcal{E}}(t)$ or vector potential $\vec{\mathcal{A}}(t)$:

$$\vec{\mathcal{E}}(t) = f(t)(\mathcal{E}_x \cos(\omega_L t), \mathcal{E}_y \sin(\omega_L t)) \rightarrow (\mathcal{E}_x \cos(\omega_L t), \mathcal{E}_y \sin(\omega_L t)) \tag{1.2}$$

$$\vec{A}(t) = f(t)(A_x \sin(\omega_L t), A_y \cos(\omega_L t)) \rightarrow (A_x \sin(\omega_L t), A_y \cos(\omega_L t)) \tag{1.3}$$

where the choice of the sinusoidal functions is arbitrary (it is only important that if $\mathcal{E}_i(t) \propto \cos(\omega_L t)$ then $\mathcal{E}_j(t) \propto \sin(\omega_L t)$, with $i = x, y$; $j = x, y$ and $i \neq j$). In the set of Eq.s 1.2 and 1.3 $f(t)$, called pulse profile, describes the on and off switching of the laser pulse; it fulfills the condition: $\lim_{t\to\pm\infty} f(t) = 0$ and $\max f(t) = 1$. It is important to note that we are neglecting the dependence, of the fields in Eq.s 1.2 and 1.3, on the space position $\vec{r}$, this approach is generally named dipole approximation, in the following we will use it several times.

1.2 Above threshold ionization.

If we look the experimental photoelectron spectrum for small energies (in the following we are going to explain what this means), we observe the multiphoton phenomenon named ATI. One of the first explanation of this experimental effect was the Keldysh theory [10], which, as initially formulated, was perturbative and not easy to correct with higher order of approximation. On the other hand, this theory is still used for explaining the ATI phenomenon and nowadays there is an expansion of this theory named strong field approximation (SFA2), that is able to explain also the recollision processes. For our purpose in this section, we only need to derive the Keldysh lowest-order theory from the time dependent Schroedinger equation (TDSE), in the future we are going to call this SFA. We assume that the Hamiltonian describing the unperturbed system can be written in the form:

$$\mathbb{H}_0 = \frac{\mathbb{p}^2}{2m_e} + \mathbb{V}(\vec{r}) \tag{1.4}$$

and that $|\phi\rangle$ is a generic eigenstate of the associated TISE (Eq. 1.1). If the Hamiltonian $\mathbb{H}_I(t)$ describes the interaction between a strong laser field and our system, we can write the TDSE:

$$\mathbb{H}\left|\psi(t)\right\rangle = i\hbar\frac{\partial}{\partial t}\left|\psi(t)\right\rangle \tag{1.5}$$

$$\mathbb{H} = \mathbb{H}_0 + \mathbb{H}_I(t) \tag{1.6}$$

$$\left|\psi(t)\right\rangle = \sum_n c_n(t)\left|\phi_n\right\rangle + \int \mathrm{d}^3\vec{k}c_{\vec{k}}(t)\left|\phi_{\vec{k}}\right\rangle; \tag{1.7}$$

where we used the dipole approximation and the state vector $|\psi(t)\rangle$ is written as an expansion of $|\phi_n\rangle$, where the first contribution is from the bound states and the second from the continuum states [11, 12].

Inserting Eq. 1.7 in Eq. 1.5 and projecting to $\langle\phi_n|$ and $\langle\phi_k|$, we get the following coupled equations:

$$i\hbar\frac{\partial c_n(t)}{\partial t} = E_n c_n(t) + \sum_m \left\langle\phi_n\right|\mathbb{H}_I(t)\left|\phi_m\right\rangle c_m(t) + \\ + \int \mathrm{d}^3\vec{k}\left\langle\phi_n\right|\mathbb{H}_I(t)\left|\phi_{\vec{k}}\right\rangle c_{\vec{k}}(t) \tag{1.8}$$

$$i\hbar\frac{\partial c_{\vec{k}}(t)}{\partial t} = E_{\vec{k}}c_{\vec{k}}(t) + \sum_m \left\langle\phi_{\vec{k}}\right|\mathbb{H}_I(t)\left|\phi_m\right\rangle c_m(t) + \\ + \int \mathrm{d}^3\vec{k}'\left\langle\phi_{\vec{k}}\right|\mathbb{H}_I(t)\left|\phi_{\vec{k}'}\right\rangle c_{\vec{k}'}(t). \tag{1.9}$$

In order to derive the SFA we have to impose three condition:

1. the probability amplitude of the initial bound state is close to one during the interaction

2. the binding potential $\mathbb{V}(\vec{r})$ is short ranged (its effect is negligible for ionized electrons)

3. $\mathbb{H}_I = -\frac{q_e}{m_e c}\vec{\mathbb{A}}(t)\cdot\vec{\mathbb{p}} + \frac{q_e^2}{2m_e c^2}\mathbb{A}^2(t) \to -\frac{q_e}{m_e c}\vec{\mathbb{A}}(t)\cdot\vec{\mathbb{p}}$, where we neglect the $\mathbb{A}^2(t)$-term because the addition of a function depending only on time to an Hamiltonian does not change the physics properties, and q_e is the charge of the electron.

From condition (2), it derives that the state $|\phi_k\rangle$ is an eigenstate of $\mathbb{p}$, thus $|\phi_k\rangle = |\vec{p}\rangle$. Then, we are only interested to Eq. 1.9 and the contributions become:

$$\left\langle\phi_{\vec{k}}\right|\mathbb{H}_I(t)\left|\phi_m\right\rangle \to \left\langle\vec{p}\right|\mathbb{H}_I(t)\left|\phi_m\right\rangle = -\frac{q_e}{m_e c}\vec{A}(t)\cdot\vec{p}\left\langle\vec{p}\right|\left.\phi_m\right\rangle = H_I(t)\phi_m(\vec{p}) \tag{1.10}$$

$$\int \mathrm{d}^3\vec{k}'\left\langle\phi_{\vec{k}}\right|\mathbb{H}_I(t)\left|\phi_{\vec{k}'}\right\rangle c_{\vec{k}'}(t) \to \int \mathrm{d}^3\vec{p}\left\langle\vec{p}\right|\mathbb{H}_I(t)\left|\vec{p}'\right\rangle c_{\vec{p}'} = \\ = \int \mathrm{d}^3\vec{p}\delta_{\vec{p},\vec{p}'}H_I(t)c_{\vec{p}'} = H_I(t)c_{\vec{p}}. \tag{1.11}$$

With this approximations Eq. 1.9 takes the form of

$$i\hbar\frac{\partial c_{\vec{p}}(t)}{\partial t} \cong \left[\frac{p^2}{2m_e} + H_I(t)\right] c_{\vec{p}}(t) + \sum_m H_I(t)\phi_m(\vec{p})c_m(t) \tag{1.12}$$

and if we consider $c_{\vec{p}}(0) = 0$ and we neglect a phase factor depending of t which is not relevant from a physics point of view, we can write as approximated solution:

$$c_{\vec{p}}(t) \cong -\frac{i}{\hbar}\sum_m \phi_m(\vec{p}) \int_0^t \mathrm{d}\tau H_I(\tau)c_m(\tau)e^{\frac{i}{\hbar}\left[\frac{p^2\tau}{2m_e}+\int_0^\tau \mathrm{d}t' H_I(t')\right]}. \tag{1.13}$$

By partial integration and dropping the not integral term that is always bounded during the interaction, we find

$$c_{\vec{p}}(t) \cong \frac{i}{\hbar}\sum_m \phi_m(\vec{p}) \int_0^t \mathrm{d}\tau e^{\frac{i}{\hbar}\int_0^\tau \mathrm{d}t' H_I(t')} \frac{\mathrm{d}}{\mathrm{d}\tau}\left[c_m(\tau)e^{\frac{i}{\hbar}\frac{p^2\tau}{2m_e}}\right]. \tag{1.14}$$

From condition (1), it follows that $c_m(t) \cong \delta_{im}e^{i\frac{I_i t}{\hbar}}$ (where $m = i$ denotes the initial state and $I_i = -E_i$) and that

$$c_{\vec{p}}(t) \cong \frac{i}{\hbar}\phi_i(\vec{p})\left(\frac{p^2}{2m_e} + I_i\right) \int_0^t \mathrm{d}\tau e^{\frac{i\tau}{\hbar}\left[\frac{p^2}{2m_e}+I_i+\frac{1}{\tau}\int_0^\tau \mathrm{d}t' H_I(t')\right]}. \tag{1.15}$$

At this point, we can calculate the angular distribution of energy for ionized electrons with momentum between $\vec{p}$ and $\vec{p} + \mathrm{d}\vec{p}$ [5] as function of the energy

$$\boldsymbol{\nabla}_{\vec{p}} I = |f(\vec{p})|^2 \tag{1.16}$$

where

$$f(\vec{p}) = c_{\vec{p}}(\infty) - c_{\vec{p}}(-\infty). \tag{1.17}$$

The integral term of Eq. 1.15 inserted into Eq. 1.16 and integrated over $\mathrm{d}^3\vec{p}$, for a periodic potential, is the energy spectrum of photoelectrons, which consequently has peaks at:

$$\frac{p^2}{2m_e} = n\hbar\omega_L - I_i - U_p \tag{1.18}$$

$$U_p = \frac{1}{\tau}\int_0^\tau \mathrm{d}t' \frac{q_e^2}{2m_e c^2}A^2(t') \tag{1.19}$$

where U_p is the ponderomotive energy, and $n\hbar\omega_L$ is the multiphoton terms. These peaks are historically named ATI [10, 11, 13, 14, 12]. To be thorough, in the standard SFA Eq. 1.13 is written as

$$c_{\vec{p}}(t) = -\frac{i}{\hbar}\int_0^t \mathrm{d}\tau \left\langle \psi_V^{\vec{p}}(\tau)\right| H_I(\tau) \left|\psi_D(\tau)\right\rangle \tag{1.20}$$

$$\left|\psi_V^{\vec{p}}(\tau)\right\rangle = e^{-\frac{i\tau}{\hbar}\left(\frac{p^2}{2m_e}+\int_0^\tau \mathrm{d}t' H_I(t')\right)} \left|\vec{p}\right\rangle \tag{1.21}$$

$$\left|\psi_D(\tau)\right\rangle = \sum_m c_m(t)\left|\phi_m\right\rangle \tag{1.22}$$

where $|\psi_V^p(\tau)\rangle$ are named Volkov states, $|\phi_i\rangle = |\phi_0\rangle$ and consequently $I_i = I_p$.

At this point, we have to explain what small energies means. For this aim, we evaluate the classical counterpart of our system. For an ionized electron driven by a vector potential $\vec{A}(t)$, such as $\langle \vec{A}(t)\rangle_{T_L} = 0$, the classical velocity is

$$m\vec{v}(t) = \frac{q_e}{c}\left[\vec{A}(t_0) - \vec{A}(t)\right] = \vec{p} - \frac{q_e}{c}\vec{A}(t) \tag{1.23}$$

where $\vec{p}$ is the momentum at the time of ionization t_0. Thus, the average kinetic energy is

$$\frac{m_e}{2}\langle \vec{v}^2(t)\rangle_{T_L} = \frac{p^2}{2m_e} + \frac{q_e^2}{2m_e c^2}\langle A^2(t)\rangle_{T_L} = E_{drift} + U_p. \tag{1.24}$$

Generally, we have an elliptical polarized incident electric field and the $\vec{A}(t)$ can be written as

$$\vec{A}(t) = \frac{A}{1+e^2}\left[\hat{x}\sin(\omega_L t) + e\hat{y}\cos(\omega_L t)\right] \tag{1.25}$$

where e is the ellipticity and $A^2 = \frac{4m_e c^2 U_p}{q_e^2}$. With this ansatz

$$\begin{aligned} E_{drift} = \frac{(q_e\vec{A}(t_0))^2}{2m_e c^2} = \frac{q_e^2 A^2}{2m_e c^2}\left[\cos^2(\omega_L t_0) + e^2\sin^2(\omega_L t_0)\right] = \\ = 2\frac{q_e^2 A^2}{4m_e c^2}\left[1 + (e^2-1)\sin^2(\omega_L t_0)\right] \end{aligned} \tag{1.26}$$

$$\frac{2e^2}{1+e^2}U_p \leq E_{drift} \leq \frac{2}{1+e^2}U_p, \tag{1.27}$$

this result means that for linear polarized laser the ATI process should happen between 0 and $2U_p$.

In conclusion, when an atom or a molecule is driven by a strong laser field, the photoelectron spectrum, in the energy range $0 \to 2U_p$, presents peaks at $\frac{p^2}{2m_e} = -I_i - U_p + n\hbar\omega_L$ named ATI.

1.3 High Harmonic Generation.

Since the first experiments in which HHG was observed, researchers have been fascinated by the possibility to utilize this coherent form of emission to develop new laser. The very peculiar characteristics of HHG, in particular the fact that it is sensitive to the symmetry of the system, allow to control the properties of the emission (such as ellipticity or time duration). Of course this control it is not easy for technical limitations in the experiment.

But, what is HHG? An atom, molecule, cluster or nanostructure, driven by an intense laser field of frequency ω_L, emits a spectrum formed by multiples of ω_L. If the target system has spherical symmetry, it only emits odd harmonics, otherwise the spectrum is composed by both even and odd harmonics. In a typical HHG spectrum the intensity of the first few harmonics rapidly decreases, later remains constant along a wide plateau and then rapidly quenches in a rapid cutoff; as reported in literature, the study of the cutoff region is important for the realization of short pulse.

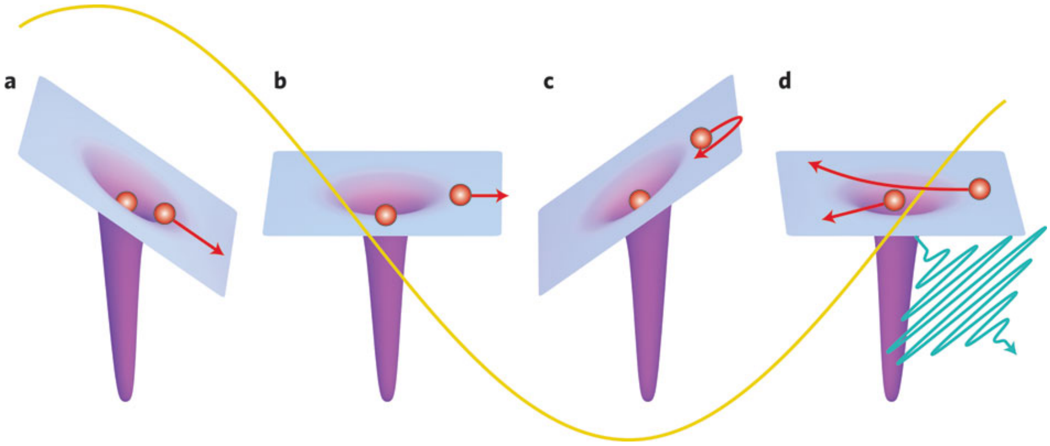

Figure 1.3: Picture of the three step model.

This phenomenon is historically explained by the three step model. The difference between the treatment of ATI and HHG is that, for the latter we have to consider the contribution of the returning electrons.

The idea of the three step model is pictorially given in (Fig.1.3): (a) a bounded electron goes to the continuum by tunneling; (b) it is accelerated by the laser field; (c) when the laser field changes sign the electron can come back close to the target system; (d) it can rescatter changing is momentum, or it can be recaptured into a bound state emitting harmonic radiation.

In the remaining part of this thesis, we will solve the TDSE to calculate the evolution of a system driven by an intense laser. However, in this section we want to explain in a easy way some characteristics of HHG, thus we use two simplified approaches.

The first one is named semi-classical and it is based on the three step model. The idea is that the active electron appears in the continuum with zero velocity ($v(t_i) = 0$ where t_i is the ionization time). In analogy with the ATI process we treat this electron classically [15, 16, 17, 18].

The equation of motion for an electron driven by a laser field linearly polarized along the $\hat{x}$-axis, is

$$ma_x(t) = -q_e\mathcal{E}_0 \sin(\omega_L t) \tag{1.28}$$

and the velocity is

$$v_x(t) = \frac{q_e\mathcal{E}_0}{m\omega_L}\left[\cos\left(\omega_L t\right) - \cos\left(\omega_L t_i\right)\right]. \tag{1.29}$$

At this point we have to find the second time of this process, the rescattering or capture time t_r, in other words a time $t_r \neq t_i$ such that $x(t_r) = 0$. From Eq. 1.29

$$x(t) = \frac{q_e \mathcal{E}_0}{m\omega_L^2} \left[\sin{(\omega_L t)} - \sin{(\omega_L t_i)} - \omega_L (t - t_i) \cos{(\omega_L t_i)} \right] \tag{1.30}$$

thus the rescatting times t_r must satisfy

$$\sin{(\omega_L t_r)} - \sin{(\omega_L t_i)} = \omega_L (t_r - t_i) \cos{(\omega_L t_i)}. \tag{1.31}$$

At the same way of the maximum energy for the ATI process we can estimate the cutoff of HHG. In this model, the energy of an emitted photon is

$$\hbar\omega = \Delta E_k + I_p \tag{1.32}$$

where

$$\Delta E_k = \frac{1}{2} m v_x(t_r)^2 - \frac{1}{2} m v_x(t_i)^2 = \frac{1}{2} m v_x(t_r)^2 \tag{1.33}$$

by simulations it has been found that the maximum value of $\Delta E_k = 3.2U_p$, thus

$$\hbar\omega_{cut} = 3.2U_p + I_p. \tag{1.34}$$

The second approach is the quasi-classical method [19] which starts from a full quantum theory. If we have an atom driven by a periodic electric field, the TDSE is:

$$i\frac{\partial}{\partial t} |\psi(\vec{r}, t)\rangle = \left[-\frac{\hbar^2 \nabla^2}{2m_e} + \mathbb{V}(\vec{r}) - q_e \vec{\mathcal{E}} \cdot \vec{r} \cos{(\omega_L t)} \right] |\psi(\vec{r}, t)\rangle \tag{1.35}$$

where Eq. 1.35 is written in the so called length gauge within the SAE. For our goal, we need that $I_p >> \hbar\omega_L$ (most of the time $I_p \approx (5 \to 20)\hbar\omega_L$) and U_p comparable with I_p. In this way the electron that leaves the atom does not feel the atomic potential $\mathbb{V}(\vec{r})$. In addition, we are interested to study the emission in the cutoff region. The electrons responsible of this part of the spectrum have a great kinetic energy compared with the ionization potential. A general solution of Eq. 1.35 is still the one in Eq. 1.7. If we are in the energy range where $\gamma = \sqrt{\frac{I_p}{2U_p}} < 1$ (γ is named Keldysh parameters), we have to consider only the contribution of the groundstate $|\phi_0\rangle$ and we have to use the assumptions (1) and (2) of section 1.2, thus

$$|\psi(t)\rangle = e^{i\hbar I_p t} c_0(t) |\phi_0\rangle + \int \mathrm{d}^3\vec{p} c_{\vec{p}}(t) |\vec{p}\rangle. \tag{1.36}$$

As in section 1.2, we insert this solution in Eq. 1.35, considering for simplicity a linear polarized laser along x

$$i\hbar \frac{\partial c_{\vec{p}}(t)}{\partial t} = \left[\frac{\vec{p}^2}{2m_e} + I_p \right] c_{\vec{p}}(t) - q_e \mathcal{E}_0 \cos{(\omega_L t)} \left[\langle \vec{p}| \mathbb{x} |\phi_0\rangle + i\frac{\partial}{\partial p_x} c_{\vec{p}}(t) \right] \tag{1.37}$$

and the general solution (where $\vec{p} = m_e\vec{v}$) is

$$c_{\vec{p}}(t) = iq_e \int_0^t \mathrm{d}t' \mathcal{E}_0 \cos(\omega_L t') \left\langle \vec{p} + \frac{q_e}{c}\vec{A}(t) - \frac{q_e}{c}\vec{A}(t') \middle| \mathbb{x} \middle| \phi_0 \right\rangle \times \\ \times e^{-i\int_{t'}^{t} \mathrm{d}t'' \left[\frac{\left(\vec{p} + \frac{q_e}{c}\vec{A}(t) - \frac{q_e}{c}\vec{A}(t'')\right)^2}{2m_e} + I_p \right]}. \tag{1.38}$$

The energy emitted from ω and $\omega + \mathrm{d}\omega$ that it is given by the Larmour formula

$$\frac{\mathrm{d}I}{\mathrm{d}\omega}(\omega) = \frac{4q_e^2}{3c^3}|\vec{a}(\omega)|^2. \tag{1.39}$$

where $\vec{a}(\omega)$ is the Fourier transform of $\vec{a}(t) = \left\langle \psi(t) \middle| \frac{\partial^2}{\partial t^2}\vec{r} \middle| \psi(t) \right\rangle$.

The x-component of the dipole moment $\vec{r}(t) = \langle \psi(t) | \vec{r} | \psi(t) \rangle$ using our expansion of $|\psi(t)\rangle$ is

$$x(t) = i \int_0^t \mathrm{d}t' \int \mathrm{d}^3\vec{P} \mathcal{E}_0 \cos(\omega_L t') \left\langle \vec{P} - \frac{q_e}{c}\vec{A}(t') \middle| \mathbb{x} \middle| \phi_0 \right\rangle \left\langle \phi_0 \middle| \mathbb{x} \middle| \vec{P} - \frac{q_e}{c}\vec{A}(t') \right\rangle \times \\ \times e^{-i\int_{t'}^{t} \mathrm{d}t'' \left[\frac{\left(\vec{P} - \frac{q_e}{c}\vec{A}(t'')\right)^2}{2m_e} + I_p \right]} + c.c. \tag{1.40}$$

where $\vec{P} = \vec{p} + \frac{q_e}{c}\vec{A}$ is the canonical momentum. In spite of its complicated look, the physical meaning of this equation is very clear.

- $\mathcal{E}_0 \cos(\omega_L t') \left\langle \vec{P} - \frac{q_e}{c}\vec{A}(t') \middle| \mathbb{x} \middle| \phi_0 \right\rangle$ is the probability amplitude for an electron to go to the continuum at time t' with canonical momentum $\vec{P}$
- $\int_{t'}^{t} \mathrm{d}t'' \left[\frac{\left(\vec{P} - \frac{q_e}{c}\vec{A}(t'')\right)^2}{2m_e} + I_p \right]$ is the quasi-classical action $S(\vec{P}, t, t')$, and describes the interaction between the free electron and the laser field in the time interval $t' \to t$
- $\left\langle \phi_0 \middle| \mathbb{x} \middle| \vec{P} - \frac{q_e}{c}\vec{A}(t') \right\rangle$ is the probability amplitude of recombination at time t

One important consideration is that the canonical momentum $\vec{P}$ does not change between t and t' because we neglected the contribution of $\mathbb{V}(\vec{r})$ in the continuum (actually this in not completely true because of the dependence of $S(\vec{P}, t, t')$ on I_p).

The generalization of this solution to the case with a $\vec{\mathcal{E}}(t)$ with a generic polarization, is trivial

$$\vec{r}(t) = i \int_0^t \mathrm{d}t' \int \mathrm{d}^3\vec{P} \left\langle \phi_0 \middle| \mathbb{r} \middle| \vec{P} - \frac{q_e}{c}\vec{A}(t') \right\rangle \vec{\mathcal{E}}(t') \cdot \left\langle \vec{P} - \frac{q_e}{c}\vec{A}(t') \middle| \mathbb{r} \middle| \phi_0 \right\rangle \times \\ \times e^{-iS(\vec{P}, t, t')} + c.c.. \tag{1.41}$$

$S(\vec{P}, t, t')$ varies much faster than the dipole matrix elements, thus the most important contribution to the integral comes from:

$$\boldsymbol{\nabla}_p S(\vec{P}, t, t') = 0. \tag{1.42}$$

As we expected from the semi-classical models, we find by Eq. 1.42 that the most important contributions come from electrons which come back at t at the same position where they started at t'. In addition, we only consider the possibility to come back in the groundstate thus $\vec{r}(t')$ have to be very close (at the scale of Bohr radius) to the center of the potential.

Consequently, we have found the assumptions of three step model by a quasi-classical method, starting from the TDSE. The advantage of this method is that, as the TDSE method, it gives the correct energy of the cutoff for HHG from an atom: $\hbar\omega_{cut} = 3.17U_p + I_p$.

1.4 Rescattering.

Both for ATI and HHG we have neglected the contribution of the atomic potential. In the first case because we consider ionized electrons which immediately go away, and in the second one because we were interested at the cutoff region (free-electrons with $E_k >> I_p$). Actually, there is a third phenomenon, named rescattering, for which $\mathbb{V}(\vec{r})$ plays an important role. Here we consider returning electrons which do not recombine into a bound state but, being diffracted by the target system, stay in the continuum [20, 21].

Classically, we start again from the situation described by Eq. 1.28, and we are still interested in electrons returning at the center of $V(\vec{r})$, thus they have to fulfill Eq. 1.31. The latter equation depending on the ionization time t_i describes several different situations [22]

- $0 < \omega_L t_i < \frac{\pi}{2}$ the electron never comes back ,
- $\frac{\pi}{2} < \omega_L t_i < 0.5697\pi$ the electron comes back at least 3 times,
- $0.5697\pi < \omega_L t_i < \pi$ the electron returns once.

Thus, if $\omega_L t_i > \frac{\pi}{2}$, the electron can be elastically scattered at time t_r by an angle θ_r with respect its direction of motion, and the components of the velocity for a rescattered electron are

$$p_x(t) = mv_x(t) = -\frac{q_e\mathcal{E}_0}{\omega_L}\{\cos(\omega_L t) - \cos(\omega_L t_r) + \\ + \cos\theta_r[\cos(\omega_L t_r) - \cos(\omega_L t_i)]\} \tag{1.43}$$

$$p_y(t) = mv_y(t) = -\frac{q_e\mathcal{E}_0}{\omega_L}\sin\theta_r[\cos(\omega_L t_r) - \cos(\omega_L t_i)]. \tag{1.44}$$

At this point, in analogy with ATI and HHG we evaluate the maximum kinetic energy, averaged in a period,

$$\langle E_k\rangle_{T_L} = \frac{1}{2}m_e\left[\langle v_x^2\rangle_{T_L} + \langle v_y^2\rangle_{T_L}\right]; \tag{1.45}$$

by using the definitions of Eq.s (1.43,1.44)

$$\frac{1}{2}m_e\langle v_x^2\rangle_{T_L} = 2U_p\Bigg\{\frac{1}{2} + \cos^2(\omega_L t_r) + \cos^2\theta_r\left[\cos(\omega_L t_r) - \cos(\omega_L t_i)\right]^2 + \\ -2\cos\theta_r\cos(\omega_L t_r)\left[\cos(\omega_L t_r) - \cos(\omega_L t_i)\right]\Bigg\}, \quad (1.46)$$

$$\frac{1}{2}m_e\langle v_y^2\rangle_{T_L} = 2U_p\sin^2\theta_r\left[\cos(\omega_L t_r) - \cos(\omega_L t_i)\right]^2 \quad (1.47)$$

and by inserting, the last two equations in Eq. 1.45, we find

$$\langle E_k\rangle_{T_L} = 2U_p\Bigg\{\frac{1}{2} + \cos^2(\omega_L t_r) + \left[\cos(\omega_L t_r) - \cos(\omega_L t_i)\right]^2 + \\ -2\cos\theta_r\cos(\omega_L t_r)\left[\cos(\omega_L t_r) - \cos(\omega_L t_i)\right]\Bigg\} = \\ = 2U_p\Bigg\{\frac{1}{2} + 2\cos^2(\omega_L t_r) + \cos^2(\omega_L t_i) - 2\cos(\omega_L t_r)\cos(\omega_L t_i) + \\ -2\cos\theta_r\cos(\omega_L t_r)\left[\cos(\omega_L t_r) - \cos(\omega_L t_i)\right]\Bigg\}. \quad (1.48)$$

Finally, with some easy steps, the averaged kinetic energy for classic rescattered electrons is

$$\langle E_k\rangle_{T_L} = 2U_p\left\{\cos^2(\omega_L t_i) + \right. \\ \left. +2[1-\cos\theta_r]\cos(\omega_L t_r)[\cos(\omega_L t_r) - \cos(\omega_L t_i)]\right\}. \quad (1.49)$$

In these theories, we did not consider the shape $f(t)$ of the laser field, in other words we supposed to have infinitely long pulses, but this is not possible in the experiments; to deal with that, a quantity of the value of U_p has been subtracted in Eq. 1.49. Under this condition the detected electron has a velocity vector which forms an angle θ

$$\cot\theta = \frac{\langle p_x(t)\rangle_{T_L}}{\langle p_y(t)\rangle_{T_L}} = \cot(\theta_r) - \frac{\cos\omega_L t_r}{\sin\theta_r[\cos(\omega_L t_r) - \cos(\omega_L t_i)]}. \quad (1.50)$$

with the polarization direction of the incident laser. The maximum of E_k given by Eq. 1.49 is $10U_p$ and it corresponds to $\cos\theta_r = -1$ that from Eq. 1.50 implies $\theta = \pi$, thus the most energetic part of photoelectrons spectrum it is represented by back-scattered electrons.

At this point, we are able to complete our model of SFA adding the contribution of rescattering electrons (SFA2). For this purpose, we start again from Eq. 1.35 and we consider the assumptions of Sec. 1.3 thus the state of the system $|\psi(t)\rangle$ can be written as in Eq. 1.7 (but considering only the contribution of groundstate for the bounded part). In this case like in Sec. 1.2 we are interested in the probability amplitude to find an electron with momentum $\vec{p}$. The exact solution for our model is [23]

$$c_{\vec{p}} = \frac{-i}{\hbar} \lim_{t\to\infty} \int_{-t}^{t} \mathrm{d}t' \left\langle \psi_{\vec{p}}(t) \right| \mathbb{U}(t,t')\mathbb{H}(t') \left| \psi_0(t') \right\rangle \tag{1.51}$$

where, we have used

$$\begin{aligned} \left| \psi_0(t) \right\rangle &= c_0(t) \left| \phi_0 \right\rangle && (1.52) \\ \left| \psi_{\vec{p}}(t) \right\rangle &= c_{\vec{p}}(t) \left| \phi_{\vec{p}} \right\rangle && (1.53) \end{aligned}$$

and $\mathbb{U}(t,t')$ is the time-evolution operator, which has to satisfy the Dyson equation

$$\mathbb{U}(t,t') = \mathbb{U}_V(t,t') - i\int_{t}^{t'} \mathrm{d}t''\mathbb{U}_V(t,t'')\mathbb{V}(\vec{r})\mathbb{U}(t'',t'); \tag{1.54}$$

$\mathbb{U}_V(t,t')$ is the time-evolution operator linked to the Hamiltonian of a free electron in a laser field

$$\mathbb{H}_V(t) = -\frac{\hbar^2}{2m_e^2}\nabla^2 - q_e\vec{r}\cdot\vec{\mathcal{E}}(t). \tag{1.55}$$

The solutions of the TDSE associated with $\mathbb{H}_V(t)$ are the Volkov states $\left|\psi_V^{\vec{k}}(t)\right\rangle$, and consequently

$$\mathbb{U}_V(t,t') = \int \mathrm{d}^3\vec{k} \left|\psi_V^{\vec{k}}(t)\right\rangle \left\langle\psi_V^{\vec{k}}(t')\right|. \tag{1.56}$$

By inserting Eq. 1.54 in Eq. 1.51, substituting $\mathbb{U}(t'',t')$ with $\mathbb{U}_V(t'',t')$ and $\left\langle \psi_{\vec{p}}(t) \right|$ with $\left\langle\psi_V^{\vec{p}}(t)\right|$, $c_{\vec{p}}$ becomes

$$\begin{aligned} c_{\vec{p}}(t) = -\frac{i}{\hbar}\Bigg[&\int_{-\infty}^{\infty} \mathrm{d}\tau \left\langle\psi_V^{\vec{p}}(t)\right| H_I(t) \left|\psi_D(t)\right\rangle + \\ &+ \int_{-\infty}^{\infty} \mathrm{d}t \int_{-\infty}^{t} \mathrm{d}t' \int \mathrm{d}^3\vec{k} \left\langle\psi_V^{\vec{p}}(t)\right| \mathbb{V}(\vec{r}) \left|\psi_V^{\vec{k}}(t)\right\rangle \left\langle\psi_V^{\vec{k}}(t')\right| H_I(t') \left|\psi_D(t')\right\rangle\Bigg]. \end{aligned} \tag{1.57}$$

Finally, we have all the contributions that we need to explain strong field ionization phenomena. At this point, the meaning of Eq. 1.57 is very clear, the first term represents electrons directly ionized by the field in the ATI process, the second one represents rescattered electrons.

1.5 MPI in molecules and clusters

In Sec.s (1.2,1.3,1.4) we did not take into account the geometry of the target system. Apart from ATI, where $\mathbb{V}(\vec{r})$ does not play a role for isotropic systems, the MPI processes depend on the symmetry and the structure.

1.5.1 HHG.

HHG presents very interesting properties when the target system is not an atom. The immediate consequence of having a molecule without spherical symmetry, is that the spectrum presents even and odd harmonics. Other important changes appear in the polarization of the emission, that as we are going to see later, is strongly affected by the symmetry. However, it is not necessary to have very complicated structures, indeed several interesting properties of molecular geometry has been found in H_2^+ such as: a cutoff energy greater than the one from atomic targets; ions satellite lines, that depends upon the nuclear oscillation frequency ω_M etc [24, 25, 26, 2, 4, 9].

In this section, we present a very simple theory explaining why molecules present $\hbar\omega_{cut} > 3.17U_p + I_p$. We start again from Eq.s (1.28,1.29,1.30), but we consider that an electron which has been extracted from the parent ion at $x = 0$, could recombine with another ion at $x = R$, where R is the inter-atomic distance.

From a classical point of view, the maximum emission happens at the maximum of the acceleration. Thus from

$$\max a_x(t) = \frac{q_e\mathcal{E}_0}{m_e}, \tag{1.58}$$

we get $\omega_L t_r = \frac{3\pi}{2}$ and consequently

$$\max E_k(t_r) = \max\left[2U_p\cos^2\left(\omega_L t_i\right)\right] = 2U_p \leftrightarrow \omega_L t_i = \pi. \tag{1.59}$$

The recollision position for $t_i = \frac{\pi}{\omega_L}$ and $t_r = \frac{3\pi}{2\omega_L}$ is

$$x(t_r) = \frac{q_e\mathcal{E}_0}{m_e\omega_L^2}\left[\frac{\pi}{2} - 1\right] = 0.57\frac{q_e\mathcal{E}_0}{m_e\omega_L^2}, \tag{1.60}$$

this means that this emission occurs for $R = 0.57\frac{q_e\mathcal{E}_0}{m_e\omega_L^2}$.

When we consider the recombination with the same parent ion, as we know from Sec. 1.3, we have to consider $x(t_r) \to 0$ and we get $\max(E_k) = 3.17U_p$. Obviously, in order to have the maximum value of $v_x(t_r)$, we have to set $a_x(t_r) = 0$ and consequently $\omega_L t_r = 2\pi$ (note, with $\omega_L t_r = \pi$ there are not solutions of $x(t_r) = 0$ if $v_x(t_r) \neq 0$). Numerically we find from Eq. 1.29 that all these conditions are satisfied for $\omega_L t_i = 0.5835\pi$.

The generalization of this case for $a_x(t_r) = 0$ and $x(t_r) \neq 0$ gives

$$\max E_k(t_r) = \max\left\{2U_p[1 - \cos\left(\omega_L t_i\right)]^2\right\} = 8U_p \leftrightarrow \omega_L t_i = \pi, \tag{1.61}$$

and finally the position of recombination is

$$R = x(t_r) = \pi\frac{q_e\mathcal{E}_0}{m_e\omega_L^2}. \tag{1.62}$$

Thus, if an electron is ionized from a parent ion at $x = 0$ and it recombines in another ion at $R = \pi\dfrac{q_e\mathcal{E}_0}{m_e\omega_L^2}$ the cutoff energy is $\hbar\omega_{cut} = 8U_p + I_p$.

1.5.2 Quantitative rescattering theory

The photoelectron emission in the rescattering region, also, depends on the symmetry of the driven system. This is not explained by the classical theory in Sec. 1.4, thus we need to modify our model in order to consider a molecular target system. The easiest way is the quantitative rescattering theory QRT that start from Eq. (1.50) but in this case it is better to work in 3D and to consider that the returning active electrons have maximum kinetic energy $E_k = 3.17U_p$ with $x(t_r) = 0$; thus from the discussion in Sec. 1.5.1, we can rewrite Eq. (1.50) as

$$\frac{p\cos(\theta)}{p\sin(\theta)} = \frac{1}{p_r\sin(\theta_r)}\left[p_r\cos(\theta_r) - \frac{\cos\omega_L t_r}{[p_r\cos(\omega_L t_r) - \cos(\omega_L t_i)]}\right] = \\ = \frac{1}{p_r\sin(\theta_r)}\left[p_r\cos(\theta_r) - \frac{p_r}{1.26}\right] \quad (1.63)$$

where $p = \sqrt{\langle p_x(t)^2\rangle_{T_L} + \langle p_y(t)^2\rangle_{T_L} + \langle p_z(t)^2\rangle_{T_L}}$ is the amplitude of measured momentum, and $p_r = \sqrt{p_x(t_r)^2 + p_y(t_r)^2 + p_z(t_r)^2}$ is the one of the momentum right after the rescattered time t_r. If we consider a linear polarized laser along $\hat{z}$, we can write, for the three components of the momentum $\vec{p}$, the following system of equations

$$p_{r,y} = p_y \quad (1.64)$$

$$p_{r,x} = p_x \quad (1.65)$$

$$p_{r,z} = p_r/1.26 \mp p_z \quad (1.66)$$

where we have used $p_x^2 + p_y^2 = p^2\sin^2(\theta) = p_r^2\sin^2(\theta_r) = p_{r,x}^2 + p_{r,y}^2$

Thus p_r can be written as

$$p_r = \sqrt{p_{r,x}^2 + p_{r,y}^2 + p_{r,z}^2} = \sqrt{p_x^2 + p_y^2 + \left(p_z^2 + \frac{p_r^2}{1.26^2} \mp \frac{2}{1.26}p_r p_z\right)} = \\ = \sqrt{p^2 + \frac{p_r^2}{1.26^2} \mp \frac{2}{1.26}p_r p_z} \quad (1.67)$$

with some steps:

$$\left(1 - \frac{1}{1.26^2}\right)p_r^2 \pm \frac{2}{1.26}p_z p_r - p^2 = 0. \quad (1.68)$$

The Δ of this second order equation is always positive:

$$\Delta = \frac{4}{1.26^2}\left(p_z^2 + \alpha p^2\right). \quad (1.69)$$

$$\alpha = 0.26 \cdot 2.26 \quad (1.70)$$

and in addition p_r is a modulus thus we must choose the positive solution for Eq. 1.68. Thus, finally we find

$$p_r = \frac{2}{1.26}\left[\mp p_z + \sqrt{p_z^2 + \alpha p^2}\right]\frac{1.26^2}{0.26 \cdot 2.26 \cdot 2} = \\ = \frac{1.26}{\alpha}\left[\mp p_z + \sqrt{\alpha p_x^2 + \alpha p_y^2 + (1+\alpha)p_z^2}\right], \quad (1.71)$$

and Eq.s (1.66,1.71)

$$p_{r,z} = \left[\frac{1}{\alpha}\left(\mp p_z + \sqrt{\alpha p_x^2 + \alpha p_y^2 + (1+\alpha)p_z^2}\right) \mp p_z\right] = \\ = \frac{1}{\alpha}\left[\mp p_z(\alpha+1) + \sqrt{\alpha p_x^2 + \alpha p_y^2 + (1+\alpha)p_z^2}\right]. \quad (1.72)$$

At this point, we are able to define the elastic differential cross section for a molecule $\sigma(\vec{q})$. If the ions can be considered independent, we can write for a molecule fixed in space [7]

$$\sigma(\vec{q}) = \left|\sum_i c_{i,\vec{q}} e^{i\vec{q}\cdot\vec{R}_i}\right|^2 \quad (1.73)$$

where $\vec{R}_i$ is the vector position of the i-th ions, $f_i(q)$ is the complex scattering amplitude of the i-th ions and $\vec{q}$ is the transferred momentum

$$\vec{q} = \vec{p}(t_r + \mathrm{d}t_r) - \vec{p}(t_r - \mathrm{d}t_r). \quad (1.74)$$

From simple consideration $q = 2p_r \sin\left(\frac{\theta_r}{2}\right)$ and by observing that the variation of momentum is only along $\hat{z}$

$$q^2 = 2p_r^2(1-\cos\theta_r) = 2p_r^2 - 2p_r p_{r,z} = q_z^2 + q_y^2 + q_x^2 = \\ = q_z^2 + p_{r,y}^2 + p_{r,x}^2 = 2p_{r,z}^2 + 2p_{r,x}^2 + 2p_{r,y}^2 - 2p_r p_{r,z}. \quad (1.75)$$

We get

$$q_z^2 = (p_z - p_{r,z})^2 \quad (1.76)$$

and consequently

$$q_x = p_{r,x} \quad (1.77)$$

$$q_y = p_{r,y} \quad (1.78)$$

$$q_z = -p_r + p_{r,z}. \quad (1.79)$$

In the following we use the relation:

$$c_{i,\vec{q}} = \sum_{j=1}^{4} a_i e^{-b_j(\frac{q}{4\pi})^2} + c \quad (1.80)$$

where a_j, b_j, c are tabulated values depending on the ions [27]. This theory does not consider the full interaction between electrons and laser. Actually, in order to get the angular resolved photoelectron spectrum $D_{\vec{p}}$ (ARPES), we need to consider also the momentum distribution of the returning electrons.

Thus, we define the so named returning wave packet $W_{\vec{q}}$ [6]

$$D_{\mathrm{target},\vec{p}} = W_{\mathrm{target},\vec{q}}\sigma_{\mathrm{target},\vec{q}}. \quad (1.81)$$

QRT without $W_{\vec{q}}$ is quasi-independent of the laser field, actually we have only to pay attention to the range of applicability that is from $2U_p$ and $10U_p$. In order to consider the fact that the properties of the wavepacket of the returning electrons depend on the driving laser, we have to include $W_{\vec{q}}$. In addition, for a given laser, $W_{\vec{q}}$ is nearly independent of the scattering center [6] thus we can substitute the $W_{\vec{q}}$ of our system with the one obtained by a sample system like an atom driven by the same laser. By inverting Eq. 1.81 for the sample [6]

$$W_{\text{sample}}(\vec{q}) = \frac{D_{\text{sample},\vec{p}}}{\sigma_{\text{sample},\vec{q}}} \tag{1.82}$$

and, considering $W_{\text{target},\vec{q}} \cong W_{\text{sample},\vec{q}}$, we can rewrite Eq. 1.81:

$$D_{\text{target},\vec{p}} = W_{\text{sample},\vec{q}}\sigma_{\text{target},\vec{q}}. \tag{1.83}$$

Thus, this simple model allows to consider several important effects for the angular distribution of the rescattered electrons, as matter of fact this theory cannot be used for explaining direct ionization $E_k < 2U_p$. In the following we will show some comparison between experiment and computational results obtained by using this version of QRT.

1.5.3 Alignment and rotations.

The last results strongly depend on the geometry of the molecular system. In general, in the experiment, low pressure gas of atoms or molecules is used as target. As the targets are randomly distributed, the PAD should be averaged in every possible configuration. Nevertheless, there is a new important topic in experimental physics, which consists in the analysis of aligned target systems [28, 3, 29]. This kind of studies allow for example to neglect the ionization from the highest occupied molecular orbital HOMO, constraining the molecule to ionize from HOMO-1. One easy technique which allows to align molecules it is to induce dipole moments [30]. As model of molecule we consider a linear rotor subject to a weak linear polarized electric field $\vec{\mathcal{E}} = \mathcal{E}_0\hat{n}$. The TISE can be written as

$$\left[B\vec{\mathbb{J}}^2 + \mathbb{V}_\alpha(\theta)\right]\psi(\theta,\phi) = E\psi(\theta,\phi) \tag{1.84}$$

where B is the rotational constant, $\vec{\mathbb{J}}$ is the total angular momentum operator, E is the eigenenergy, θ is the angle between the molecular axis $\hat{z}$ and the polarization axis $\hat{n}$, and

$$\mathbb{V}_\alpha = -\frac{1}{4}\mathcal{E}_0^2(\alpha_\parallel \cos^2\theta + \alpha_\perp \sin^2\theta) \tag{1.85}$$

is the averaged interaction potential, note the dipole potential $-q_e\vec{r}\cdot\vec{\mathcal{E}}$ averaged in a period is zero, thus it does not appear in Eq. 1.84. In order to solve Eq. 1.84 we use the method of separation of variables $\psi(\theta,\phi)$:

$$\psi(\theta,\phi) = S_{j,m}(\theta)\Phi_m(\phi), \tag{1.86}$$

where j is the total angular momentum quantum number and m the magnetic number. Thus Eq. 1.84 can be written as

$$\left[-\vec{\mathbb{J}}^2 - \frac{1}{B}\mathbb{V}_\alpha(\theta) + \frac{E_{j,m}}{B}\right]S_{j,m}(\theta)\Phi_m(\phi) = 0 \tag{1.87}$$

and using

$$\vec{\mathbb{J}}^2 = -\hbar^2 \left[\frac{1}{\sin\theta} \frac{\partial}{\partial\theta} \left(\sin\theta \frac{\partial}{\partial\theta} \right) + \frac{1}{\sin^2\theta} \frac{\partial^2}{\partial\phi^2} \right] \tag{1.88}$$

it assumes the form of

$$\begin{aligned} \frac{\hbar^2 \sin^2\theta}{S_{j,m}(\theta)} \left[\frac{1}{\sin\theta} \frac{\partial}{\partial\theta} \left(\sin\theta \frac{\partial}{\partial\theta} \right) - \frac{1}{\hbar^2 B} \mathbb{V}_\alpha(\theta) + \frac{E_{j,m}}{\hbar^2 B} \right] S_{j,m}(\theta) = \\ = -\frac{\hbar^2}{\Phi_m(\phi)} \frac{\partial^2}{\partial\phi^2} \Phi_m(\phi). \end{aligned} \tag{1.89}$$

At this point, we split Eq. (1.89) in

$$\frac{\partial^2}{\partial\phi^2} \Phi_m(\phi) = -m^2 \Phi_m(\phi) \tag{1.90}$$

and

$$\hbar^2 \sin^2\theta \left[\frac{1}{\sin\theta} \frac{\partial}{\partial\theta} \left(\sin\theta \frac{\partial}{\partial\theta} \right) - \frac{1}{B} \mathbb{V}_\alpha(\theta) + \frac{E_{j,m}}{B} \right] S_{j,m}(\theta) = \hbar^2 m^2 S_{j,m}(\theta). \tag{1.91}$$

With some substitutions

$$z = \cos\theta \tag{1.92}$$

$$\frac{\partial}{\partial\theta} = \frac{\partial z}{\partial\theta} \frac{\partial}{\partial z} \tag{1.93}$$

$$\beta^2 = \frac{\mathcal{E}_0^2}{4B} (\alpha_\parallel - \alpha_\perp) \tag{1.94}$$

$$\lambda_{j,m} = \frac{\mathcal{E}_0^2}{4B} \alpha_\perp + E_{j,m}/B \tag{1.95}$$

$$\sin^2\theta = 1 - z^2 \tag{1.96}$$

$$\tag{1.97}$$

we finally get

$$\left\{ \hbar^2 \frac{\mathrm{d}}{\mathrm{d}z} \left[(1-z^2) \frac{\mathrm{d}}{\mathrm{d}z} \right] - \frac{\hbar^2 m^2}{1-z^2} + \lambda_{j,m} + \beta^2 z^2 \right\} S_{j,m}(\theta) = 0 \tag{1.98}$$

this is an oblate spheroidal equation. If $\beta^2 = 0$, Eq. 1.98 becomes

$$\left\{ \hbar^2 \frac{\mathrm{d}}{\mathrm{d}z} \left[(1-z^2) \frac{\mathrm{d}}{\mathrm{d}z} \right] - \frac{\hbar^2 m^2}{1-z^2} + \hbar^2 j(j+1) \right\} S_{j,m}(z) = 0 \tag{1.99}$$

where $S_{j,m}(z)$ in this case is the Legendre Polynomial $P_{j,m}(z)$. In this case, $\psi_{j,m}(\theta,\phi) = Y_{j,m}(\theta,\phi)$, the other solutions can be found tabulated in [31]. In order to evaluate the alignment we have to calculate the expectation value of the squared alignment cosine, which is a summation over every $\bar{j} = |m|$ of $\langle \cos^2\theta \rangle_{\bar{j},m}$ weighted by

$$w_j = \frac{e^{-\frac{\bar{j}(\bar{j}+1)}{k_b T/B}}}{Q_r}, \tag{1.100}$$

where Q_r is the rotational partition function. For $\beta^2 \to 0$ the alignment angular distribution takes the form of

$$n(\theta) = 1 + \frac{5}{2}(3\langle\cos^2\theta\rangle - 1)P_2(\cos\theta) + \dots \tag{1.101}$$

otherwise for $\beta^2 \to \infty$

$$n(\theta) = e^{-\frac{1}{2}\frac{\sin^2\theta}{\sigma^2}} \tag{1.102}$$

$$\sigma^2(\theta) = 1 - \langle\cos^2\theta\rangle. \tag{1.103}$$

In conclusion, we are able to calculate the ensemble alignment as functions of rotational temperature k_bT/B, polarizability ($\alpha_\parallel$, $\alpha_\perp$), rotational constant B and the laser intensity $\mathcal{E}_0$. Thus in order to compare experiment and theory on aligned molecule, the theoretical data should be angular averaged following $n(\theta)$, in order to correctly reproduce the experiment.

1.6 Many body phenomena.

In a large part of this introductive analysis, we did not consider the many electrons effects. Actually, for a several numbers of intent it is a good approximation for strong laser physics. However, there are some effects that could be explained only considering contributions for more than one orbitals especially for aligned molecules or high symmetric systems. For example, it has been found experimentally that for molecule with p-HOMO, if the probe laser and the molecular axis are aligned the biggest contribution to the total ionization comes from the s-(HOMO-1). In addition, if we look more in detail the photoelectron spectrum by studying the PAD, we find holographic features about the orbitals. Another approximation that we did, was to consider one electron in a mean field generated by the presence of the others electrons and the nuclei. As matter of fact, we should consider the quantum mechanic nature of every particles in the system.

A molecule or an atom are complicated collections of electrons and nuclei. Of course, the force which plays a role is the Coulomb interaction. We are interested in to derive in a easy way the many-body TISE, thus we have to write the energy associated with the Coulomb interaction, which is from a classical point of view [32]

$$V_{ee} = \frac{1}{2}\sum_{i\neq j}^{n_e}\frac{q_e^2}{|\vec{r}_i - \vec{r}_j|} \tag{1.104}$$

$$V_{NN} = \frac{1}{2}\sum_{i\neq j}^{n_n}\frac{Z^2q_e^2}{|\vec{R}_i - \vec{R}_j|} \tag{1.105}$$

$$V_{Ne} = -\sum_{i}^{n_n}\sum_{j}^{n_e}\frac{Zq_e^2}{|\vec{R}_i - \vec{r}_j|}, \tag{1.106}$$

where Zq_e is the nuclear charge, n_n is the number nuclei in the system and n_e of electrons, $\vec{r}_j$ and $\vec{R}_i$ with $i = 1\dots n_n$ and $j = 1\dots n_e$ are respectively the position of the nucleus i and the electron j. The many body Hamiltonian must assume the same form of Eq. 1.4, but, in this case we have to substitute the kinetic energy operator $\mathbb{T} = \frac{\mathbb{p}^2}{2m_e}$ with the summations of the kinetic energies of all electrons and nuclei

$$\mathbb{T} = \mathbb{T}_e + \mathbb{T}_n \tag{1.107}$$

$$\mathbb{T}_e = -\sum_i^{n_e} \frac{\hbar^2}{2m_e} \nabla_{i,r}^2 \tag{1.108}$$

$$\mathbb{T}_n = -\sum_i^{n_n} \frac{\hbar^2}{2m_{n,i}} \nabla_{i,R}^2, \tag{1.109}$$

where $m_{n,i}$ is the mass of the i nucleus. The binding energy operator $\mathbb{V}$ generally is the quantum mechanics counterpart of the summations of V_{ee}, V_{NN} and V_{Ne} thus the many body TISE is [33, 34, 35, 36, 37]

$$\left[-\sum_i^{n_e} \frac{\hbar^2}{2m_e} \nabla_{i,r}^2 - \sum_i^{n_n} \frac{\hbar^2}{2m_{n,i}} \nabla_{i,R}^2 + \frac{1}{2} \sum_{i \neq j}^{n_e} \frac{q_e^2}{|\vec{r}_i - \vec{r}_j|} + \right.$$
$$\left. + \frac{1}{2} \sum_{i \neq j}^{n_n} \frac{Z^2 q_e^2}{|\vec{R}_i - \vec{R}_j|} - \sum_i^{n_n} \sum_j^{n_e} \frac{Z q_e^2}{|\vec{R}_i - \vec{r}_j|} \right] |\psi\rangle = E \, |\psi\rangle \, . \tag{1.110}$$

From Eq. 1.110, we can find the solution under SAE approximation by considering that the active electron feels the interaction with the other particles as mean field effect. In addition, if we consider that the electronic mass is negligible compared to the nuclear mass, the kinetic energy of the nuclei is also negligible and consequently the nuclei can be assume fixed in the space ($\mathbb{V}_{NN}$ constant). The TISE under fixed nuclei approximation becomes

$$\left[-\sum_i^{n_e} \frac{\hbar^2}{2m_e} \nabla_{i,r}^2 + \frac{1}{2} \sum_{i \neq j}^{n_e} \frac{q_e^2}{|\vec{r}_i - \vec{r}_j|} - \sum_i^{n_n} \sum_j^{n_e} \frac{Z q_e^2}{|\vec{R}_i - \vec{r}_j|} \right] |\psi\rangle = E' \, |\psi\rangle \, , \tag{1.111}$$

$$E' = E - \frac{1}{2} \sum_{i \neq j}^{n_n} \frac{Z^2 q_e^2}{|\vec{R}_i - \vec{R}_j|}. \tag{1.112}$$

1.7 Summary

In this introductive chapter we gave a look of the world of strong field physics, with a didactic aim. In the following, we are going to present more rigorous theory and interesting new results found in the PhD study period.

2

Theory

In the previous chapter, we underlined some features of the strong field ionization (SFI). In this chapter we develop the theories used for the results in this thesis.

We solve the TISE and TDSE Eq.s (1.1,1.5), both from a many body point of view, using the density functional theory (DFT), and under SAE approximation. Thus, depending on the system and on the features that we want to observe we use different approaches.

2.1 Quantum rings.

2.1.1 Plain rings.

In the first part of this chapter, we analyze an artificial nanostructure system named quantum ring [38, 39, 40, 41, 42, 43, 44, 45]. This system is composed by a charge bound to a toroidal structure of radius R of some nanometers (see Fig. (2.1)). The simplest way, to model this system, is to consider an electron constrained to stay in a circle. This very simple 1D system, named plain ring, allows the identification of various interesting results [8, 46, 47]. In this case, the TISE can be written as

$$\frac{\mathbb{L}^2}{2m_e R^2} |\phi\rangle = E |\phi\rangle \tag{2.1}$$

which admits solutions

$$|\phi_{\pm\ell}\rangle = \frac{1}{\sqrt{2\pi}} e^{\pm i\ell\varphi} \tag{2.2}$$

$$E_\ell = \frac{\hbar^2 \ell^2}{2m_e R^2} \tag{2.3}$$

$$\ell = 0, 1, \dots, \infty \tag{2.4}$$

where $\mathbb{L}$ is the angular momentum operator, ℓ is the angular momentum quantum number, φ is the angular variable. It is interesting to note that every energy E_ℓ with $\ell > 0$ is degenerate, this behaviour is caused by the fact that the system has circular symmetry.

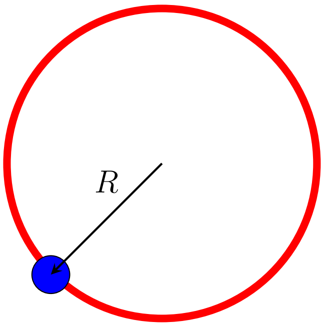

Figure 2.1: Picture of a 1D plain ring.

2.1.2 Structured quantum rings.

Another important quantum nanostructure is represented by the structured quantum ring SQR. The SQR is formed by an electron bounded again to a circle, with M dots along. The physics properties of this system strickly depend on the number of dots and the relative positions of the dots in the circle. If we consider a 1D system with M dots not necessarily equal along a circle of radius R we could write the binding energy as

$$\mathbb{V}_S(\varphi) = \sum_{n=1}^{M} -\frac{K_n}{\sqrt{\eta_n + 1 - \cos(\varphi - \varphi_n)}} \tag{2.5}$$

that mimics the presence of M dots at the angular positions φ_n, where η_n are soft-core constants (in order to smooth the potential for $(\varphi = \varphi_n)$) and K_n normalization constants [48].

In any case, the SQR was originally presented with M identical and equidistant dots along the ring, thus the binding energy can assume the form of (see Fig. (2.2))

$$\mathbb{V}_C(\varphi) = V_0 \cos(M\varphi). \tag{2.6}$$

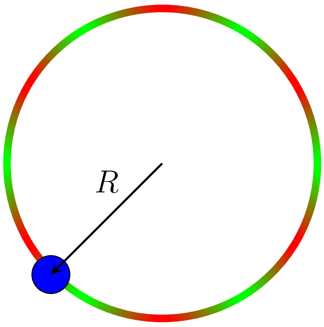

Figure 2.2: Picture of a 1D SQR, with $M = 6$ red dots.

The TISE becomes

$$-\frac{\hbar^2}{2m_e R^2}\frac{\partial^2}{\partial\varphi^2}\left|\phi\right\rangle+\mathbb{V}_C(\varphi)\left|\phi\right\rangle=E\left|\phi\right\rangle, \tag{2.7}$$

this is not an easy equation, but can be rewritten as the well known Mathieu equation. With some easy substitutions [49]:

$$\begin{cases} N=\dfrac{M}{2} \\ x=N\varphi \\ a=\dfrac{2m_e R^2 E}{\hbar^2 N^2} \\ q=\dfrac{m_e R^2 V_0}{\hbar^2 N^2}, \end{cases} \tag{2.8}$$

we get

$$\begin{cases} \dfrac{\mathrm{d}^2}{\mathrm{d}x^2}\Phi(x)+[a-2q\cos(2x)]\Phi(x)=0 \\ x\in[0,2N\pi] \\ \Phi(0)=\Phi(2N\pi) \\ \left|\phi\right\rangle\rightarrow\Phi(\varphi), \end{cases} \tag{2.9}$$

note for $M=1,2$ we get the standard Mathieu equations and consequently solutions.

The Mathieu's equation, originally introduced to describe the normal modes of an elliptical drumhead, is among the hardest equation of mathematical physics. For $M=1,2$, the boundary conditions are respectively $\Phi(0)=\Phi(\pi)$ and $\Phi(0)=\Phi(2\pi)$; the so named Mathieu's functions are the solutions. These are described in many books, papers and tables [50, 31, 51, 52, 53, 54, 55].

In order to solve the Mathieu equation (2.9) with general boundary conditions, we split the general solution as the sum of an even $\Phi_{a,j}(q;x)$ and an odd $\Phi_{b,j}(q;x)$ part:

$$\Phi_j(q;x)=\Phi_{a,j}(q;x)+\Phi_{b,j}(q;x) \tag{2.10}$$

with $j=0,1,2,\ldots$. As first step, we determine the degeneration rules of the eigenvalues $a_j^{(N)}(q)$ (even) and $b_j^{(N)}(q)$ (odd) (which corresponds to the solutions $\Phi_{a,j}(q;x)$ and $\Phi_{b,j}(q;x)$) of the Mathieu's equation [56, 57, 31, 58, 54, 59, 60]:

$$\begin{cases} \dfrac{\mathrm{d}^2}{\mathrm{d}x^2}\Phi_{a,j}(q;x)+\left[a_j^{(N)}(q)-2q\cos 2x\right]\Phi_{a,j}(q;x)=0 \\ \Phi_{a,j}(q;0)=\Phi_{a,j}(q;2N\pi) \end{cases} \tag{2.11}$$

$$\begin{cases} \dfrac{\mathrm{d}^2}{\mathrm{d}x^2}\Phi_{b,j}(q;x)+\left[b_j^{(N)}(q)-2q\cos 2x\right]\Phi_{b,j}(q;x)=0 \\ \Phi_{b,j}(q;0)=\Phi_{b,j}(q;2N\pi) \end{cases} \tag{2.12}$$

$$x\in[0,2N\pi] \tag{2.13}$$

.

At this point, we can study separately the equations for even and odd M. The case of a plain ring ($q=0$) can be easily solved (note: for the boundary conditions this is a plain ring with not integer magnetic number):

$\Phi_{a,j}(0;x) = \cos\left(\frac{jx}{N}\right)$, $\Phi_{b,j}(0;x) = \sin\left(\frac{jx}{N}\right)$, $a_j^{(N)}(0) = b_j^{(N)}(0) = \dfrac{j^2}{N^2}$.

In order to solve the not trivial SQR problem ($q \neq 0$), we expand eigenfunction and eigenvalue as power of q:

$$\begin{cases} \Phi_{a,j}(q;x) = \cos\left(\frac{jx}{N}\right) + \sum_{n=1}^{\infty} c_{n,j}^{(N)}(x) q^n \\ a_j^{(N)}(q) = \dfrac{j^2}{N^2} + \sum_{n=1}^{\infty} \alpha_{n,j}^{(N)} q^n \end{cases} \tag{2.14}$$

$$\begin{cases} \Phi_{b,j}(q;x) = \sin\left(\frac{jx}{N}\right) + \sum_{n=1}^{\infty} s_{n,j}^{(N)}(x) q^n \\ b_j^{(N)}(q) = \dfrac{j^2}{N^2} + \sum_{n=1}^{\infty} \beta_{n,j}^{(N)} q^n \end{cases} \tag{2.15}$$

with $c_{n,j}^{(N)}(x)$ and $s_{n,j}^{(N)}(x)$ respectively even and odd functions; it is important to remark that in any part of this theory, we set the coefficients of $\cos(jx/N)$ and $\sin(jx/N)$, at any order of approximation, equal to 1; this condition determines the renormalization of the α and β coefficients at any order. By inserting Eq.s (2.14,2.15) into Eq.s (2.11) and (2.12) we get for the even case:

$$\begin{aligned} q\left[\frac{\mathrm{d}^2 c_{1,j}^{(N)}}{\mathrm{d}x^2} + \alpha_{1,j}^{(N)} \cos\left(\frac{jx}{N}\right) + \frac{j^2}{N^2} c_{1,j}^{(N)} - 2\cos(2x)\cos\left(\frac{jx}{N}\right)\right] + \\ + \sum_{n=2}^{\infty} q^n \left[\frac{\mathrm{d}^2 c_{n,j}^{(N)}}{\mathrm{d}x^2} + \frac{j^2}{N^2} c_{n,j}^{(N)} + \alpha_{n,j}^{(N)} \cos\left(\frac{jx}{N}\right) + \right. \\ \left. + \sum_{m=1}^{n-1} (\alpha_{n-m,j}^{(N)} c_{m,j}^{(N)}) - 2\cos(2x) c_{n-1,j}^{(N)}\right] = 0 \end{aligned} \tag{2.16}$$

and for the odd one:

$$\begin{aligned} q\left[\frac{\mathrm{d}^2 s_{1,j}^{(N)}}{\mathrm{d}x^2} + \beta_{1,j}^{(N)} \sin\left(\frac{jx}{N}\right) + \frac{j^2}{N^2} s_{1,j}^{(N)} - 2\cos(2x)\sin\left(\frac{jx}{N}\right)\right] + \\ + \sum_{n=2}^{\infty} q^n \left[\frac{\mathrm{d}^2 s_{n,j}^{(N)}}{\mathrm{d}x^2} + \frac{j^2}{N^2} s_{n,j}^{(N)} + \beta_{n,j}^{(N)} \sin\left(\frac{jx}{N}\right) + \right. \\ \left. + \sum_{m=1}^{n-1} (\beta_{n-m,j}^{(N)} s_{m,j}^{(N)}) - 2\cos(2x) s_{n-1,j}^{(N)}\right] = 0. \end{aligned} \tag{2.17}$$

At this point, we can use the polynomial identity and thus we equate the coefficients in (2.16) and (2.17) at different order of q to zero, and in this way, we calculate the corrections at various order of approximations.

For the first order, we obtain:

$$\begin{cases}\dfrac{\mathrm{d}^2 c_{1,j}^{(N)}}{\mathrm{d}x^2}+\frac{j^2}{N^2}c_{1,j}^{(N)}+\alpha_{1,j}^{(N)}\cos\left(\dfrac{jx}{N}\right)-\cos\left(\frac{j+2N}{N}x\right)-\cos\left(\frac{j-2N}{N}x\right)=0,\\ c_{1,j}^{(N)}(0)=c_{1,j}^{(N)}(2N\pi),\end{cases}\tag{2.18}$$

$$\begin{cases}\dfrac{\mathrm{d}^2 s_{1,j}^{(N)}}{\mathrm{d}x^2}+\frac{j^2}{N^2}s_{1,j}^{(N)}+\beta_{1,j}^{(N)}\sin\left(\frac{jx}{N}\right)-\sin\left(\frac{j+2N}{N}x\right)-\sin\left(\frac{j-2N}{N}x\right)=0,\\ s_{1,j}^{(N)}(0)=s_{1,j}^{(N)}(2N\pi).\end{cases}\tag{2.19}$$

The homogeneous equations associated admit the same kind of solution in the form of $A\cos(jx/N)+B\sin(jx/N)$ but for our choice of normalization (coefficients of $\cos(jx/N)$ and $\sin(jx/N)$ are equal to 1 at any order of approximation), thus we can neglect this solution. For solving the inhomogeneous differential equations we have to distinguish two different cases: $j\neq N$ and $j=N$.

If $j\neq N$, we have to solve two system of three equations:

$$\begin{cases}\dfrac{\mathrm{d}^2 c_{1,j}^{(N)}}{\mathrm{d}x^2}+\dfrac{j^2}{N^2}c_{1,j}^{(N)}+\alpha_{1,j}^{(N)}\cos\left(\dfrac{jx}{N}\right)=0,\\ \dfrac{\mathrm{d}^2 c_{1,j}^{(N)}}{\mathrm{d}x^2}+\dfrac{j^2}{N^2}c_{1,j}^{(N)}-\cos\left(\dfrac{j+2N}{N}x\right)=0,\\ \dfrac{\mathrm{d}^2 c_{1,j}^{(N)}}{\mathrm{d}x^2}+\dfrac{j^2}{N^2}c_{1,j}^{(N)}-\cos\left(\dfrac{j-2N}{N}x\right)=0,\\ c_{1,j}^{(N)}(0)=c_{1,j}^{(N)}(2N\pi),\end{cases}\tag{2.20}$$

$$\begin{cases}\dfrac{\mathrm{d}^2 s_{1,j}^{(N)}}{\mathrm{d}x^2}+\dfrac{j^2}{N^2}s_{1,j}^{(N)}+\beta_{1,j}^{(N)}\sin\left(\dfrac{jx}{N}\right)=0,\\ \dfrac{\mathrm{d}^2 s_{1,j}^{(N)}}{\mathrm{d}x^2}+\dfrac{j^2}{N^2}s_{1,j}^{(N)}-\sin\left(\dfrac{j+2N}{N}x\right)=0,\\ \dfrac{\mathrm{d}^2 s_{1,j}^{(N)}}{\mathrm{d}x^2}+\dfrac{j^2}{N^2}s_{1,j}^{(N)}-\sin\left(\dfrac{j-2N}{N}x\right)=0,\\ s_{1,j}^{(N)}(0)=s_{1,j}^{(N)}(2N\pi),\end{cases}\tag{2.21}$$

in order to neglect the solutions of the two first differential equations that having respectively the form of $x\sin\left(\dfrac{jx}{N}\right)$ and $x\cos\left(\dfrac{jx}{N}\right)$, do not fulfill the boundary conditions, we have to impose $\alpha_{1,j}^{(N)}=\beta_{1,j}^{(N)}=0$. Therefore for $j\neq N$, the two eigenvalues with the same j are not split and

$$\begin{cases}c_{1,j}^{(N)}(x)=-\dfrac{N}{4}\left[\dfrac{\cos\left(\frac{j+2N}{N}x\right)}{N+j}+\dfrac{\cos\left(\frac{j-2N}{N}x\right)}{N-j}\right],\\ s_{1,j}^{(N)}(x)=-\dfrac{N}{4}\left[\dfrac{\sin\left(\frac{j+2N}{N}x\right)}{N+j}+\dfrac{\sin\left(\frac{j-2N}{N}x\right)}{N-j}\right],\\ \alpha_{1,j}^{(N)}=\beta_{1,j}^{(N)}=0.\end{cases}\tag{2.22}$$

For $j=N$ we have only two inhomogeneous equations and the corrections are

$$c_{1,N}^{(N)}(x)=-\frac{1}{8}\cos 3x,\quad s_{1,N}^{(N)}(x)=-\frac{1}{8}\sin 3x,\quad \alpha_{1,N}^{(N)}=-\beta_{1,N}^{(N)}=1.$$

At the first order of approximation in q the two eigenvalues with $j=N$ are non-degenerates and $\alpha_{1,N}^{(N)}-\beta_{1,N}^{(N)}$=2. These solutions ($j=N$) correspond to traditional Mathieu solutions $ce_1(q;x), se_1(q;x)$ [56, 57, 31, 58, 54, 59, 60], thus, we need to study at higher order the case $j\neq N$.

The q^2-system of equations in Eq.s 2.16 and 2.17 is

$$\begin{cases}\dfrac{\mathrm{d}^2}{\mathrm{d}x^2}c_{2,j}^{(N)}+\dfrac{j^2}{N^2}c_{2,j}^{(N)}+\alpha_{2,j}^{(N)}\cos\left(\dfrac{jx}{N}\right)-2\cos(2x)c_{1,j}^{(N)}=0,\\ c_{2,j}^{(N)}(0)=c_{2,j}^{(N)}(2N\pi),\end{cases}\tag{2.23}$$

$$\begin{cases}\dfrac{\mathrm{d}^2}{\mathrm{d}x^2}s_{2,j}^{(N)}+\dfrac{j^2}{N^2}s_{2,j}^{(N)}+\beta_{2,j}^{(N)}\sin\left(\dfrac{jx}{N}\right)-2\cos(2x)s_{1,j}^{(N)}=0,\\ s_{2,j}^{(N)}(0)=s_{2,j}^{(N)}(2N\pi).\end{cases}\tag{2.24}$$

We use the prostapheresis rules

$$2\cos(2x)\cos\left(\frac{j\pm 2N}{N}x\right)=\cos\left(\frac{j\pm 4N}{N}x\right)+\cos\left(\frac{j}{N}x\right),$$

$$2\cos(2x)\sin\left(\frac{j\pm 2N}{N}x\right)=\sin\left(\frac{j\pm 4N}{N}x\right)+\sin\left(\frac{j}{N}x\right).$$

to transform the terms $-2\cos(2x)c_{1,j}^{(N)}$ and $-2\cos(2x)s_{1,j}$, where $c_{1,j}^{(N)}$ and $s_{1,j}^{(N)}$ are given by Eq. (2.22). As above we separate two different cases: $4N-j\neq j$ (i.e. $j\neq 2N$); $j=2N$. If $j\neq 2N$, the degenerate solutions are:

$$\alpha_{2,j}^{(N)}=\beta_{2,j}^{(N)}=-\frac{1}{2}\left[\frac{1}{1-\dfrac{j^2}{N^2}}\right]=-\frac{1}{2}\left[\frac{1}{1-a_j^{(N)}(0)}\right],\tag{2.25}$$

$$c_{2,j}^{(N)}(x)=\frac{N^2}{32}\left[\frac{\cos\left(\frac{j+4N}{N}x\right)}{(N+j)(2N+j)}+\frac{\cos\left(\frac{j-4N}{N}x\right)}{(N-j)(2N-j)}\right],\tag{2.26}$$

$$s_{2,j}^{(N)}(x)=\frac{N^2}{32}\left[\frac{\sin\left(\frac{j+4N}{N}x\right)}{(N+j)(2N+j)}+\frac{\sin\left(\frac{j-4N}{N}x\right)}{(N-j)(2N-j)}\right].\tag{2.27}$$

At the contrary for $j=2N$ the corrections to the non-degenerate eigenvalues are given by

$$\alpha_{2,2N}^{(N)}=\frac{5}{12},\ \beta_{2,2N}^{(N)}=-\frac{1}{12}.$$

Once again for the third order in q, we get

$$\begin{cases} \dfrac{\mathrm{d}^2 c_{3,j}^{(N)}}{\mathrm{d}x^2} + \dfrac{j^2}{N^2} c_{3,j}^{(N)} + \alpha_{3,j}^{(N)} \cos\left(\frac{j}{N}x\right) + \\ + \left[\alpha_{2,j}^{(N)} \dfrac{N}{4} \dfrac{1}{N-j} - \dfrac{N^2}{32} \dfrac{1}{(N-j)(2N-j)}\right] \cos\left(\frac{j-2N}{N}x\right) + \\ + \left[\alpha_{2,j}^{(N)} \dfrac{N}{4} \dfrac{1}{N+j} - \dfrac{N^2}{32} \dfrac{1}{(N+j)(2N+j)}\right] \cos\left(\frac{j+2N}{N}x\right) + \\ - \dfrac{N^2}{32} \dfrac{\cos\left(\frac{j+6N}{N}x\right)}{(N+j)(2N+j)} - \dfrac{N^2}{32} \dfrac{\cos\left(\frac{j-6N}{N}x\right)}{(N-j)(2N-j)} = 0, \\ c_{3,j}^{(N)}(0) = c_{3,j}^{(N)}(2N\pi), \end{cases} \tag{2.28}$$

$$\begin{cases} \dfrac{\mathrm{d}^2 s_{3,j}^{(N)}}{\mathrm{d}x^2} + \dfrac{j^2}{N^2} s_{3,j}^{(N)} + \beta_{3,j}^{(N)} \sin\left(\frac{j}{N}x\right) + \\ + \left[\beta_{2,j}^{(N)} \dfrac{N}{4} \dfrac{1}{N-j} - \dfrac{N^2}{32} \dfrac{1}{(N-j)(2N-j)}\right] \sin\left(\frac{j-2N}{N}x\right) + \\ + \left[\beta_{2,j}^{(N)} \dfrac{N}{4} \dfrac{1}{N+j} - \dfrac{N^2}{32} \dfrac{1}{(N+j)(2N+j)}\right] \sin\left(\frac{j+2N}{N}x\right) + \\ - \dfrac{N^2}{32} \dfrac{\sin\left(\frac{j+6N}{N}x\right)}{(N+j)(2N+j)} - \dfrac{N^2}{32} \dfrac{\sin\left(\frac{j-6N}{N}x\right)}{(N-j)(2N-j)} = 0, \\ s_{3,j}^{(N)}(0) = s_{3,j}^{(N)}(2N\pi). \end{cases} \tag{2.29}$$

for $6N - j \neq j$, the degenerates eigenvalues

$$\alpha_{3,j}^{(N)} = \beta_{3,j}^{(N)} = 0, \tag{2.30}$$

and the non-degenerate corrections for $j = 3N$

$$\alpha_{3,j}^{(N)} = \frac{1}{64}, \ \beta_{3,j}^{(N)} = -\frac{1}{64}.$$

Iterating we can state that the eigenvalues $a_j^{(N)}(q)$ and $b_j^{(N)}(q)$ are non-degenerate if:

$$j = nN, \tag{2.31}$$

$$n = 0, 1, 2, \ldots. \tag{2.32}$$

The degeneration rule, Eq. (2.31) shows that the eigenvalues $a_j^{(N)}$ and $b_j^{(N)}$ are non-degenerate if j is a multiple of N and that $n = \dfrac{j}{N}$ gives the q minimum order that fulfills the condition

$$a_{nN}^{(N)}(q) - b_{nN}^{(N)}(q) \neq 0 \tag{2.33}$$

. Actually, it is important to note that if we expand until the n-th order, every eigenvalue with $j > nN$ appears not to be split. The other eigenvalues (those for which $j \neq nN$) are degenerate. Furthermore, it is possible to show that [61]

$$a_{nN}^{(N)}(q) - b_{nN}^{(N)}(q) = \frac{2q^n}{[2^{n-1}(n-1)!]^2}(1 + O(q^2))$$

and that the rate of convergence for the power series of $a_j^{(N)}(q)$ in q can be written as [61]:

$$\frac{a_{j+2\ell N}^{(N)}}{a_{j+2N(\ell\mp 1)}^{(N)}} = \frac{-q}{4\ell^2}\left(1 + O\left(\frac{1}{\ell^2}\right)\right).$$

This ratio is inversely proportional to the square of ℓ and it is independent from the considered eigenvalue and from the number of dots.

For odd M, by following a procedure analogous to the one introduced in the previous sub-section for even M, it is possible to find the expressions for the eigenstates and the corresponding eigenenergies. In this case, the non-degenerates eigenvalues are those corresponding to the index:

$$2k = 2lM. \tag{2.34}$$

where $2l$ represents the minimum order of q for which $a_{2k}(q) \neq b_{2k}(q)$.

Practical examples

$j = 1$	$j = 2$	$j = 3$
$a_1^{(3)}(q) = \frac{1}{9} - \frac{9}{16}q^2 + \dots$	$a_2^{(3)}(q) = \frac{4}{9} - \frac{9}{10}q^2 + \dots$	$a_3^{(3)}(q) = 1 + q + \dots$
$b_1^{(3)}(q) = a_1^{(3)}(q)$	$b_2^{(3)}(q) = a_2^{(3)}(q)$	$b_3^{(3)}(q) = 1 - q + \dots$
$\Phi_{a,1}(q;x) = \cos\left(\frac{x}{3}\right) +$ $+ \sum_{n=1}^{\infty} c_{n,1}^{(3)}(x)q^n$	$\Phi_{a,2}(q;x) = \cos\left(\frac{2x}{3}\right) +$ $+ \sum_{n=1}^{\infty} c_{n,2}^{(3)}(x)q^n$	$\Phi_{a,3}(q;x) = \cos x +$ $+ \sum_{n=1}^{\infty} c_{n,3}^{(3)}(x)\, q^n$
$\Phi_{b,1}(q;x) = \sin\left(\frac{x}{3}\right) +$ $+ \sum_{n=1}^{\infty} s_{n,1}^{(3)}(x)q^n$	$\Phi_{b,2}(q;x) = \sin\left(\frac{2x}{3}\right) +$ $+ \sum_{n=1}^{\infty} s_{n,2}^{(3)}(x)q^n$	$\Phi_{b,3}(q;x) = \sin x +$ $+ \sum_{n=1}^{\infty} s_{n,3}^{(3)}(x)\, q^n$

Table 2.1: Summary of solutions obtained for $M = 6$, and $j \leq 3$.

In Table 2.1 we summarize the results obtained for the particular case of $M = 6$ [62].

2.2 2D quantum rings

A better way to describe a quantum ring is to consider an electron moving in a 2D plane with a potential energy:

$$U(r) = -U_0 \left(\frac{r}{R}\right)^2 e^{[1-(r/R)^4]/2}, \tag{2.35}$$

thus a flat ring of radius R (a scheme in Fig. 2.3).

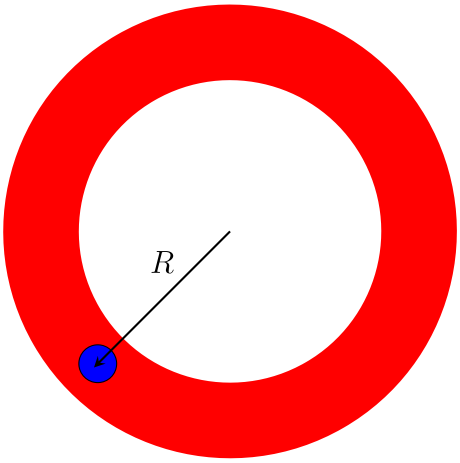

Figure 2.3: Schematic representation of the 2D plain ring (note in the next chapter we are going to plot the real potential used for simulations in this thesis).

In this case the Hamiltonian is:

$$\hat{H}_2 = -\frac{\hbar^2}{2m_e}\left(\frac{\partial^2}{\partial r^2} + \frac{1}{r}\frac{\partial}{\partial r} + \frac{1}{r^2}\frac{\partial^2}{\partial \phi^2}\right) + U(r) \tag{2.36}$$

and thus, the TISE $\hat{H}_2 u(r,\phi) = Eu(r,\phi)$ has as solutions both bound (like in the 1D case) and continuum states. We are only interesting in the bound states $E < 0$, and by setting

$$V(r) \equiv \frac{2m_e}{\hbar^2}U(r), \quad V_0 \equiv \frac{2m_e}{\hbar^2}U_0, \quad w^2 \equiv -\frac{2m_e}{\hbar^2}E. \tag{2.37}$$

and by separating the variables $u(r,\phi) \equiv \mathcal{R}(r)\Phi(\phi)$ we obtain the TISE

$$\frac{r^2}{\mathcal{R}}\frac{\mathrm{d}^2\mathcal{R}}{\mathrm{d}r^2} + \frac{r}{\mathcal{R}}\frac{\mathrm{d}\mathcal{R}}{\mathrm{d}r} - r^2V(r) - w^2r^2 = -\frac{1}{\Phi}\frac{\mathrm{d}^2\Phi}{\mathrm{d}\phi^2}. \tag{2.38}$$

If m is the separation constant, we can rewrite for the angular part

$$\frac{1}{\Phi_m}\frac{\mathrm{d}^2\Phi_m}{\mathrm{d}\phi^2} = -m^2 \Rightarrow \Phi_m(\phi) = \frac{e^{im\phi}}{\sqrt{2\pi}}, \quad m = 0, \pm1, \pm2, \ldots \tag{2.39}$$

and for the radial one

$$\frac{\mathrm{d}^2\mathcal{R}_{k,m}}{\mathrm{d}r^2} + \frac{1}{r}\frac{\mathrm{d}\mathcal{R}_{k,m}}{\mathrm{d}r} - \left[V(r) + w_{k,m}^2 + \frac{m^2}{r^2}\right]\mathcal{R}_{k,m} = 0 \tag{2.40}$$

where we have introduced two quantum numbers, m and k respectively angular and the radial number of excitations (in the future we will use $\{k, m\}$ as label for the eigenstates). The states are twofold degenerate in $\pm m$. It is important to remark that the number of bound states is finite and determined by the actual value of U_0.

2.3 DFT

In Sec. 1.6, we found that the total energy E, of a many-electron system under certain approximations can be written as

$$E = \langle\psi|\,\mathbb{H}\,|\psi\rangle \tag{2.41}$$

with

$$\mathbb{H} = \left[-\sum_i^{n_e}\frac{\hbar^2}{2m_e}\nabla_i^2 + \frac{1}{2}\sum_{i\neq j}^{n_e}\frac{q_e^2}{|\vec{r}_i - \vec{r}_j|} - \sum_j^{n_e}\mathbb{V}_n(\vec{r}_j)\right], \tag{2.42}$$

$$\mathbb{V}_n(\vec{r}) = \sum_i^{n_n}\frac{Zq_e^2}{|\vec{R}_i - \vec{r}|}. \tag{2.43}$$

Since the form of the Hamiltonian in Eq. 2.42 is independent from the properties of the considered system), every change in E is associated with a change of $|\psi\rangle$. Mathematically speaking, E is a functional of $|\psi\rangle$

$$E = \mathcal{F}[\psi]. \tag{2.44}$$

In the 1964 Hohenberg and Kohn observed that if E_0 is the minimum energy of the system (energy of the ground state), then E_0 is a functional only of the electron density n [63, 64, 65, 66, 67]

$$n(\vec{r}) = N_e\int|\psi(\vec{r}, \vec{r}_2, \ldots \vec{r}_{n_e}; \vec{R}_1 \ldots \vec{R}_{n_n})|^2\mathrm{d}\vec{r}_2 \ldots \mathrm{d}\vec{r}_{n_e}\mathrm{d}\vec{R}_1 \ldots \mathrm{d}\vec{R}_{n_n} \tag{2.45}$$

$$E_0 = \mathcal{F}[n], \tag{2.46}$$

this is false for the excited states [68]. This observation is named *Hohenberg-Kohn* theorem. The proof of the theorem is based on three steps

- The electronic density n determines uniquely $\mathbb{V}_n$
- For any quantum state, $\mathbb{V}_n$ determines uniquely $|\psi\rangle$
- $E = \mathcal{F}[\psi]$.

This could be summarized as $n \to \mathbb{V}_n \to |\psi\rangle \to E$ and consequently $E = \mathcal{F}[n]$. For proving the theorem, we have to prove every step. As said before, the third one is true, the second one means that if we change the atomic properties of the nuclei, the wavefunction changes, obviously this is true.

At this point, in order to prove the first assumption we proceed for reduction ad absurdum, thus we suppose that two differents external potential $\mathbb{V}_n$ could be associated with the same ground-state density n.

The total energy E can be written as

$$E = \left\langle \psi \middle| \sum_j \mathbb{V}_n(\vec{r}_j) \middle| \psi \right\rangle + \langle\psi| \mathbb{T} + \mathbb{V}_{ee} |\psi\rangle \tag{2.47}$$

and by using the definition of density in Eq. 2.45

$$E = \int \mathrm{d}\vec{r} n(\vec{r}) \mathbb{V}_n(\vec{r}) + \langle\psi| \mathbb{T} + \mathbb{V}_{ee} |\psi\rangle \,. \tag{2.48}$$

If we write the last equation for the ground state ($|\psi\rangle \to |\psi_0\rangle$, $E \to E_0$) and we suppose that it exists another potential $\mathbb{V}'_n \neq \mathbb{V}_n$ associated with the same density n we could define the quantities $\mathbb{H}'$, $|\psi\rangle'$ and E'. Of course, $|\psi\rangle$ is not the ground state of $\mathbb{H}'$, then

$$\langle\psi| \mathbb{H}' |\psi\rangle > E' \tag{2.49}$$

and remembering that $\mathbb{H}' = \mathbb{H} - \sum_j^{n_e} \mathbb{V}_n(\vec{r}_j) + \sum_j^{n_e} \mathbb{V}'_n(\vec{r}_j)$, we get

$$E_0 - E'_0 > \int \mathrm{d}\vec{r} n_0(\vec{r}) [\mathbb{V}_{n_0}(\vec{r}) - \mathbb{V}'_{n_0}(\vec{r})]. \tag{2.50}$$

The same procedure could be use for $\mathbb{H}$, starting from

$$\langle\psi'| \mathbb{H} |\psi'\rangle > E \tag{2.51}$$

we get

$$E'_0 - E_0 > \int \mathrm{d}\vec{r} n(\vec{r}) [\mathbb{V}'_{n_0}(\vec{r}) - \mathbb{V}_{n_0}(\vec{r})]. \tag{2.52}$$

by multiply the latest equation for -1, we get

$$E_0 - E'_0 < \int \mathrm{d}\vec{r} n_0(\vec{r}) [\mathbb{V}_{n_0}(\vec{r}) - \mathbb{V}'_{n_0}(\vec{r})]. \tag{2.53}$$

Therefore the premise that two different external potential could have the same density of the ground-state is absurd, and the Kohn-Honenberg theorem is proved.

2.3.1 Konh-Sham equation

The idea of Konh-Sham theory is that being $V_{n_0}(\vec{r})$ and E_0 a functional of n_0, we can use a system with the same number of non-interacting electrons with the same ground state density, in order to determine the properties of the system [69, 70, 71, 72, 73]. As written above, for a generic state $|\psi\rangle$

$$\mathbb{H} = \mathbb{T} + \int \mathrm{d}\vec{r} n(\vec{r}) \mathbb{V}_n(\vec{r}) + \mathbb{V}_{ee} \tag{2.54}$$

$$\mathbb{H} |\psi[\mathbb{V}_n]\rangle = E[\mathbb{V}_n] |\psi[\mathbb{V}_n]\rangle \tag{2.55}$$

$$E[\mathbb{V}_n] = \langle\psi[\mathbb{V}_n]| \mathbb{H} |\psi[\mathbb{V}_n]\rangle . \tag{2.56}$$

We already showed that for the ground state the functionals of $\mathbb{V}_n$ could be written as functionals of n, but now we want derive generally the form of the these equations as functionals of n. We start by taking the functional derivative of $E[\mathbb{V}_n]$ with respect $\mathbb{V}_n$

$$\frac{\delta E}{\delta \mathbb{V}_n} = \left\langle \frac{\delta\psi}{\delta \mathbb{V}_n} \middle| \mathbb{H} \middle| \psi \right\rangle + \left\langle \psi \middle| \mathbb{H} \middle| \frac{\delta\psi}{\delta \mathbb{V}_n} \right\rangle + \left\langle \psi \middle| \frac{\delta \mathbb{H}}{\delta \mathbb{V}_n} \middle| \psi \right\rangle . \tag{2.57}$$

From Eq. 2.54

$$\left\langle \psi \middle| \frac{\delta \mathbb{H}}{\delta \mathbb{V}_n} \middle| \psi \right\rangle = \langle\psi| \mathbb{n}(\vec{r}) |\psi\rangle = n(\vec{r}) \tag{2.58}$$

and by using

$$\mathbb{H} |\psi\rangle = E[\mathbb{V}_n] |\psi\rangle \tag{2.59}$$

$$\langle\psi| \psi\rangle = 1 \tag{2.60}$$

we get

$$\left\langle \frac{\delta\psi}{\delta \mathbb{V}_n} \middle| \mathbb{H} \middle| \psi \right\rangle + \left\langle \psi \middle| \mathbb{H} \middle| \frac{\delta\psi}{\delta \mathbb{V}_n} \right\rangle = E[\mathbb{V}_n] \frac{\delta 1}{\delta \mathbb{V}_n} = 0 \tag{2.61}$$

and consequently

$$\frac{\delta E}{\delta \mathbb{V}_n} = n(\vec{r}). \tag{2.62}$$

At this point, we can define the Legendre transform

$$F[n] = E[n] - \int \mathrm{d}\vec{r} n(\vec{r}) \mathbb{V}_n(\vec{r}) = \langle\psi[\mathbb{V}_n(\vec{r})]| \mathbb{T} + \mathbb{V}_{ee} |\psi[\mathbb{V}_n(\vec{r})]\rangle \tag{2.63}$$

where $\mathbb{V}_n(\vec{r})$ is a functional of n. Using Eq. 2.62 we easily find

$$\frac{\delta F}{\delta n(\vec{r})} = -\mathbb{V}_n(\vec{r}). \tag{2.64}$$

In order to derive the Kohn-Sham equation, we define a system of N_e non interacting electrons (this means that $\mathbb{V}_{ee} = 0$), with the same density of the previous system, described by the Konh-Sham Hamiltonian

$$\mathbb{H}_{KS} = \mathbb{T} + \int \mathrm{d}\vec{r} n(\vec{r}) \mathbb{V}_{KS}(\vec{r}). \tag{2.65}$$

The total energy of the ground state of Konh-Sham Hamiltonian takes the form of

$$E_{KS}[\mathbb{V}_{KS}(\vec{r})] = \left\langle \Phi[\mathbb{V}_{KS}(\vec{r})] \right| \mathbb{T} + \int \mathrm{d}\vec{r} n(\vec{r}) \mathbb{V}_{KS}(\vec{r}) \left| \Phi[\mathbb{V}_{KS}(\vec{r})] \right\rangle \tag{2.66}$$

where $\left| \Phi[\mathbb{V}_{KS}(\vec{r})] \right\rangle$ is the ground state wavefunction associated with the TISE determined by $\mathbb{H}_{KS}$. The Legendre transform becomes

$$F_{KS}[n] = E_{KS}[n] - \int \mathrm{d}\vec{r} n(\vec{r}) \mathbb{V}_{KS}(\vec{r}) = \langle \psi[\mathbb{V}_{KS}(\vec{r})] | \, \mathbb{T} \, | \psi[\mathbb{V}_{KS}(\vec{r})] \rangle \tag{2.67}$$

and the associated derivatives are

$$\frac{\delta E_{KS}}{\delta \mathbb{V}_{KS}} = n(\vec{r}) \tag{2.68}$$

$$\frac{\delta F_{KS}}{\delta n} = -\mathbb{V}_{KS}(\vec{r}) \tag{2.69}$$

by its particular structure $\frac{\delta F_{KS}}{\delta n}$ is usually denoted as $T_{KS}[n]$. Now, we can assume

$$F[n] = T_{KS}[n] + \frac{1}{2} \int \mathrm{d}\vec{r} \mathrm{d}\vec{r'} n(\vec{r}) n(\vec{r'}) \mathbb{v}_{ee}(|\vec{r} - \vec{r'}|) + E_{xc}[n] \tag{2.70}$$

where $E_{xc}[n]$ is the exchange correlation functional and

$$\mathbb{v}_{ee}(|\vec{r} - \vec{r'}|) = \frac{q_e^2}{|\vec{r} - \vec{r'}|}. \tag{2.71}$$

By using the previous differential equations and Eq. 2.70 we get

$$\mathbb{V}_{KS} = \mathbb{V}_n + \int \mathrm{d}\vec{r'} n(\vec{r'}) \mathbb{v}_{ee}(|\vec{r} - \vec{r'}|) + \mathbb{V}_{xc} \tag{2.72}$$

$$\mathbb{V}_{xc} = \frac{\delta E_{xc}}{\delta n} \tag{2.73}$$

this system of equations defines the exchange-correlation potential $\mathbb{V}_{xc}$.

The Konh-Sham Hamiltonian describes a system of non-interacting particles thus, the ground-state of the system can be written as an antisymmetrized product of single-particles orbitals $|\varphi_i(\vec{r})\rangle$.

Finally, we get the Konh-Sham equations system

$$E[n] = \sum_i \langle \varphi_i | \, \mathbb{t}_i \, | \varphi_i \rangle + \int \mathrm{d}\vec{r} n(\vec{r}) \mathbb{V}_n(\vec{r}) + \\ + \frac{1}{2} \int \mathrm{d}\vec{r} \mathrm{d}\vec{r'} n(\vec{r}) n(\vec{r'}) \mathbb{v}_{ee}(|\vec{r} - \vec{r'}|) + E_{xc}[n] \tag{2.74}$$

$$\left(\mathbb{t} + \mathbb{V}_n(\vec{r}) + \int \mathrm{d}\vec{r'} n(\vec{r'}) \mathbb{v}_{ee}(|\vec{r} - \vec{r'}|) + \mathbb{V}_{xc} \right) |\varphi_i\rangle = \epsilon_i \, |\varphi_i\rangle \, (\vec{r}) \tag{2.75}$$

$$n(\vec{r}) = \sum_i^{n_e} |\varphi_i(\vec{r})|^2. \tag{2.76}$$

As matter of fact, solving the original problem of N_e interacting electrons and N_n nuclei consists on solving the Konh-Sham problem making some approximation for evaluating the $\mathbb{V}_{xc}$, in general using self-consistent methods. In addition, it is possible to separate the exchange contribution and the correlation one $\mathbb{V}_{xc} = \mathbb{V}_x + \mathbb{V}_c$

2.3.2 Local density approximation

Since the development of the Konh-Sham theory various methods to evaluate the exchange correlation potential has been derived, in what follows we are going to use the simplest, that is named local density approximation (LDA) [74, 75, 76, 77]. This approximation consists on considering a homogeneous electron gas, which is a gas of electrons in a box with a constant nuclei potential and in which an electron feels the Coulomb repulsions due to the other electrons. For an homogeneous electron gas (HEG) we can calculate exactly the exchange potential, and numerically the correlation one. As first, we want to determine the exchange energy of a HEG, if our gas has not magnetic momentum

$$E_x = -\sum_{i,j} \int_V \mathrm{d}\vec{r} \int_V \mathrm{d}\vec{r'} \varphi_i^*(\vec{r}) \varphi_i(\vec{r'}) \varphi_j^*(\vec{r'}) \varphi_j(\vec{r}) \frac{q_e^2}{|\vec{r} - \vec{r'}|} \tag{2.77}$$

and by considering that under this condition the energy spectrum is continuum

$$E_x = -\frac{3}{4} \left(\frac{3}{\pi} \right)^{\frac{1}{3}} n^{\frac{4}{3}} V \tag{2.78}$$

where V is the volume of the box. In agreement with this theory the correlation energy assumes the form of

$$E_c = nV \cdot \begin{cases} 0.0311 \log(r_s) - 0.0480 + 0.002 r_s \log(r_s) - 0.0116 r_s & r_s < 1 \\ \dfrac{-0.1423}{1 + 1.0529\sqrt{r_s} + 0.3334 r_s} & r_s \geq 1 \end{cases} \tag{2.79}$$

where r_s is the Wigner-Seitz radius that can be defined as the radius of the sphere occupied on average by each electron $r_s = \left(\frac{3}{4\pi n} \right)^{\frac{1}{3}}$.

2.4 Interaction between matter and the electromagnetic field.

In this section, we want to derive classically the Hamiltonian of a particle in a strong electromagnetic field. Starting from the Newton's Law

$$\vec{F} = q \left(\vec{\mathcal{E}} + \frac{1}{c} \vec{v} \times \vec{B} \right) \tag{2.80}$$

in order to build the Hamiltonian, we need to know the conjugate momenta and thus we must find the Lagrangian first. Force and Lagrangian are related by the Euler-Lagrange equation

$$\frac{\mathrm{d}}{\mathrm{d}t} \left(\frac{\partial L}{\partial \vec{v}} \right) - \frac{\partial L}{\partial \vec{r}} = 0 \tag{2.81}$$

by substituting the Lagrangian in the Euler-Lagrange equation we find the Newton's Law of the system.

Thus, in order to prove that the Lagrangian describes correctly the system we have to prove that it gives the right form of the Newton's Law.

The appropriate Lagrangian for a particle in an electromagnetic field is

$$L = \frac{1}{2}mv^2 - q\Phi(\vec{r},t) + \frac{q}{c}\vec{v}\cdot\vec{A}(\vec{r},t), \tag{2.82}$$

and arises

$$\begin{aligned}\frac{\mathrm{d}}{\mathrm{d}t}\left(\frac{\partial L}{\partial v_x}\right) &= \frac{\mathrm{d}}{\mathrm{d}t}(mv_x + \frac{q}{c}A_x) = m\frac{\mathrm{d}v_x}{\mathrm{d}t} + \frac{q}{c}\frac{\mathrm{d}A_x}{\mathrm{d}t} = \\ &= m\frac{\mathrm{d}v_x}{\mathrm{d}t} + \frac{q}{c}\left(\frac{\mathrm{d}x}{\mathrm{d}t}\frac{\partial A_x}{\partial x} + \frac{\mathrm{d}y}{\mathrm{d}t}\frac{\partial A_x}{\partial y} + \frac{\mathrm{d}z}{\mathrm{d}t}\frac{\partial A_x}{\partial z} + \frac{\partial A_x}{\partial t}\right) = \\ &= m\frac{\mathrm{d}v_x}{\mathrm{d}t} + \frac{q}{c}\left(v_x\frac{\partial A_x}{\partial x} + v_y\frac{\partial A_x}{\partial y} + v_z\frac{\partial A_x}{\partial z} + \frac{\partial A_x}{\partial t}\right)\end{aligned} \tag{2.83}$$

$$\frac{\partial L}{\partial x} = -q\frac{\partial \Phi}{\partial x} + \frac{q}{c}\left(v_x\frac{\partial A_x}{\partial x} + v_y\frac{\partial A_y}{\partial x} + v_z\frac{\partial A_z}{\partial x}\right). \tag{2.84}$$

Thus, the Euler-Lagrange equation for the x-component gives

$$m\frac{\mathrm{d}v_x}{\mathrm{d}t} = -q\left(\frac{\partial \Phi}{\partial x} + \frac{1}{c}\frac{\partial A_x}{\partial t}\right) + \frac{q}{c}\left[v_y\left(\frac{\partial A_y}{\partial x} - \frac{\partial A_x}{\partial y}\right) + v_z\left(\frac{\partial A_z}{\partial x} - \frac{\partial A_x}{\partial z}\right)\right], \tag{2.85}$$

repeating the procedure for all the components and remembering that

$$\vec{\mathcal{E}} = -\boldsymbol{\nabla}\Phi - \frac{1}{c}\frac{\partial \vec{A}}{\partial t} \tag{2.86}$$

$$\vec{B} = \boldsymbol{\nabla} \times \vec{A} \tag{2.87}$$

we get the correct Newton's Law. We can calculate $\vec{P}$ the conjugate momentum to $\vec{r}$ as

$$\vec{P} = \frac{\partial L}{\partial \vec{v}} = m\vec{v} + \frac{q}{c}\vec{A} \tag{2.88}$$

and as consequence, we state that conjugate momentum $\vec{P}$ (or as said in the introduction canonical momentum) is formed by the kinetic momentum $\vec{p} = m\vec{v}$ and the field momentum $\frac{q}{c}\vec{A}$. Using a Legendre transformation, we easily get the Hamiltonian

$$\begin{aligned}H &= \vec{v}\cdot\vec{P} - L = \\ &= mv^2 + \frac{q}{c}\vec{v}\cdot\vec{A} - \frac{1}{2}mv^2 + q\Phi - \frac{q}{c}\vec{v}\cdot\vec{A} = \\ &= \frac{1}{2}mv^2 + q\Phi = \\ &= \frac{1}{2m}\left(\vec{P} - \frac{q}{c}\vec{A}\right)^2 + q\Phi\end{aligned} \tag{2.89}$$

In order to switch from the Hamiltonian equation to the Hamiltonian operator, we just have to turn some quantities into operator:

$$\mathbb{H} = \frac{1}{2m}\left(\vec{\mathbb{P}} - \frac{q}{c}\vec{A}(\boldsymbol{r}, t)\right)^2 + q\Phi(\vec{r}, t) \tag{2.90}$$

(where $\vec{A}$ and Φ are not operators.) The square produces:

$$\mathbb{H} = \frac{1}{2m}\left(\vec{\mathbb{P}}^2 + \frac{q^2}{c^2}\vec{A}^2(\vec{r}, t) - \frac{q}{c}\vec{A}(\vec{r}, t)\cdot\vec{\mathbb{P}} - \frac{q}{c}\vec{\mathbb{P}}\cdot\vec{A}(\vec{r}, t)\right) + q\Phi(\vec{r}, t) \tag{2.91}$$

The momentum operator is an example of a differential operator

$$\vec{\mathbb{P}} = -i\hbar\vec{\nabla} \tag{2.92}$$

In Coulomb's gauge:

$$\vec{\mathbb{P}}\cdot\vec{A}f = \vec{A}\cdot\vec{\mathbb{P}}f - i\hbar(\vec{\nabla}\cdot\vec{A})f = \vec{A}\cdot\vec{\mathbb{P}}f. \tag{2.93}$$

At this point because $\vec{A}$ is not an operator and because the coulombian potential $\Phi(\vec{r}, t)$ depends only upon $\vec{r}$, the $\mathbb{H}$ turns into:

$$\mathbb{H} = \frac{1}{2m}(\vec{\mathbb{P}}^2 + \frac{q^2}{c^2}\vec{A}^2(\vec{r}, t) - 2\frac{q}{c}\vec{A}(\vec{r}, t)\cdot\vec{\mathbb{P}}) + q\Phi(\vec{r}) \tag{2.94}$$

and according to the Maxwell equation:

$$\vec{A}(\vec{r}, t) = \vec{A}_0 e^{i(\vec{k}\cdot\vec{r} - \omega_L t)} \tag{2.95}$$

In order to absorb a photon, the electron must move in the presence of another particle (to preserve the total energy and momentum).

In addition we are going to work with wavelengths which are hundred times larger than the atomic distances so we can use the dipole approximation:

$$\vec{k}\cdot\vec{r} - \omega_L t = \frac{2\pi}{\lambda}\hat{k}\cdot\vec{r} - \omega_L t \approx -\omega_L t. \tag{2.96}$$

$\vec{A}$ is no longer dependent on r, as we know equations of motion do not change if we add to the Hamiltonian equation a time-dependent function, so we can delete the $\vec{A}^2$-term leaving the physical results unchanged.

Finally, the Hamiltonian operator of interaction:

$$\mathbb{H} = \frac{1}{2m}\vec{\mathbb{P}}^2 + q\Phi(\vec{r}) - \frac{q}{mc}\vec{A}(t)\cdot\vec{\mathbb{P}} \tag{2.97}$$

2.4.1 Gauge $\vec{\mathcal{E}}\cdot\vec{r}$

Actually, in this thesis we mostly use the Hamiltonian operator in the gauge $\vec{\mathcal{E}}\cdot\vec{r}$. Starting from the Hamiltonian (2.94), we make a gauge transformation:

$$\mathbb{Q} = \frac{q}{\hbar c}\vec{A}\cdot\vec{r}. \tag{2.98}$$

We apply the unitary operator $\mathbb{U}$ to the right of the Hamiltonian in the $\vec{A}\cdot\vec{\mathbb{P}}$ gauge.

$$\mathbb{U} = e^{-i\mathbb{Q}} \tag{2.99}$$

and to the left the complex conjugate. We obtain:

$$e^{i\mathbb{Q}}\mathbb{H}e^{-i\mathbb{Q}} = \frac{1}{2m}e^{i\mathbb{Q}}\vec{\mathbb{P}}^2e^{-i\mathbb{Q}} + e^{i\mathbb{Q}}q\Phi(\vec{r})e^{-i\mathbb{Q}} - \frac{q}{mc}e^{i\mathbb{Q}}\vec{A}(t)\cdot\vec{\mathbb{P}}e^{-i\mathbb{Q}} \tag{2.100}$$

$\vec{A}$ and Φ are multiplicative operators, so $\mathbb{U}$, which is not a differential operator, does not act on them $e^{i\mathbb{Q}}e^{-i\mathbb{Q}} = \mathbb{I}$ (where $\mathbb{I}$ is the unit matrix). Now we calculate its action on $\vec{\mathbb{P}}$ e $\vec{\mathbb{P}}^2$:

$$e^{i\mathbb{Q}}\vec{\mathbb{P}}e^{-i\mathbb{Q}} = -i\hbar e^{i\frac{q}{\hbar c}\vec{A}\cdot\vec{r}}\left(-i\frac{q}{\hbar c}\vec{A}e^{-i\frac{q}{\hbar c}\vec{A}\cdot\vec{r}} + e^{-i\frac{q}{\hbar c}\vec{A}\cdot\vec{r}}\vec{\nabla}\right) = -\frac{q}{c}\vec{A} + \mathbb{P} \tag{2.101}$$

$$\begin{aligned} e^{iQ}\vec{\mathbb{P}}^2e^{-i\mathbb{Q}} &= e^{i\mathbb{Q}}\vec{\mathbb{P}}e^{-i\mathbb{Q}}e^{i\mathbb{Q}}\vec{\mathbb{P}}e^{-i\mathbb{Q}} = \\ &= \left(-\frac{q}{c}\vec{A} + \vec{\mathbb{P}}\right)\cdot\left(-\frac{q}{c}\vec{A} + \vec{\mathbb{P}}\right) = \\ &= \vec{\mathbb{P}}^2 - \frac{2q}{c}\vec{A}\cdot\vec{\mathbb{P}} + \frac{q^2}{c^2}\vec{A}^2 \end{aligned} \tag{2.102}$$

where we have used equation (2.92).

$$\begin{aligned} \mathbb{H} = \frac{1}{2m}\left(\vec{\mathbb{P}}^2 - \frac{2q}{c}\vec{A}\cdot\vec{P} + \frac{q^2}{c^2}\vec{A}^2\right) &+ \frac{q}{mc}\vec{A}\cdot\left(-\frac{q}{c}\vec{A} + \vec{\mathbb{P}}\right) + \\ &+ \frac{q^2}{2mc^2}\vec{A}^2 + q\vec{\mathcal{E}}\cdot\vec{r} + q\Phi(\vec{r}) = \\ &= \frac{1}{2m}\vec{\mathbb{P}}^2 + q\Phi(\vec{r}) + q\vec{\mathcal{E}}\cdot\vec{r} \end{aligned} \tag{2.103}$$

We define:

$$\mathbb{H}_0 = \frac{1}{2m}\vec{\mathbb{P}}^2 + q\Phi(\vec{r}) \tag{2.104}$$

and:

$$\mathbb{V}(\vec{r},t) = q\vec{\mathcal{E}}\cdot\vec{r}, \tag{2.105}$$

thus the interaction Hamiltonian operator in two terms is

$$\mathbb{H} = \mathbb{H}_0 + \mathbb{V}(\vec{r},t) \tag{2.106}$$

2.5 Time dependent Schroedinger equation SAE.

As said in the final part of the previous section, the Hamiltonian of a quantum system driven by an intense laser in dipole approximation could be written as

$$\mathbb{H} = \mathbb{H}_0 + \mathbb{V}(\vec{r}, t) \tag{2.107}$$

where $\mathbb{H}_0$ is the unperturbed Hamiltonian. At this point, we can write the equations for our quantum ring when it is driven by a strong-laser field; in particular, for the plain ring:

$$\left(\frac{\mathbb{L}^2}{2m_eR^2} - q_e\vec{\mathcal{E}} \cdot \vec{r}\right) = i\hbar\frac{\partial}{\partial t}\left|\psi(t)\right\rangle \tag{2.108}$$

and for the SQR

$$\left(-\frac{\hbar^2}{2m_eR^2}\frac{\partial^2}{\partial\varphi^2} + V_0\cos\left(M\varphi\right) - q_e\vec{\mathcal{E}} \cdot \vec{r}\right)\left|\psi(t)\right\rangle = i\frac{\partial}{\partial t}\left|\psi(t)\right\rangle . \tag{2.109}$$

Special reference needs to be made to time dependent density functional theory (TDDFT), thus we are going to focus on it in the following.

2.5.1 Classical counterpart of quantum ring and chaos

As reported in the introduction, numerous features of the quantum phenomena in strong field physics can be modelled by studying the equation of motions associated with the classical counterpart of the quantum Hamiltonian. For the plain ring the classical version of the Hamiltonian is [62].

$$H = \frac{\ell^2}{2I} + U_0\cos(6\varphi) + R\mathcal{E}_0\cos(\varphi)\sin(\omega_L t) \tag{2.110}$$

and thus, the Newton's Law

$$\ddot{\varphi} = \frac{6U_0}{I}\sin(6\varphi) + \frac{R\mathcal{E}_0}{I}\sin(\varphi)\sin(\omega_L t) - 2\gamma\dot{\varphi} \tag{2.111}$$

where φ is the angular coordinate of the moving particle, ℓ the conjugate momentum (angular momentum), I the moment of inertia of the particle, $2U_0$ the depth of the potential of the structures, $R\mathcal{E}_0$ the maximum laser-particle interaction energy and ω_L the laser angular frequency. It is necessary to add a small dissipative term proportional to $\dot{\varphi}$ to neglect artificial instability [78].

For simplicity sake, we work with adimensional parameters, by defining the scaled time $\tau = \omega_L t$,in addition by substituting $a = \gamma/\omega_L$, $u = 6U_0/(I\omega_L^2)$, $v = R\mathcal{E}_0/I\omega_L^2$ we get

$$\begin{cases} \varphi' = \ell \\ \ell' + 2a\ell = u\sin(6\varphi) + v\sin(\varphi)\sin(\tau) \end{cases} \tag{2.112}$$

where the prime sign denotes derivative with respect to τ. The evolution in the phase space is represented by the two coordinates $\vec{\rho}(\tau) \equiv (\varphi(\tau), \ell(\tau))$. At this point, we are able to solve the previous system of differential equations by setting the initial conditions $\vec{\rho}(0) = (\varphi_0, \ell_0)$.

In literature, the semiclassical picture is mostly used to understand some features of phenomena of interaction between lasers and systems, explained by the three step model. Our model does not consider the possibility, for the electron, to go in the continuum, in any case, we can still have a similar effect when an electron from the neighborhood of a well, goes in and out from a different well.

Thus, we can still estimate the cutoff as the maximum of the kinetic energy in units of $R\mathcal{E}_0$

$$K \equiv \frac{L^2}{2IR\mathcal{E}_0} = \frac{\ell^2}{2v}. \tag{2.113}$$

2.6 Time Dependent Density Functional Theory

DFT is an extraordinary tool to solve many-body stationary problems, and thus to evaluate stationary quantities. However, most of the interesting atomic and molecular phenomena are time-dependent (TD), and in particular we are interested to study SFI. The DFT theory is based on the HK theorem that we demonstrate earlier, unfortunately this theorem is not valid for a TD arbitrary system.

This problem was solved by Runge and Gross (RG) [79], the RG theorem states that the time-independent density is a unique functional of the external potential for a given initial state. In order to report this theorem we write the Hamiltonian of the system as

$$\mathbb{H} = \mathbb{T} + \mathbb{V}_{ee} + \mathbb{V}_{ext}(t) \tag{2.114}$$

where $\mathbb{V}_{ext}(t)$ is a generic external time-independent potential. To demonstrate this theorem, we work in second quantization and consequently:

$$\mathbb{T} = -\frac{\hbar^2}{2m_e}\sum_s \int \mathrm{d}\vec{r}\,\mathbb{\Psi}_s^\dagger(\vec{r})\nabla^2\mathbb{\Psi}_s(\vec{r}) \tag{2.115}$$

$$\mathbb{V}_{ext}(t) = \sum_s \int \mathrm{d}\vec{r}\,v_{ext}(\vec{r},t)\mathbb{\Psi}_s^\dagger(\vec{r})\mathbb{\Psi}_s(\vec{r}) \tag{2.116}$$

$$\mathbb{V}_{ee} = \frac{1}{2}\sum_{s,s'}\int \mathrm{d}\vec{r}\int \mathrm{d}\vec{r'}\,v_{ee}(|\vec{r}-\vec{r'}|)\mathbb{\Psi}_s^\dagger(\vec{r})\mathbb{\Psi}_{s'}^\dagger(\vec{r'})\mathbb{\Psi}_{s'}(\vec{r'})\mathbb{\Psi}_s(\vec{r}). \tag{2.117}$$

where s and s' are the spin numbers. In general $v_{ee}(|\vec{r}-\vec{r'}|)$ is arbitrary, but in fact is more or less equal to the Coulomb repulsion (as written before). Thus, we can consider that some relations between the density and the current density are valid.

In this model the time dependent density can be written as

$$n(\vec{r},t) = \langle\psi(t)|\,\mathbb{n}(\vec{r})\,|\psi(t)\rangle \tag{2.118}$$

where the density operator is

$$\mathbb{n}(\vec{r}) = \sum_s \mathbb{\Psi}_s^\dagger(\vec{r})\mathbb{\Psi}_s(\vec{r}). \tag{2.119}$$

If we consider that our system evolves from the ground state $|\psi_0\rangle$ under the influence of $\mathbb{H}(t)$ in the state $|\psi(t)\rangle$, we can write the following continuity equation

$$\frac{\partial}{\partial t}n(\vec{r},t) = -\frac{i}{\hbar}\langle\psi(t)|\,[\mathbb{n}(\vec{r}),\mathbb{H}(t)]\,|\psi(t)\rangle = -\vec{\nabla}\cdot\vec{j}(\vec{r},t) \tag{2.120}$$

where the current density $\vec{j}(\vec{r},t)$ and the current operator $\mathbb{j}(\vec{r})$ are defined by

$$\vec{j}(\vec{r},t) = \langle\psi(t)|\,\mathbb{j}(\vec{r})\,|\psi(t)\rangle \tag{2.121}$$

$$\mathbb{j}(\vec{r}) = \frac{\hbar q_e}{2im_e}\sum_s\left\{\Psi_s^\dagger(\vec{r})\nabla\Psi_s(\vec{r}) - [\nabla\Psi_s^\dagger(\vec{r})]\Psi_s(\vec{r})\right\}. \tag{2.122}$$

The meaning of this continuity equation is the local consequence of the conservation of particle number, or by the means of the Gauss theorem that the number of particles within some volume can be found studying the current particle flux.

At this point, we consider the continuity equation for the current

$$\frac{\partial}{\partial t}\vec{j}(\vec{r},t) = \frac{-i}{\hbar}\langle\psi(t)|\,[\mathbb{j}(\vec{r}),\mathbb{H}(t)]\,|\psi(t)\rangle, \tag{2.123}$$

with some steps

$$\hbar\frac{\partial}{\partial t}j_\alpha(\vec{r},t) = -n(\vec{r},t)\frac{\partial}{\partial x_\alpha}v_{ext}(\vec{r},t) - \sum_\beta\frac{\partial}{\partial x_\beta}T_{\beta\alpha}(\vec{r},t) - \mathcal{F}_\alpha \tag{2.124}$$

where the stress momentum tensor $\mathbb{T}_{\beta\alpha}(\vec{r},t)$ is

$$\begin{aligned}\mathbb{T}_{\alpha,\beta} = \frac{\hbar^2}{2m_e}\sum_s\Bigg\{&\frac{\partial}{\partial x_\beta}\Psi_s^\dagger(\vec{r})\frac{\partial}{\partial x_\alpha}\Psi_s(\vec{r}) + \frac{\partial}{\partial x_\alpha}\Psi_s^\dagger(\vec{r})\frac{\partial}{\partial x_\beta}\Psi_s(\vec{r}) + \\ &-\frac{1}{2}\frac{\partial^2}{\partial x_\beta\partial x_\alpha}\Psi_s^\dagger(\vec{r})[\Psi_s(\vec{r})]\Bigg\}\end{aligned} \tag{2.125}$$

$$T_{\beta\alpha}(\vec{r},t) = \langle\psi(t)|\,\mathbb{T}_{\alpha,\beta}\,|\psi(t)\rangle \tag{2.126}$$

and the quantity $\mathcal{F}_\alpha$ is defined as

$$\mathbb{F}_\alpha = \sum_{s,s'}\int d\vec{r}'\Psi_s^\dagger(\vec{r})\Psi_{s'}^\dagger(\vec{r}')\frac{\partial}{\partial x_\alpha}v_{ee}(|\vec{r}-\vec{r}'|)\Psi_{s'}(\vec{r}')\Psi_s(\vec{r}) \tag{2.127}$$

$$\mathcal{F}_\alpha = \langle\psi(t)|\,\mathbb{F}_\alpha\,|\psi(t)\rangle. \tag{2.128}$$

By taking the divergence of both side of the continuity equation of the current density (Eq. 2.124) and by using the continuity equation for the density (Eq. 2.120) we get

$$\frac{\partial^2}{\partial t^2}n(\vec{r},t) = \boldsymbol{\nabla}\cdot[n(\vec{r},t)\boldsymbol{\nabla}v_{ext}(\vec{r},t)] + q(\vec{r},t) \tag{2.129}$$

where the operator $\mathbb{q}(\vec{r})$ is given by

$$\mathbb{q}(\vec{r}) = \sum_{\alpha,\beta}\frac{\partial^2}{\partial x_\beta\partial x_\alpha}\mathbb{T}_{\beta,\alpha}(\vec{r}) + \sum_\alpha\frac{\partial}{\partial x_\alpha}\mathbb{F}_\alpha(\vec{r}) \tag{2.130}$$

and the expectation value is defined at the usual way.

Eq.2.129 is very important due to fact that it represents the connection between electron density and external potential. It is important to make clear that $q(\vec{r},t)$ decays exponentially at infinity if $n(\vec{r},t)$ does the same, instead $v_{ext}(\vec{r},t)$ grows exponentially at infinity. In any case, we are going to analyze only bounded external potential defined in finite systems.

As first, we consider a system described by $\mathbb{H}(t)$ with an initial state $|\psi(t_0)\rangle = |\psi_0\rangle$ and we suppose that $n(\vec{r},t)$ is analytic at time t_0. With this considerations our system satisfies Eq. 2.129, at this point we can consider another Hamiltonian $\mathbb{H}'(t)$

$$\mathbb{H}'(t) = \mathbb{T} + \mathbb{V}'_{ext}(t) + \mathbb{V}'_{ee}; \tag{2.131}$$

if also in this case we define the initial state $|\psi'_0\rangle$ and if V'_{ee} with its derivatives are finite, we can write an analogous equation of Eq. 2.129

$$\frac{\partial^2}{\partial t^2} n'(\vec{r},t) = \boldsymbol{\nabla}\cdot[n'(\vec{r},t)\boldsymbol{\nabla} v'_{ext}(\vec{r},t)] + q'(\vec{r},t). \tag{2.132}$$

Now, we choose v'_{ext} is such a way that $n(\vec{r},t) = n'(\vec{r},t)$ and also $\frac{\partial^k}{\partial t^k} n'(\vec{r},t)|_{t=t_0} = \frac{\partial^k}{\partial t^k} n(\vec{r},t)|_{t=t_0}$. The idea it to build up the time expansion as Taylor series of v'_{ext} around the point t_0 for that

$$n'(\vec{r},t_0) = \langle\psi'_0|\, \mathbb{n}(\vec{r})\, |\psi'_0\rangle = \langle\psi_0|\, \mathbb{n}(\vec{r})\, |\psi_0\rangle = n(\vec{r},t_0), \tag{2.133}$$

due to fact that Eq.s 2.129,2.132 are second order differential equation we have to consider also

$$\frac{\partial}{\partial t} n'(\vec{r},t)|_{t=t_0} = \frac{\partial}{\partial t} n'(\vec{r},t)|_{t=t_0} = \left\langle\psi'_0\right| \boldsymbol{\nabla}\cdot\vec{\mathbb{j}}(\vec{r}) \left|\psi'_0\right\rangle = \left\langle\psi_0\right| \boldsymbol{\nabla}\cdot\vec{\mathbb{j}}(\vec{r}) \left|\psi_0\right\rangle, \tag{2.134}$$

where it has been used the continuity equation for the density.

For simplicity sake, we define

$$O^{(k)}(\vec{r}) := \frac{\partial^k}{\partial t^k} O(\vec{r},t)|_{t=t_0}, \tag{2.135}$$

where $O(\vec{r},t)$ is a generic expectation value, and consequently we can rewrite Eq. 2.132 as

$$n'^{(2)}(\vec{r}) = \boldsymbol{\nabla}\cdot[n'^{(0)}(\vec{r})\boldsymbol{\nabla} v'^{(0)}_{ext}(\vec{r})] + q'^{(0)}(\vec{r}). \tag{2.136}$$

Since we require $n^{(k)} = n'^{(k)}$ for all k, we find

$$\boldsymbol{\nabla}\cdot[n^{(0)}(\vec{r})\boldsymbol{\nabla} v'^{(0)}_{ext}(\vec{r})] = n^{(2)}(\vec{r}) - q'^{(0)}(\vec{r}). \tag{2.137}$$

If we define the boundary condition $v'^{(0)}_{ext}(\vec{r}) \to 0$ for $r \to \infty$, the latest Sturm-Liouville type equation admits an unique solution.

Thus we got $v'^{(0)}_{ext}$, for getting a generic order $v'^{(k)}_{ext}$ we have to solve the equation

$$n'^{(k+2)}(\vec{r}) = q'^{(k)}(\vec{r}) + \sum_{l=0}^{k} \binom{k}{l} \boldsymbol{\nabla}\cdot[n'^{(k-l)}(\vec{r})\boldsymbol{\nabla} v'^{(l)}_{ext}(\vec{r})], \tag{2.138}$$

and using $n'^{(k)} = n^{(k)}$ we get

$$\boldsymbol{\nabla}\cdot[n^{(0)}(\vec{r})\boldsymbol{\nabla} v'^{(k)}_{ext}(\vec{r})] = n^{(k+2)}(\vec{r}) - q'^{(k)}(\vec{r}) - \sum_{l=0}^{k-1} \binom{k}{l} \boldsymbol{\nabla}\cdot[n'^{(k-l)}(\vec{r})\boldsymbol{\nabla} v'^{(l)}_{ext}(\vec{r})]. \tag{2.139}$$

The right side of this Eq. 2.139 is uniquely determined due to fact that we know the solution for $l = 0$ of $v_{ext}^{\prime(l)}$ and we are able to recursively determinate the other orders. Thus we can build up $v'_{ext}(\vec{r}, t)$ as Taylor series

$$v'_{ext}(\vec{r}, t) = \sum_{k=0}^{\infty} \frac{1}{k!} (t - t_0)^k v_{ext}^{\prime(k)}(\vec{r}, t_0) \tag{2.140}$$

and for the analyticity of $v'_{ext}(\vec{r}, t)$ around t_0 we can conclude that we are able to determine the requested $v'_{ext}(\vec{r}, t)$ within the convergence radius of the Taylor series around t_0. In order to determine this quantity in all the time space we have only to use another point t_1 in the radius of convergence of the previous Taylor series and we have to use it as initial state of another Taylor series. In this way, we are able to completely determine $v'_{ext}(\vec{r}, t)$ for all t.

Thus, if we have a density $n(\vec{r}, t)$ obtained by a Hamiltonian $\mathbb{H}$ with an initial state $|\psi_0\rangle$ and if we use another many-particle system with a two-particle interaction V'_{ee}, in such a way that, for this system with initial state $|\Psi'_0\rangle$, it is valid $n'^{(k)} = n^{(k)}$, there is only an external potential v'_{ext} that reproduces the given density $n(\vec{r}, t)$.

This proves that for this kind of system, it is always possible define a Konh-Sham potential [80]. The case with the same initial state for both the system is the well know RG theorem, thus this demonstration could be considered and extension of the traditional one. The central theorem of TDDFT states that there is a one-to-one correspondence between $v_{ext}(\vec{r}, t)$ and the one-body density $n(\vec{r}, t)$.

2.6.1 Density Response Function.

Let us consider a system of interacting particle initially in its ground-state and a perturbation starting at $t = 0$, where the perturbation is given by [81]

$$\mathbb{V}_L = \mathcal{E}(t) \sin(\omega_L t) \sum_{j=1}^{N} \vec{r}_j \cdot \vec{\alpha} \tag{2.141}$$

where α is the polarization vector. We can write the total potential as

$$\begin{cases} v_{ext}(\vec{r}, t) = v_{ext}(\vec{r}, 0) + \delta v_{ext}(\vec{r}, t) & t > 0 \\ v_{ext}(\vec{r}, t) = v_{ext}(\vec{r}, 0) & t \leq 0, \end{cases} \tag{2.142}$$

thus any observables could be written as a Taylor series with respect δv_{ext}, and consequently the density is

$$n(\vec{r}, t) = \sum_{l=0}^{\infty} \frac{1}{l!} \int \mathrm{d}\vec{r}\mathrm{d}t \ldots \mathrm{d}\vec{r}_l \mathrm{d}t_l \chi^{(l)}(\vec{r}, t; \ldots; \vec{r}_l, t_l) \delta v_{ext}(\vec{r}, t) \ldots \delta v_{ext}(\vec{r}_l, t_l) \tag{2.143}$$

where the response function at order l is

$$\chi^{(l)}(\vec{r}, t; \ldots; \vec{r}_l, t_l) = \left. \frac{\delta^l n(\vec{r}, t)}{\delta v_{ext}(\vec{r}_1, t_1) \ldots \delta v_{ext}(\vec{r}_l, t_l)} \right|_{v_{ext}(\vec{r}, 0)} . \tag{2.144}$$

At first order we get the linear response equations system

$$n_1(\vec{r},t) = \int \mathrm{d}t' \int \mathrm{d}\vec{r} \chi(\vec{r},t;\vec{r}_1,t_1)\delta v_{ext}(\vec{r}_1,t_1) \tag{2.145}$$

$$\chi(\vec{r},t;\vec{r}_1,t_1) = \left.\frac{\delta n(\vec{r},t)}{\delta v_{ext}(\vec{r}_1,t_1)}\right|_{v_{ext}(\vec{r},0)}. \tag{2.146}$$

We can rewrite the response function as

$$\chi(\vec{r},t;\vec{r}_1,t_1) = -i\Theta(t-t_1) \langle\psi_0| \left[\mathbb{n}_{H_0}(\vec{r},t), \mathbb{n}_{H_0}(\vec{r}_1,t_1)\right] |\psi_0\rangle \tag{2.147}$$

where $\Theta(\tau)$ is the step function and

$$\mathbb{n}_{H_0}(\vec{r},t) = e^{i\frac{\mathbb{H}t}{\hbar}} \mathbb{n}(\vec{r}) e^{-i\frac{\mathbb{H}t}{\hbar}}. \tag{2.148}$$

By Fourier transforming the equation, by inserting the identity derived by the continuity equation, we get the spectral decomposition

$$\begin{aligned}\chi(\vec{r},\vec{r}_1,\omega) = \lim_{\epsilon\to 0^+} \sum_I \Bigg[& \frac{\langle\psi_0| \mathbb{n}(\vec{r}) |\psi_I\rangle \langle\psi_I| \mathbb{n}(\vec{r}) |\psi_0\rangle}{\hbar\omega - \hbar\omega_{0,I} + i\epsilon} + \\ & - \frac{\langle\psi_0| \mathbb{n}(\vec{r}) |\psi_I\rangle \langle\psi_I| \mathbb{n}(\vec{r}) |\psi_0\rangle}{\hbar\omega + \hbar\omega_{0,I} + i\epsilon} \Bigg]\end{aligned} \tag{2.149}$$

where the sum goes over all the excited interacting states I and $E_I = \hbar\omega_I = \hbar\omega_{0,I} + \hbar\omega_0$.

It is very heavy to calculate the linear response as defined by Eq.2.149, but by using the RG theorem we can work with a Kohn-Sham equation. The response function is a functional of n_{GS}, thus we can substitute our system with the Kohn-Sham system of non-interacting electrons, with the same groundstate density. Thus, the first order density response function becomes

$$n_1(\vec{r},t) = \int \mathrm{d}t_1 \int \mathrm{d}\vec{r}_1 \chi_{KS}(\vec{r},t;\vec{r}_1,t_1)\delta v_{KS}(\vec{r}_1,t_1) \tag{2.150}$$

where δv_{KS} is the perturbation to the effective Konh-Sham potential, and $\chi_{KS}(\vec{r},t;\vec{r}_1,t_1)$ is the response function of a system of non-interacting particle with unperturbed density n_{GS}. The spectral decomposition for the Kohn-Sham response function is

$$\chi_{KS}(\vec{r},\vec{r}_1,\omega) = \lim_{\eta\to 0^+} \sum_{l,j} (f_l - f_j)\delta_{s_l,s_j} \frac{\varphi_l^{(0)*}(\vec{r})\varphi_j^{(0)}(\vec{r})\varphi_j^{(0)*}(\vec{r}_1)\varphi_l^{(0)}(\vec{r}_1)}{\hbar\omega - (\epsilon_j - \epsilon_l) + i\eta} \tag{2.151}$$

where $\varphi_j^{(0)}(\vec{r})$ are the ground state Konh-Sham orbitals, the fs are the Fermi occupation factors and s_l is the spin orientation of the l-th orbital.

The problem of the previous equation is that the poles of the Kohn-Sham response are at the energies of the Kohn-Sham eigenvalues that are not the same energies of the system with interacting electrons. Thus we need to get $\chi(\vec{r},t;\vec{r}_1,t_1)$ from the Kohn-Sham response.

Everything becomes clear when we write down the first-order variation for the TD Kohn-Sham potential

$$\delta v_{KS}(\vec{r},t) = \delta v_{ext}(\vec{r},t) + \int \mathrm{d}\vec{r}_1 \frac{n_1(\vec{r}_1,t)}{|\vec{r}-\vec{r}_1|} + \\ + \int \mathrm{d}t_1 \int \mathrm{d}\vec{r}_1 n_1(\vec{r}_1,t_1) \left.\frac{\delta v_{xc}(\vec{r},t)}{\delta n(\vec{r}_1,t_1)}\right|_{n=n_{GS}} \tag{2.152}$$

At this point by using Eq.s (2.145,2.150,2.151), we get that the linear response for the interacting system is

$$\chi[n_{GS}](\vec{r},t,\vec{r}_1,t) = \chi_{KS}[n_{GS}](\vec{r},t,\vec{r}_1,t_1) + \\ + \int \mathrm{d}t_2 \int \mathrm{d}\vec{r}_2 \int \mathrm{d}t_3 \int \mathrm{d}\vec{r}_3 \chi_{KS}[n_{GS}](\vec{r},t,\vec{r}_2,t_2) \times \\ \times \left[\frac{\delta_{t_2,t_3}}{|\vec{r}_2-\vec{r}_3|} + \left.\frac{\delta v_{xc}(\vec{r}_2,t_2)}{\delta n(\vec{r}_3,t_3)}\right|_{n=n_{GS}} \right] \chi_{KS}[n_{GS}](\vec{r}_3,t_3,\vec{r}_1,t_1). \tag{2.153}$$

For our goal, we state that the time-dependent Konh-Sham equations yield the exact density, including non linear effects. As we are going to see in the next section, in order to evaluate the spectrum for strong field interaction we need to evaluate the dipole moment

$$\vec{d}(t) = \int \mathrm{d}\vec{r} q_e \vec{r} n(\vec{r},t) \tag{2.154}$$

or the averaged electronic acceleration $\vec{a}(t)$.

2.7 Electrons, strong field and quantum mechanical properties.

We suppose to have a charge q, moving along a trajectory $\vec{s}(t)$ with an acceleration $\vec{a}(t) = \frac{\mathrm{d}^2\vec{s}}{\mathrm{d}t^2}$, if the velocity of the particle is not relativistic, our moving object generates an electric field that for a far away observation point $\vec{r}$ is given by (see Fig. 2.4)

$$\vec{\mathcal{E}}(\vec{r},t) = \frac{q}{c^2} \left[\frac{\hat{n} \times (\hat{n} \times \vec{a})}{|\vec{r}-\vec{s}|} \right]_{\bar{t}} \tag{2.155}$$

where $\bar{t} : |\vec{r} - \vec{s}(\bar{t})| = c(t - \bar{t})$ is the retarded time, $\hat{n}$ is the unit vector representing the direction from $\vec{s}(\bar{t})$ to $\vec{r}$ (in the previous equation all time dependent quantities must be calculate at $\bar{t}$). As we stated above, the observation point is far away, thus from the observer point of view $\hat{n}$ can be consider a constant vector and $|\vec{r} - \vec{s}| \cong r$.

Thus, finally our equation becomes

$$\vec{\mathcal{E}}(\vec{r},t) = \frac{q}{c^2 r} \{[\hat{n} \cdot \vec{a}(\bar{t})]\hat{n} - \vec{a}(\bar{t})\}, \tag{2.156}$$

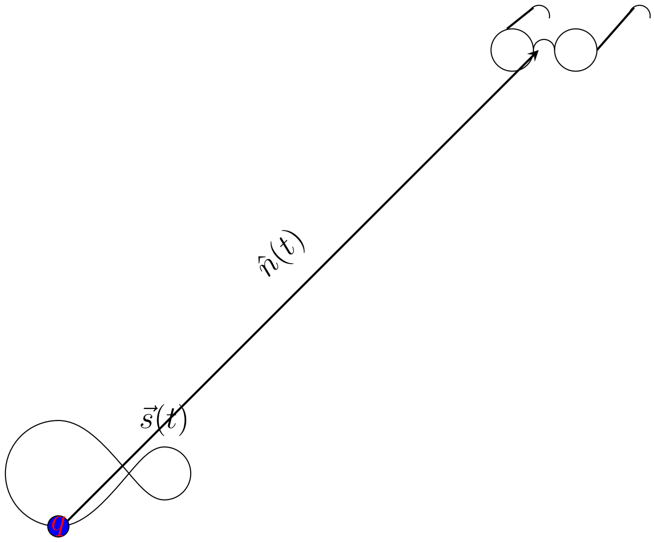

Figure 2.4: Schematic representation of a particle of charge q moving in a trajectory $\vec{s}(t)$ and an observer positioning along the $\hat{n}(t)$ direction.

as consequences of the form of this equation we can state that $\vec{\mathcal{E}}$ depends on the observant position thus, we get different plain of the emitted field by varying $\hat{n}$ and the polarization state of the emitted radiation depends only on $\vec{a}$ [32].

In order to analyze the emitted radiation, we are interested in knowing the Fourier transform of the field

$$\vec{\mathcal{E}}(\vec{r},t) = \frac{1}{\sqrt{2\pi}} \int_{-\infty}^{+\infty} e^{i\omega t} \vec{\mathcal{E}}(\vec{r},\omega) d\omega \tag{2.157}$$

where $\vec{\mathcal{E}}(\vec{r},\omega)$ is a complex vector. The field at frequency ω is

$$\vec{\mathcal{E}}(\vec{r},t) = |\mathcal{E}(\vec{r},\omega)| \cos(\omega t + \alpha) \hat{\mathcal{E}} \tag{2.158}$$

where the phase α is in general different for any components of $\vec{\mathcal{E}}(\vec{r},t)$ and $\hat{\mathcal{E}}$ is the versor in the direction of the electric field.

For $\hat{n} = \hat{z}$, the Stokes parameters, which give a quantitative picture of the polarization at a fixed frequency [82], can be written as

$$\tan 2\Psi = \frac{2\mathcal{E}_x(\omega)\mathcal{E}_y(\omega)\cos(\delta)}{\mathcal{E}_x^2(\omega) - \mathcal{E}_y^2(\omega)} \tag{2.159}$$

$$e_c = |\tan \chi| \tag{2.160}$$

$$\tan 2\chi = \frac{2\mathcal{E}_x(\omega)\mathcal{E}_y(\omega)\sin(\delta)}{\sqrt{[\mathcal{E}_x^2(\omega) + \mathcal{E}_y^2(\omega)]^2 - 4\mathcal{E}_x^2(\omega)\mathcal{E}_y^2(\omega)\sin^2(\delta)}} \tag{2.161}$$

where $\vec{\mathcal{E}}(\omega) \equiv |\mathcal{E}(\vec{r},\omega)|\hat{\mathcal{E}}$ (since the observer is very far away compared to the dimension of the system, $\vec{r}$ dependence is omitted); $\delta \equiv \alpha_x - \alpha_y$ is the phase between the two field components; $0 \leq \Psi \leq \pi$ is the angle between the major axis of the polarization ellipse and the x-direction, e_c is the ellipticity and $-\pi/4 \leq \chi \leq \pi/4$ is an auxiliary parameter ($\tan\chi = \pm B/A$, where A and B are the major and the minor axes of the polarization ellipse) [82].

At this point, we can evaluate the energy emitted in the range between $[\omega, \omega + d\omega]$, in the total interaction time

$$S(\omega) = \frac{4q^2}{3c^3}|\vec{a}(\omega)|^2. \tag{2.162}$$

It is important to stress again that by the means of Eq. 2.156, the position of the observer selects the measured ellipse of the emitted radiation thus all the previous quantities changing by varying the observer location.

The theory here outlined is based on classical grounds, but for our scope it suffices to substitute this classical quantities with the correspondent quantum averaged ones.

$S(\omega)$ does not provide any temporal information about the emission of a particular frequency during the interaction time, but just the total emission at that frequency. The main mathematical motivation of this is the fact that we have used the Fourier transformation. A way to solve this problem is to change in our theory this transformation with a windowed version of it. Thus, we generalize the Fourier definition by resorting to the Morlet transform of the acceleration, defined as

$$\begin{cases} \vec{a}(t_0;\omega) = \int_{-\infty}^{\infty} \vec{a}(t) M(t_0;\omega,t)\mathrm{d}t \\ M(t_0;\omega,t) = \sqrt{\omega}\left\{e^{-i[\omega(t-t_0)]} - e^{-\sigma_0^2/2}\right\} e^{-\omega^2(t-t_0)^2/(2\sigma_0^2)} \end{cases} \tag{2.163}$$

where σ_0 is the number of oscillations at frequency ω within the Gaussian width and t_0 represents the time for which we require information[83, 84]; $\vec{a}(t_0;\omega)$ can be interpreted as the frequency content of the acceleration at time t_0. Coherently we make the substitutions $\vec{a}(\omega) \rightarrow \vec{a}(t_0;\omega)$, $\delta \rightarrow \delta(t_0)$, $\chi(\omega) \rightarrow \chi(t_0;\omega)$, $e_c(\omega) \rightarrow e_c(t_0;\omega)$ $\Psi(\omega) \rightarrow \Psi(t_0;\omega)$, $\mathcal{E}_j(\omega) \rightarrow \mathcal{E}_j(t_0;\omega)$ and assume that they give the time dependence of the associated time independent quantities .

2.8 PAD and TDDFT: the surface method.

In the following, we are going to evaluate the ARPES by using TDDFT and the Surface flux method [85, 86, 87]. As in the introduction, we consider the general solution for an ejected electron by a quantum system as summation of Volkov states

$$|\Psi(t)\rangle = \sum_p b(\vec{p}) \left|\psi_V^{\vec{p}}(t)\right\rangle \tag{2.164}$$

$$b(\vec{p}) = \left\langle \psi_V^{\vec{p}}(t)\right| \Psi(t)\right\rangle \tag{2.165}$$

$$\left|\psi_V^{\vec{p}}(\tau)\right\rangle = e^{-\frac{i\tau}{\hbar}\left(\frac{P^2}{2m_e}+\int_0^\tau \mathrm{d}t' H_I(t')\right)} |\vec{p}\rangle \tag{2.166}$$

$|b(\vec{p})|^2$ is the density probability to find a particle with momentum $\vec{p}$. As said before the well known Volkov states are the solutions of the time dependent Schroedinger equation, for a free particle moving in an electromagnetic field

$$i\hbar\frac{\partial}{\partial t}\left|\psi_V(t)\right\rangle = \frac{1}{2m_e}\left[\vec{\mathbb{p}} - \frac{q_e}{c}\vec{A}(t)\right]^2 \left|\psi_V(t)\right\rangle = \mathbb{H}_V \left|\psi_V(t)\right\rangle . \tag{2.167}$$

By definition we can write

$$b(\vec{p}) = \int_0^T \left(\frac{\mathrm{d}}{\mathrm{d}t}\left\langle \psi_V^{\vec{p}}(t)\right| \Psi(t)\Big\rangle\right)\mathrm{d}t; \tag{2.168}$$

at this point we make the strong assumptions of this method, which consists in supposing that for a certain position in the space at distance $r \geq r_c$ the Hamiltonian in the TDSE equation

$$i\hbar\frac{\partial}{\partial t}\left|\psi(t)\right\rangle = \frac{1}{2m_e}\left[\vec{\mathbb{p}} - \frac{q_e}{c}\vec{A}(t)\right]^2 \left|\psi(t)\right\rangle + V(\vec{r},t)\left|\psi(t)\right\rangle = \mathbb{H}\left|\psi(t)\right\rangle . \tag{2.169}$$

can be taken equal to Volkov Hamiltonian $\mathbb{H}(t) = \mathbb{H}_V(t)$ (see Eq. 1.21). Finally, by decomposing $\left|\psi_V^{\vec{p}}(t)\right\rangle$ in spherical harmonics $\left|lm(\Omega_k)\right\rangle$ we get the $b(\vec{p})$:

$$\begin{aligned} b(\vec{p}) = {} & -\frac{i4\pi r_c^2}{2(2\pi)^{3/2}}\sum_{lm}(-i)^l j_l(kr)\left|lm(\Omega_k)\right\rangle \int \mathrm{d}t e^{\frac{i}{2}\int_0^t [\vec{p}-\vec{A}(t)]^2 \mathrm{d}\tau} \times \\ & \times \left\{\left(-i\vec{p} + 2i\frac{\vec{A}}{c}\right)\int \mathrm{d}\Omega_r \left\langle lm(\Omega_r)\right|\hat{r}\left|\Psi(t)\right\rangle - \int \mathrm{d}\Omega_r \left\langle lm(\Omega_r)\right|\frac{\partial}{\partial r}\left|\Psi(t)\right\rangle\right\}. \end{aligned} \tag{2.170}$$

where we have used atomic units.

Compared with other methods (like mask method or sampling point method [88, 89, 90, 87]), this method allows to fine study the diffraction patterns of the molecules and to reduce the calculations time improving the accuracy.

3
Results

In the previous chapters we introduced the reader into the world of SFI, in this chapter, we finally show him our results.

3.1 Plain ring

As first, we want to show some ground state results. As shown in the Theory chapter, for a plain 1D quantum ring (Eq. 2.1), the eigenfunctions and the eigenenergies can be analytically calculated (Eq.s 2.2,2.3).

In Fig. 3.1 we show the eigenstates $\Phi_{+\ell}(\varphi)$ for $\ell = 0, 1, 2$, it is important to stress that $\Phi_{-\ell}(\varphi)$ have the same real part as $\Phi_{+\ell}(\varphi)$ and the imaginary part is $\Im(\Phi_{-\ell}(\varphi)) = -\Im(\Phi_{+\ell}(\varphi))$, thus we only report the first one in the plot in order to show the behaviour.

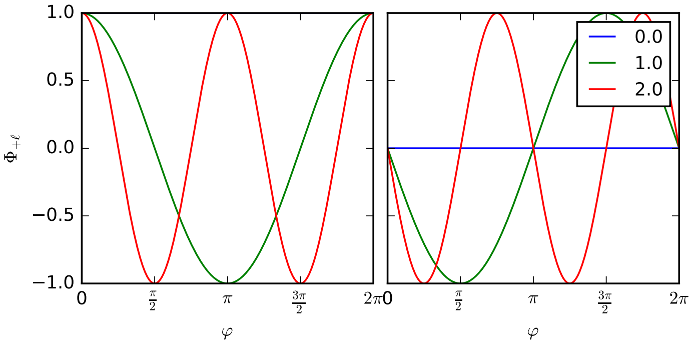

Figure 3.1: Eigenstates of a plain ring with $\ell = 0, 1, 2$. In the left side the real part of $|\Phi_{\pm\ell}\rangle$, and in the right part the imaginary part of $|\Phi_{+\ell}\rangle$.

The high symmetry of these eigenstates have important consequences when we study the interaction of this system with a laser.

3.2 Structured quantum ring.

As stated in the theoretical chapter (see Sec. 2.1.2), the behaviour of eigenvalues for the SQR is well determined by M (number of dots in the ring).

In Fig. 3.2, we report the eigenvalues for $M = 3, 4, 6, 8$, and in Fig.(3.3) a scheme explaining the degeneration rules for a generic M.

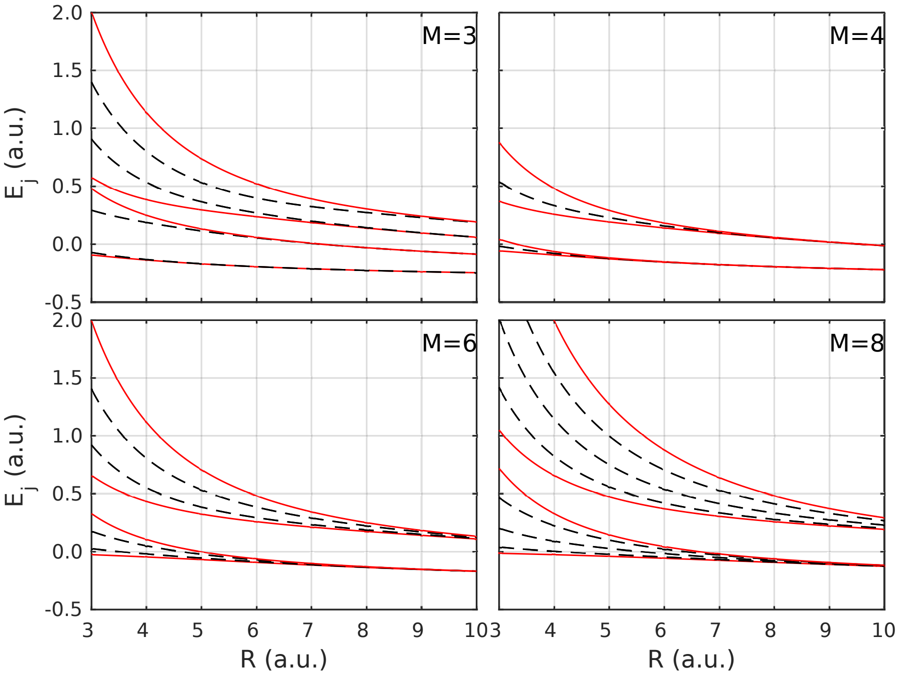

Figure 3.2: E_j (eigenvalues of 1D model) vs R for $V_0 = 0.33$ a.u., the red continuous lines represent the non-degenerate eigenvalues and the black dotted ones the degenerate. In the top row we report respectively the graphs for $M = 3$ (left), and $M = 4$ (right), in the bottom row those for $M = 6$ (left) and $M = 8$ (right).

By using the analytic method of Sec. 2.1.2 we are able to evaluate the eigenvalues and eigenfunction as function of q; for example, in the top side of Fig. 3.4 we show the behaviour of the eigenvalues for $M = 6$.

Once again, both from Fig. 3.4 and the top side of Fig. 3.5 we find that the degeneration rules are the ones analytically evaluated in the previous chapter. In the lower 4 subplot of both Fig.s 3.5 and 3.4 we show the eigenstates for $0 \leq j \leq N$ respectively for $M = 3$ and 6. All the eigenstates are normalized.

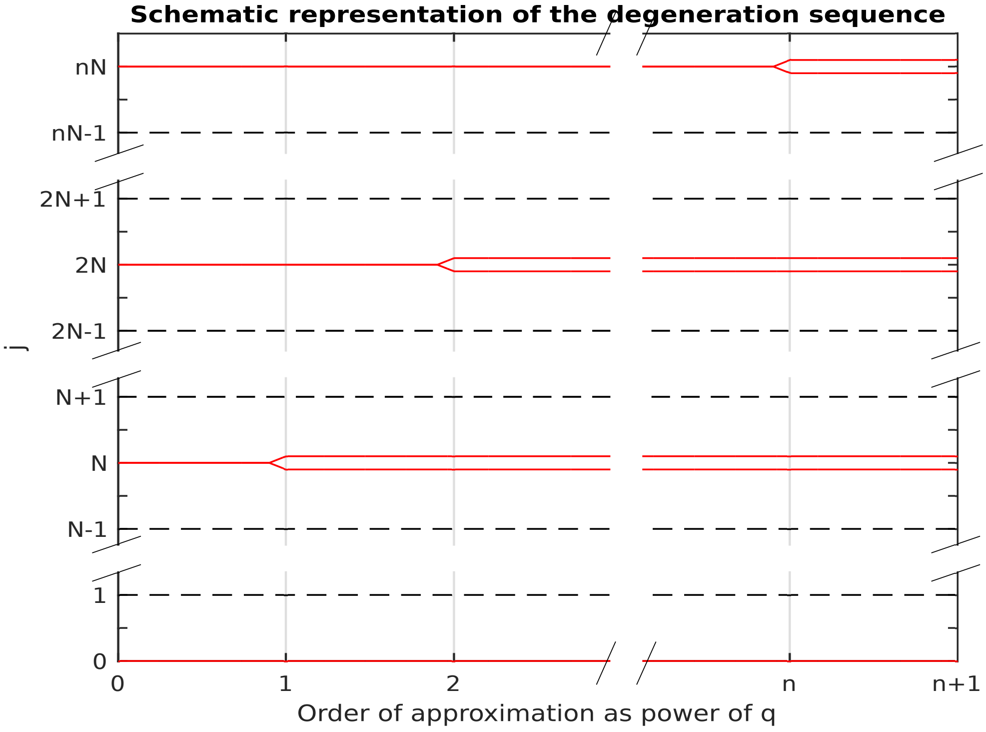

Figure 3.3: Schematic representation of the non-degeneration rule (Eq.2.31). We report j (eigenvalues index) vs the order of approximation as power of q for M even, $N = \frac{M}{2}$ and $M > 2$; the red continuous lines represent the non-degenerate eigenvalues and the black dotted ones the degenerate. We show that the non degenerate eigenvalues are multiples of N and that any couple of eigenvalues ($a_j^{(N)}$ and $b_j^{(N)}$) with $j > nN$ appears not split to the n order of approximation.

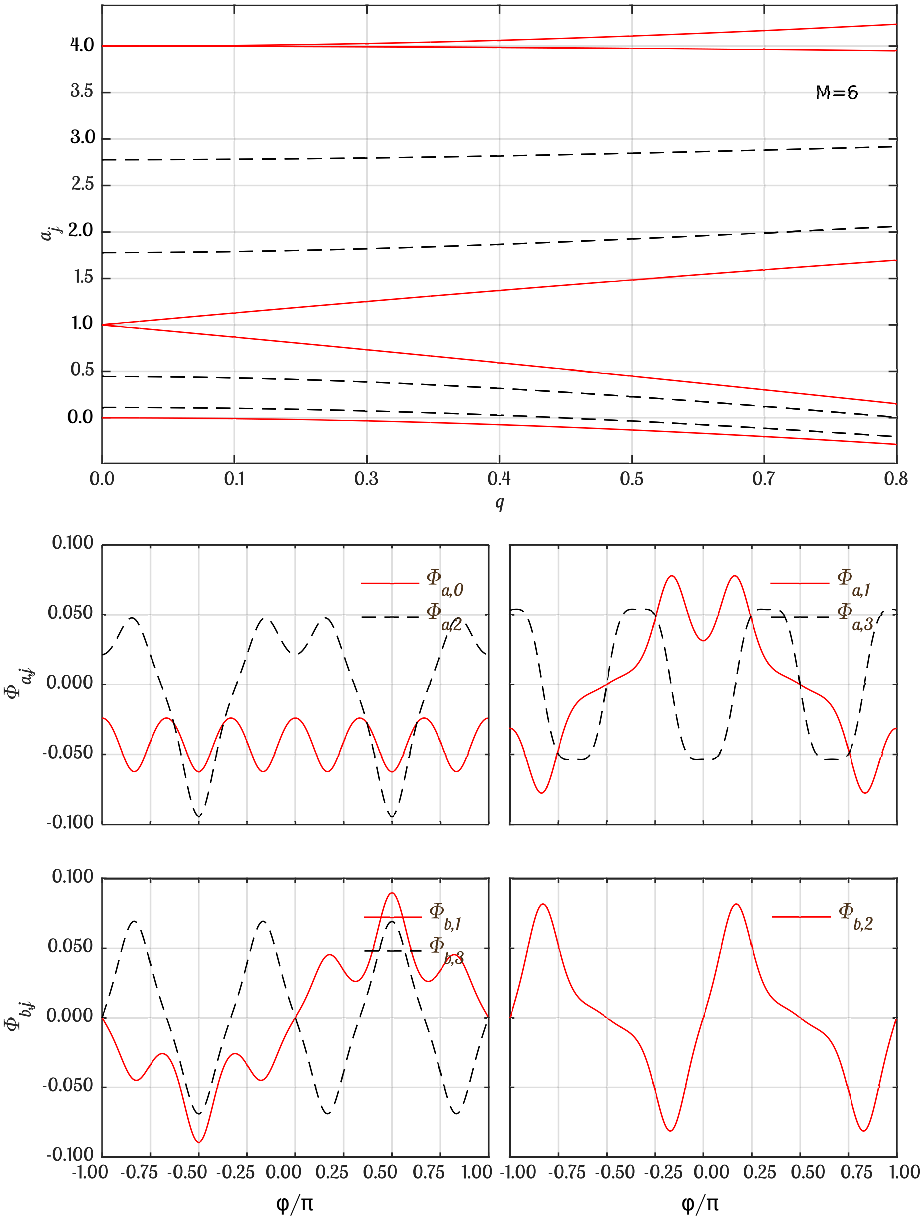

Figure 3.4: First row: a_j vs q for $M = 6$; second row: $\Phi_{a,j}$ vs φ/π for $M = 6$, $q = 1$ and $0 \leq j \leq 3$; third row: $\Phi_{b,j}$ vs φ/π for $M = 6$, $q = 1$ and $0 < j \leq 3$. The eigenstates with $j = 0, 3$ are non-degenerate the others are degenerate.

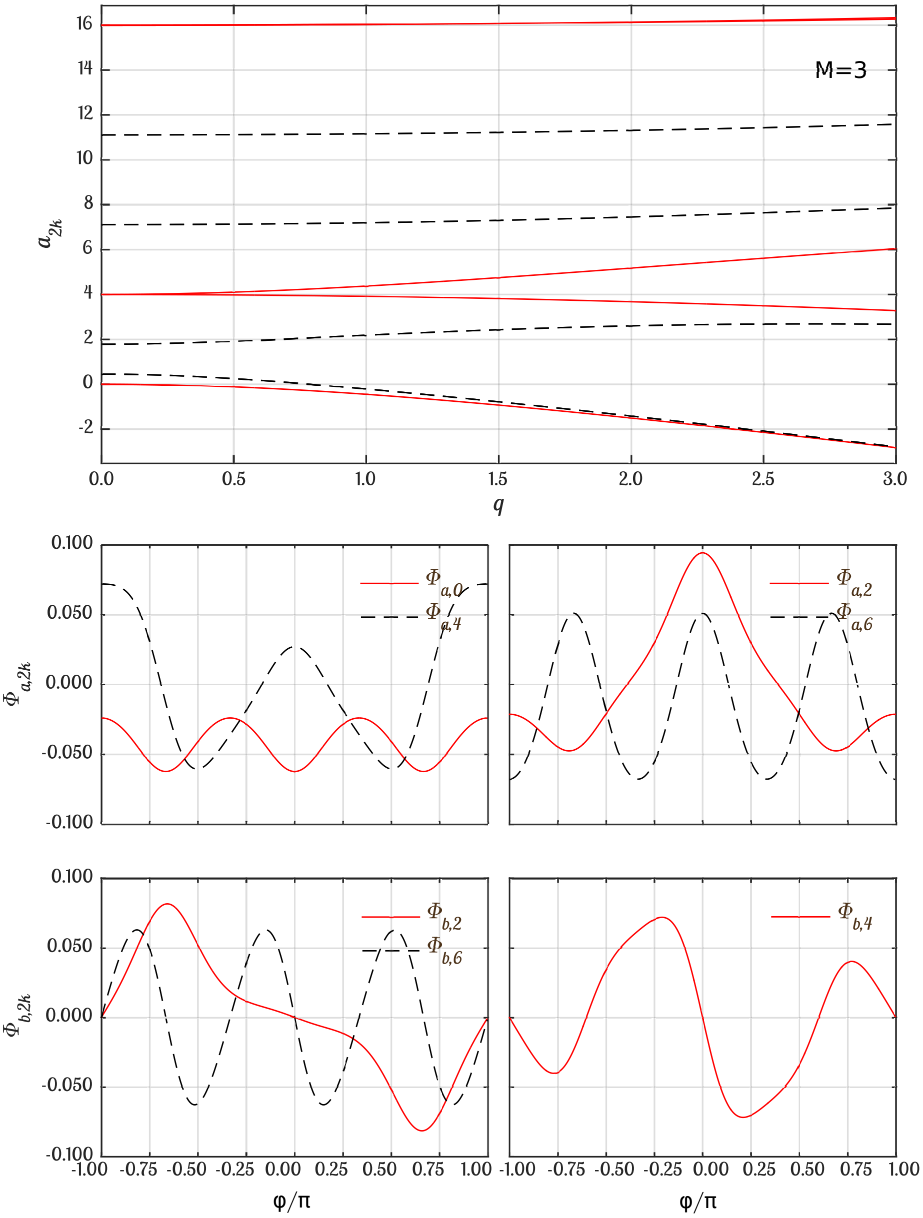

Figure 3.5: First row: a_j vs q for $M = 3$; second row: $\Phi_{a,2k}$ vs φ/π for $M = 3$, $q = 1$ and $0 \leq k \leq 3$; third row: $\Phi_{b,2k}$ vs φ/π for $M = 3$, $q = 1$ and $0 \leq k \leq 3$. The eigenstates with $k = 0, 3$ are non-degenerate the others are degenerate.

3.3 2D Quantum Rings.

Fig. 3.6 show a set of eigenstates for the 2D quantum ring (QR) described in Sec. 2.2.

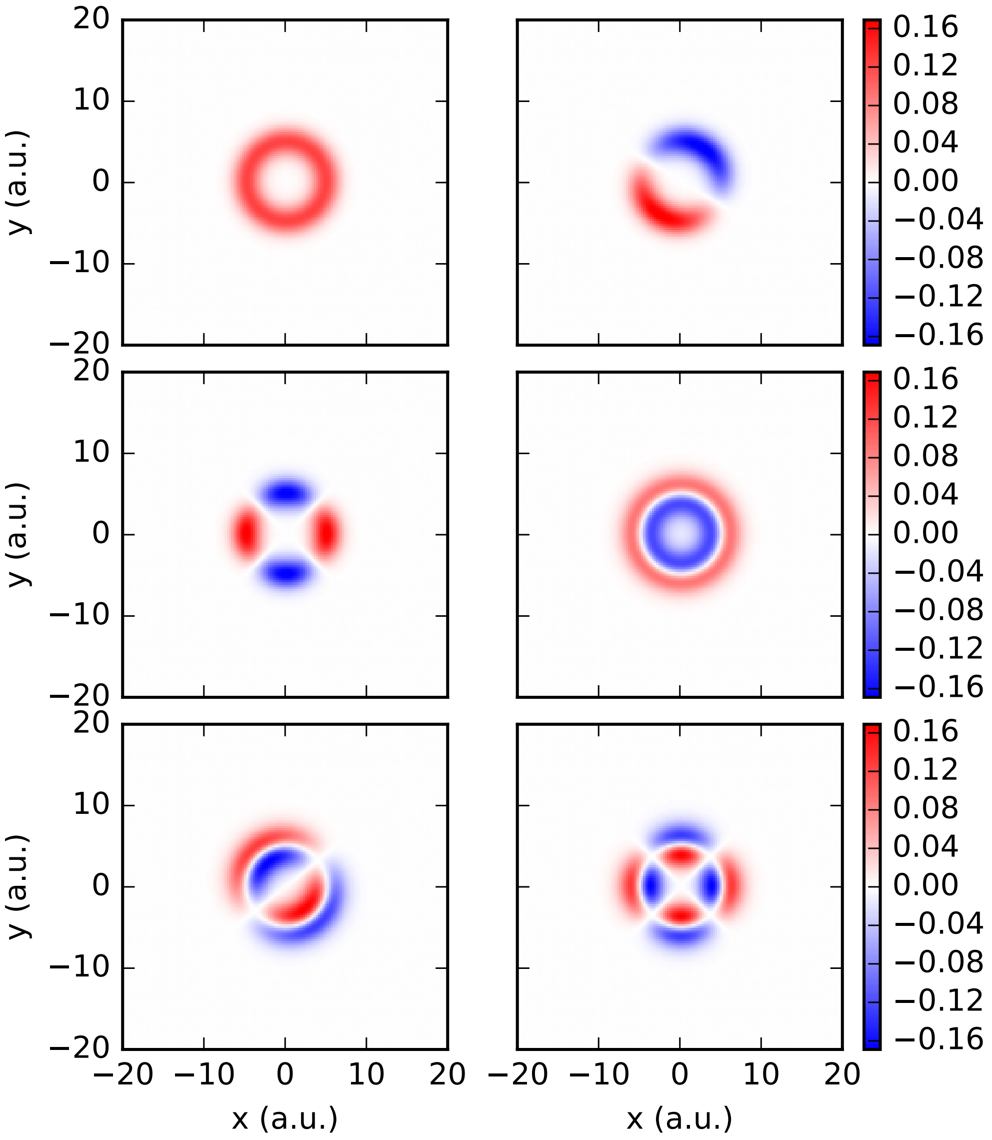

Figure 3.6: Set of eigenstates labeled $\{k, m\}$. From left to right: first row: $\{0, 0)$ and $\{0, 1\}$; second row: $\{0, 2\}$ and $\{1, 0\}$; third row: $\{1, 1\})$ and $\{1, 2\}$.

Orbital	E_j (au)	Occupation
HOMO-5	-1.206	2
HOMO-4	-0.905	2
HOMO-3	-0.638	2
HOMO-2	-0.600	4
HOMO-1	-0.576	2
HOMO	-0.428	4

Table 3.1: Energies (au) and occupations of the Kohn-Sham outer shell orbitals using in the numerical modelling of OCS.

3.4 DFT

3.4.1 OCS

In Tab. 3.1, we report the eigenvalues obtained by solving the Kohn-Sham equation with self-interacting correction (SIC) under LDA for carbonyl sulfide (OCS) molecules by considering an HEG. In addition, in Fig. 3.7 we plot HOMO-1 and HOMOs orbitals, which will be the most important for our further analysis. Afterwords, as we are in strong field regime, we will consider the core orbital as a pseudo-potential. A pseudo-potential is an opportune potential energy fitted which reproduces some experimental quantity. As we observe (in Fig. 3.7), OCS presents a degenerated HOMO with π-symmetry, and at the contrary HOMO-1 does not have nodal plane along $\hat{z}$, this has very important consequences when we make OCS interact with a laser, as we are going to see in the next.

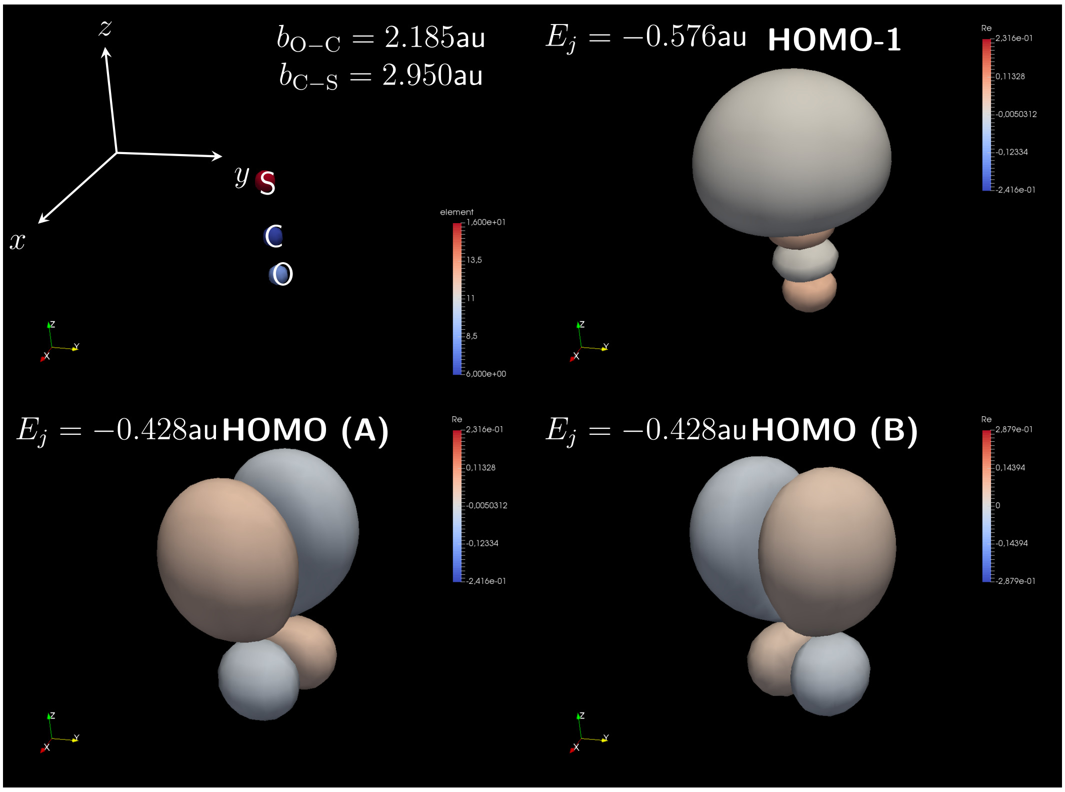

Figure 3.7: DFT study of OCS. In the first row left side we plot the OCS molecule (with in the upper right side the bound length used for the simulations and in the upper left side the axis of the reference system), and in order from left to right, up to down the Kohn-Sham HOMO-1 and HOMOs orbitals. For any orbital we report the corresponding evaluated energy in the upper part right side of the plot.

Orbital	E_j (au)	Occupation
HOMO-10	-1.363	2
HOMO-9	-1.255	4
HOMO-8	-0.823	2
HOMO-7	-0.767	2
HOMO-6	-0.709	4
HOMO-5	-0.658	2
HOMO-4	-0.583	4
HOMO-3	-0.545	4
HOMO-2	-0.520	2
HOMO-1	-0.463	2
HOMO	-0.375	4

Table 3.2: Energies (au) and occupations of the Kohn-Sham outer shell orbitals using in the numerical modelling of CF_3I.

3.4.2 CF_3I

As for OCS, in Tab. 3.2 we report the eigenvalues evaluated by solving the Kohn-Sham equation with SIC under LDA for a Trifluoromethyl iodide (CF_3I) molecule by considering a HEG and we plot, in Fig. 3.8, HOMO-1 and HOMOs orbitals. Also in this case we have a degenerate HOMO with π symmetry, and a HOMO-1 with no nodal plane around the molecular axis.

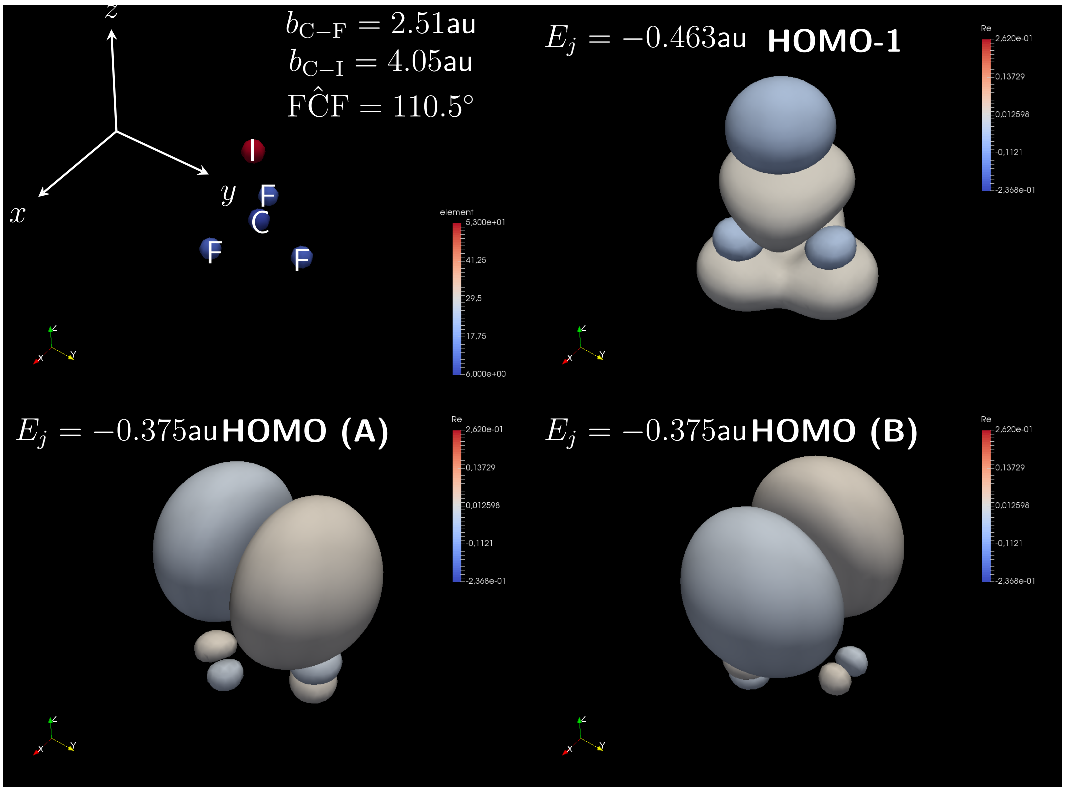

Figure 3.8: DFT study of CF_3I. In the first row left side we plot the CF_3I molecule (with in the upper right side the bound length used for the simulations), and in order from left to right, up to down the HOMO-1 and HOMOs Kohn-Sham orbitals. For any orbital we report the corresponding evaluated energy in the upper part right side of the plot.

Orbital	E_j (au)	Occupation
HOMO-1	-1.140	2
HOMO	-0.613	6

Table 3.3: Energies (au) and occupations of the Kohn-Sham outer shell orbitals using in the numerical modelling of Ar.

3.4.3 Ar

In Tab. 3.3 we report the energies and occupations of valence states of Argon evaluated by using LDA with SIC and by considering an HEG. In Fig. 3.9 we show the three fold degenerate groundstate, which has p-symmetry, being this symmetry similar to the π of OCS and CF_3I we are going to use Ar as sample system to improve the QRT model (see Sec. 1.5.2).

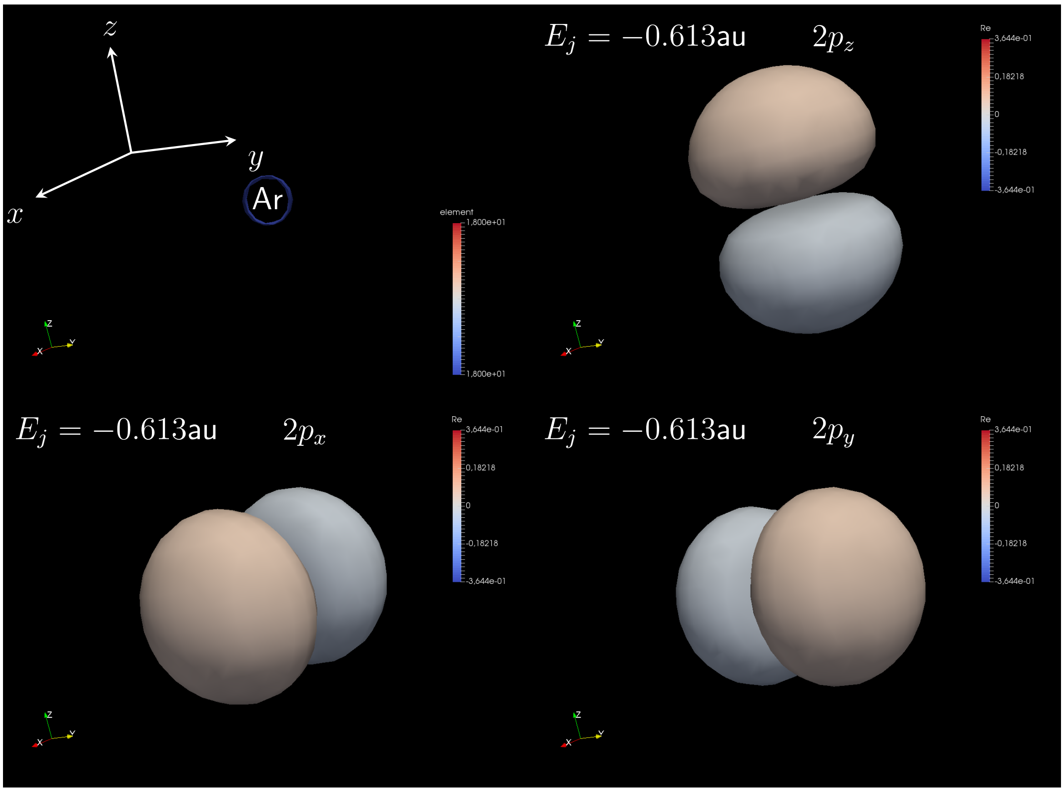

Figure 3.9: DFT study of Ar. In the first column we plot the Ar atom (with in the upper right side the bound length used for the simulations), and in order from left to right, up to down the Konh-Sham states. For any state we report the corresponding evaluated energy in the upper part right side of the plot.

$\mathcal{I}$ (W/cm^2)	v
10^{13}	0.9120
$4.7 \cdot 10^{13}$	1.9771
$4.72 \cdot 10^{13}$	1.9813
$4.74 \cdot 10^{13}$	1.9855
$5 \cdot 10^{13}$	2.0392
10^{14}	2.8839
$5 \cdot 10^{14}$	6.4486

Table 3.4: $\mathcal{I}$ in $\mathrm{W/cm^2}$ and corresponding values of v which will be used in the calculations.

3.5 Interaction between Matter and Strong Radiation.

Finally, we are ready to study the interaction between the systems that we have already introducted with a strong lasers. We are going to reconstruct important properties of the systems by studying the emission of light and electrons.

3.6 Classic rings.

Here, we study the Newton's Equation derived by the classical counterpart of the Hamiltonians respectevely of plain ring and SQR, see Sec. 2.5.1 (this study is also reported in [91]). In what follows we report only the most significant results of our calculations. Starting from the range of parameters derived by the information acquired in [62], we set $R = 10a_0$, with a_0 the Bohr radius, $\lambda = 1060$ nm corresponding to $\omega_L = 1.78 \cdot 10^{15}$ sec^{-1} ($\hbar\omega_L = 1.16$ eV) and $\gamma = 5 \cdot 10^{-3}\omega_L$. Actually, in the classic equations (see Eq.s 2.112) there is an important parameter the initial angular momentum ℓ_0, and by the nature of these equations it strongly affected the final results, for simplicity sake we always set $\ell_0 = 0$. In order to compare the value of the parameter v and the intensity generally using in the experiments it is useful to report

$$v = \frac{5.33 \cdot 10^{-9}\sqrt{\mathcal{I}(\mathrm{W} \cdot \mathrm{cm}^{-2})}}{R(\mathrm{au})} \left(\frac{\lambda_L(\mathrm{nm})}{45.57}\right)^2 \tag{3.1}$$

where λ_L is the wavelength of the laser in the indicated units. In Tab. (3.4) we report the intensity values used for this classic analysis and in addition the the wells of the SQR is set to $U_0 = 7.5 \cdot 10^{-2} e^2/a_0 = 2.04$ eV corresponding to $u = 2.4348$. In this section, we show several sets of Poincaré maps and the acceleration power spectrum obtained from the classical equations. In order to evaluate the Poincaré map, we study the trajectory points in the phase space, sampling every $\Delta\tau = 2\pi$ by varying the initial condition $\rho(0)$. This, kind of image are named Poincaré sections. Classically, by looking at Poincaré sections, we are able to discriminate between periodic and chaotic behaviour, depending on the presence of accumulation, randomly distributed and attractors points [78, 92].

3.6.1 Plain ring

It is not new to find chaotic motion of a charge on a plain ring [93]. Actually, we are interested in analyzing the effects of the structure of the ring on the chaotic motion, but in continuity to literature we start studying the plain ring $u = 0$. As said before (in Sec. 2.5.1), we set the numerical values of the parameters of the calculations close to the experimental ones used nowadays [94, 95]. However we used a laser field with pulse duration longer than the one used in the experiments, this is due to the fact that the chaoticity of this system can appear after some long transient. Thus, the pulses used in this part are so long that it is not necessary to consider their shape form. By looking at the classical equation of motion we easily see that all the minimum points of the potential, where the force is zero, are equivalent; thus when the laser field is linearly polarized in the direction perpendicular to the one indicated by ϕ_0 the electron remains at rest; of course the interaction is maximum when the previous two directions are parallel. In addition, we set $a = 5 \cdot 10^{-3}$, in order to see and to discuss some motion features.

The first analyzed case is the one with $v = 0.912$. By looking at this case, with several different initial positions (for our scope we did not show this data), we see a Poincaré section presenting three different attractors. For the symmetry of the system not only at $\phi_0 = 30°$, $\phi_0 = 90°$, $\phi_0 = 150°$, but also near the specular points $\phi_0 = 210°$, $\phi_0 = 270°$, $\phi_0 = 330°$ with different values of ℓ; consequently we have three different periods. But as said before, the system is really parameters sensitive thus we can also have only one attractor since a linear transition from the two types (one attractor $\rightarrow$ three attractors). In Fig. (3.10), we report the Poincaré map and the spectrum for three starting positions, very close each other, after a transition time, the Poincaré map starts to show some accumulation points, this it is strangely linked to an HHG spectrum that presents both odd order harmonics and side lines, actually the quantum origin of side lines has been discussed and they are referred to very different motivation to the one analyzed here [96, 97, 98], thus, they are unexpected in this context.

In Fig. (3.11) we show similar plots with a stronger field ($v = 2.0392$). The Poincaré sections reveal always two accumulation points reached after erratic exploration of the phase space; in this case the classic Fourier spectra present very sharp odd, even and half harmonics. Usually half harmonics are correlated with chaotic behaviour. In addition, we have notably increased the laser thus in the Hamiltonian there is a stronger laser-ring coupling; from an intuitive point of view, this coupling should have a large importance on the onset of chaos. It is also important to state that in the great amount of calculations not reported here, we found several case in which the electron does not reach in his time evolution a periodic attractor. For example, if we set $\phi_0 = 30°$ (this case is not reported in the thesis), leaving the other parameters unvaried, we find out that the Poincaré section is composed by a set of uncorrelated points in any position of the space, and the spectrum is obviously broad and dense.

It is interesting to study the case reported in Fig. (3.12), where we compare the results for two different v, and with the other parameters equal. In this comparison, we see that due to the fact that chaos is not predictable, the chaotic behaviour is evident for the v (first row); although the Poincaré maps do not seem to show important difference, the presence of an accumulation point, in the case shown in the bottom row, $(\phi, \ell) = (270°, -1)$ produce a spectrum presenting a comb of odd harmonics.

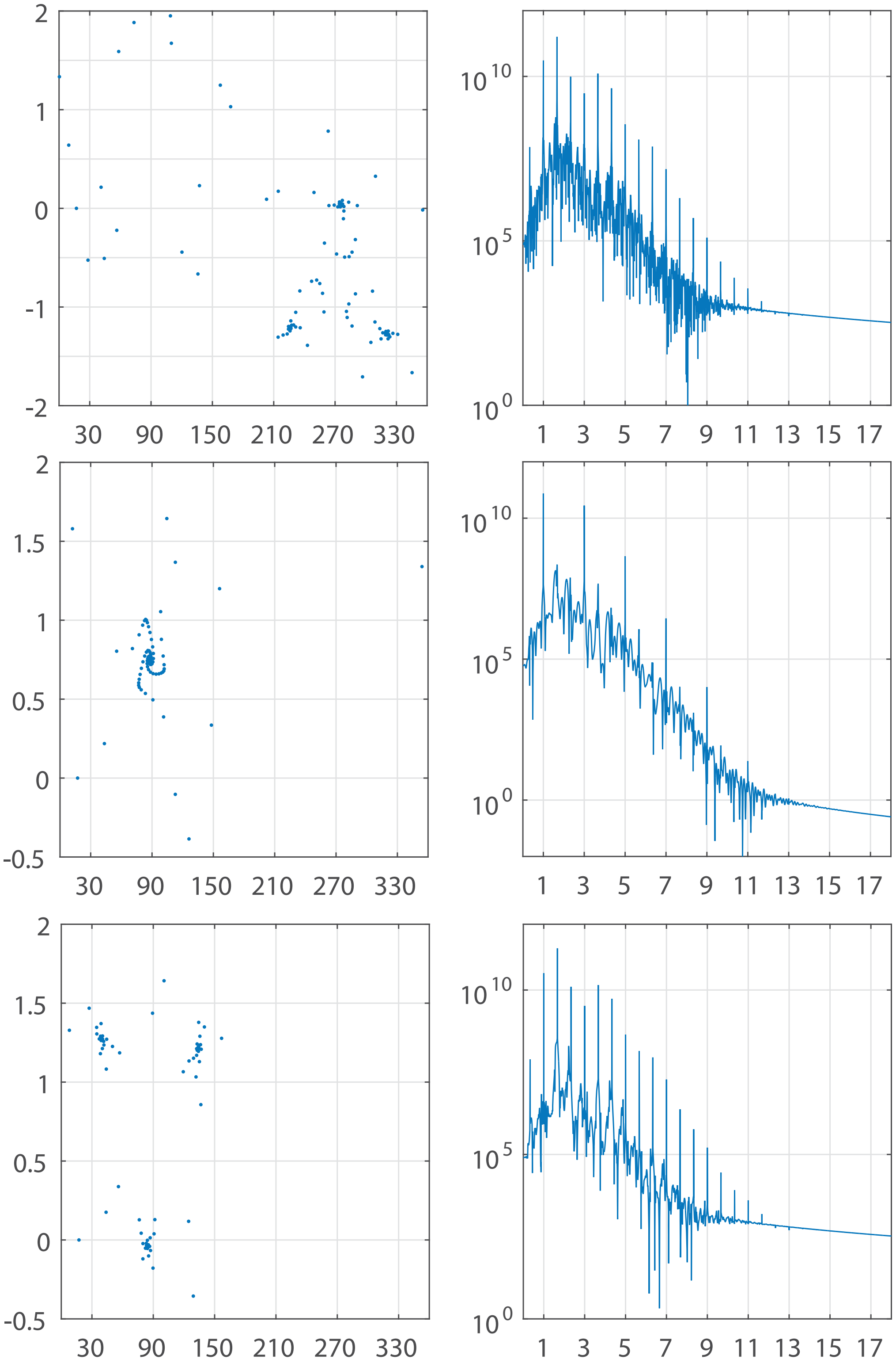

Figure 3.10: Left side: Poincaré section of the motion of the electron in a plain ring vs ϕ vs ℓ. Right side, Fourier power spectrum vs the harmonic order ω/ω_L. $u = 0$. With: top $\phi_0 = 17°$, center $\phi_0 = 17.2°$, bottom $\phi_0 = 17.3°$, 200 o. c., $a = 5 \cdot 10^{-3}$, $u = 0$ and $v = 0.912$.

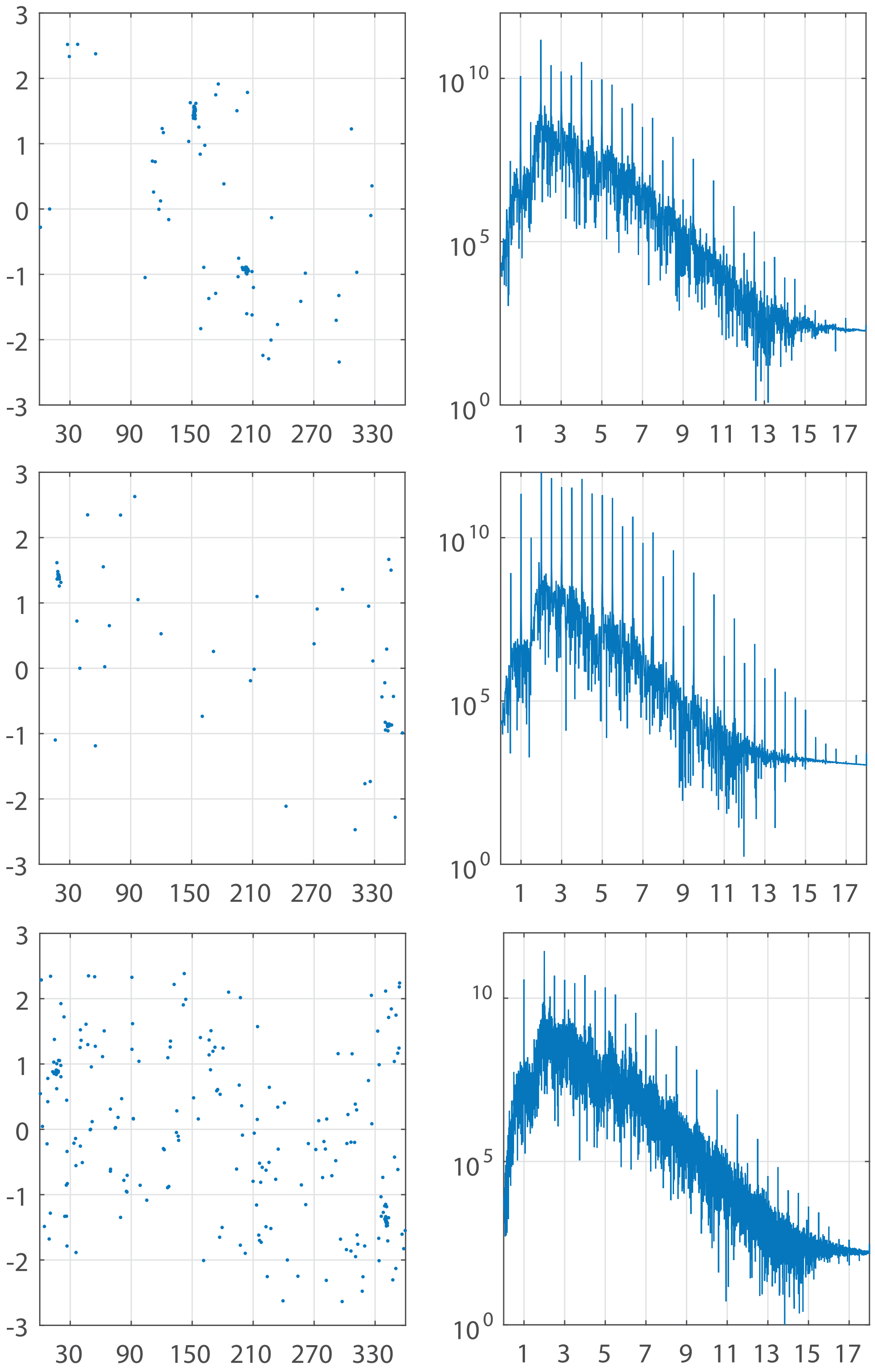

Figure 3.11: As Fig. 3.10, with in the top part $\phi_0 = 10^\circ$, 200 o.c.; center $\phi_0 = 40^\circ$, 800 o.c.; bottom $\phi_0 = 50^\circ$, 400 o.c.. The others values are $a = 5 \cdot 10^{-3}$, $u = 0$ and $v = 2.0392$.

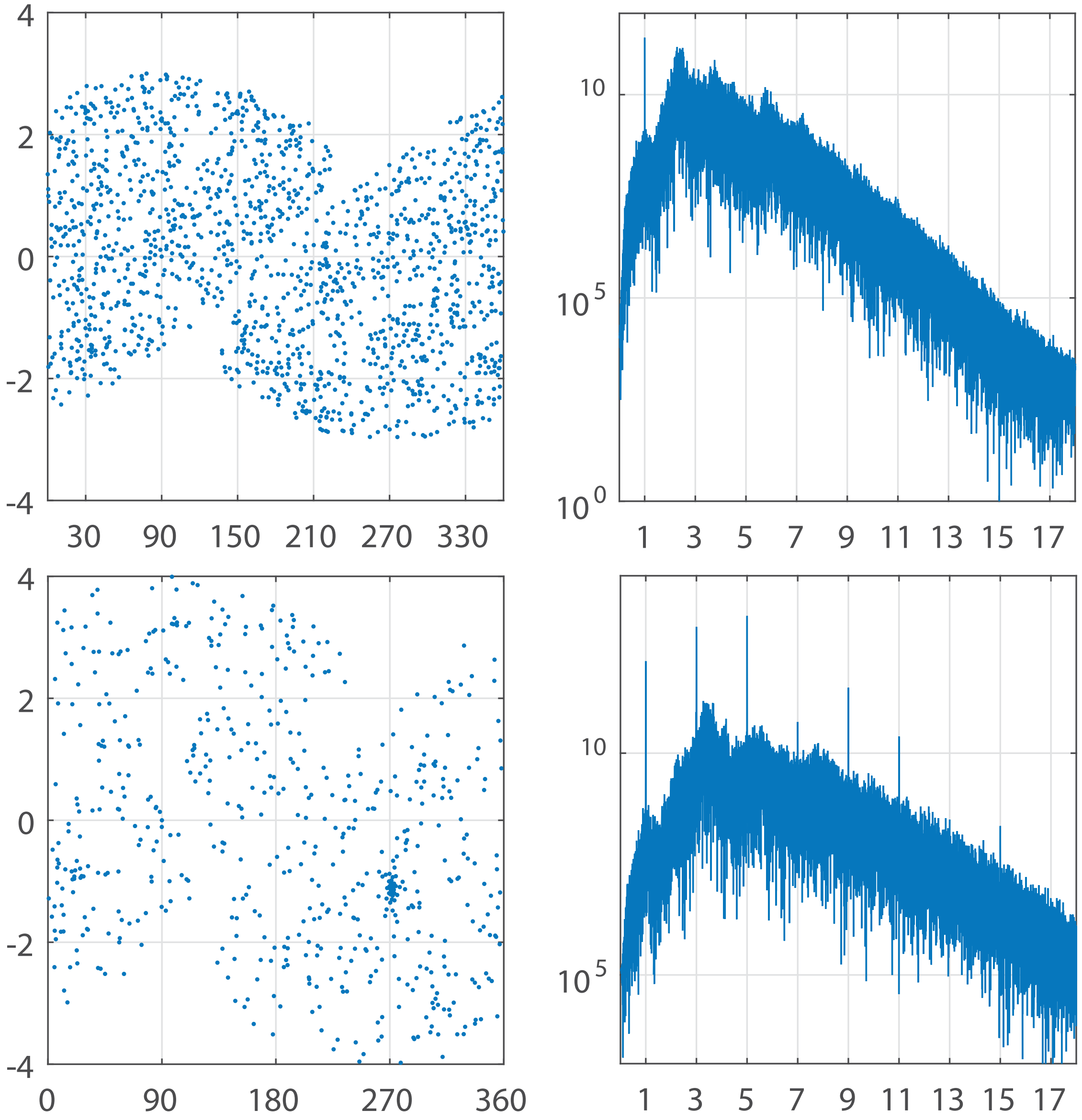

Figure 3.12: As Fig. 3.10 with $\phi_0 = 90°$, $a = 5 \cdot 10^{-3}$, 1500 o.c.. In the top part $v = 2.8839$ and in the bottom part $v = 6.4486$.

Finally, for the plain ring, we can state that the classical Newton Laws may show chaotic behaviour, that for the absence of regularity stimulates the ring to emit a broad and indistinct spectrum.

3.6.2 Structured ring

As a second case, we study the classic structured ring by setting $u \neq 0$.

In the absence of the laser, the system has six stable equilibrium points (at $\phi_n = -30° + n60°$ with $n = 1 \ldots 6$) and the same number of not unstable equilibrium points (at $\phi_n = n60°$). Although the system looks very different to the previous one, we still set $\ell_0 = 0$, this produces a pendular dumped motion around the closest stable position.

When the laser field is introduced, the system becomes extremely more complicated, in any case for weak external field the electron only oscillates between the closest unstable positions. But if the laser is intense enough, the particle starts to rotate in the ring and with small changes of the initial condition and parameters we get very different final state of motion.

As an instance, in Fig. 3.13 we report three cases, small variation of ϕ_0 (9°, 10°, 11°), and we get different final states of motion; the difference is not only the final attractor but also the way that they follow to reach it. It is interesting to pay attention to the middle plot, at beginning we observe a similar chaotic behaviour with a Poincaré section formed by point all over the space, but at end after a very long time $\tau > 250$ o.c. the electron remains in an attractor (located around $\phi = 150^\circ$). In the unreported calculations, we observe eventual revival of chaos, in any case the power spectra are similar and indistinct.

Depending on the polarization vector of the laser, a particle originally in a potential well have different motions. For example, if the laser is along $\hat{x}$, when the particle starts from $\phi_0 = 90^\circ$ the coupling laser-ring is maximum and the particle rotates along the ring, if $\phi_0 = 30^\circ$ the motion is periodic around this stable equilibrium position and thus the spectrum is well resolved. From a classic point of view, by varying ϕ_0 we set a different component of the tangential force applied to the electron in the ring.

As for the plain ring, we can state that the classical motion of an electron in a structured quantum ring driven by a strong laser field presents chaotic features. As we said before, in strong field physics it is used to predict the cutoff of the spectrum and other issue by evaluating the classical counterpart of the quantum system. When, as in this case, the system is chaotic this is not easy, roughly speaking, we may say that the electron in a cycle can absorb an energy of the order of $2V_0$, and by calculating numerically the maximum kinetic energy for the cases shown in this thesis we find from Eq. (2.113) that $K \leq 2.8$.

We have to clarify that we have studied the possibility of generating different final state by changing the value of the initial position. Thus, we have studied the chaoticity derived by ϕ_0, but in principle every variation in any parameters that we have in the equation could conduct from periodic to chaotic behaviour. Actually, we consider that there are not fluctuations in the laser intensity from a cycle to another and that the laser is constant for a very long duration, it is easy to realize that these possible variations shot by shot can totally change the results.

If we look at Fig. 3.14, we see that really little variation in the intensity generates a variety of results. The first row, show an incredible spectrum composed by odd harmonics, the Poincaré map shows that in this case the laser is still not intense enough to allow the rotation of the electron. The fact that the results, derived by solving the Newton Laws, are really affected by the parameters, allows us to say that this system is governed by parametric chaos[91].

3.7 QRs

At this point, we are ready to study quantum ring from the point of view of TDSE and thus in this section we are going to report quantum simulations (see [48]).

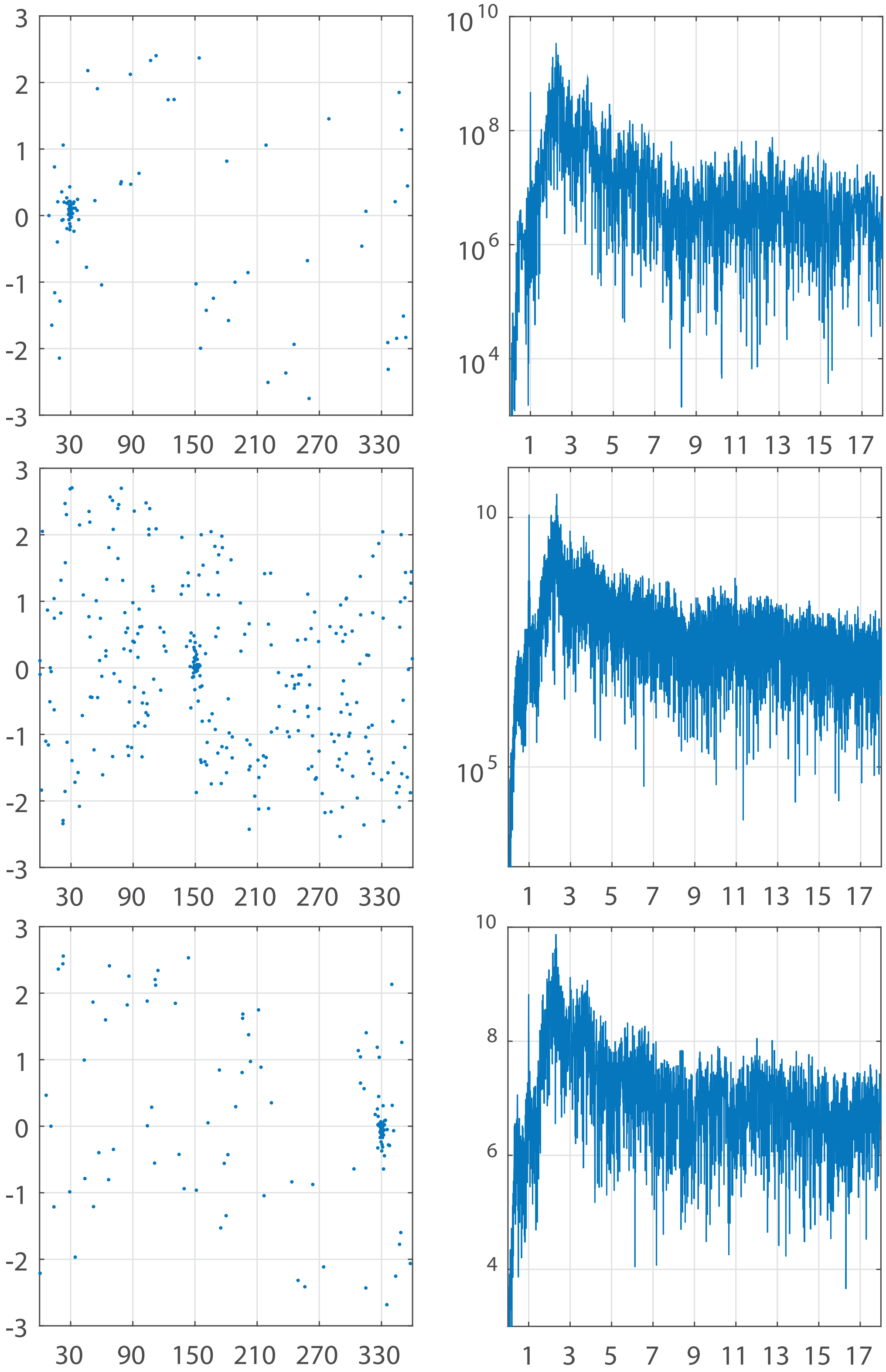

Figure 3.13: As Fig. 3.10. With 300 o.c., $a = 5 \cdot 10^{-3}$, $u = 2.4348$ and $v = 2.0392$: in the top part $\phi_0 = 9°$; in the center $\phi_0 = 10°$; in the bottom $\phi_0 = 11°$. The values of the load parameters are $a = 5 \cdot 10^{-3}$, $u = 2.4348$ and $v = 2.0392$.

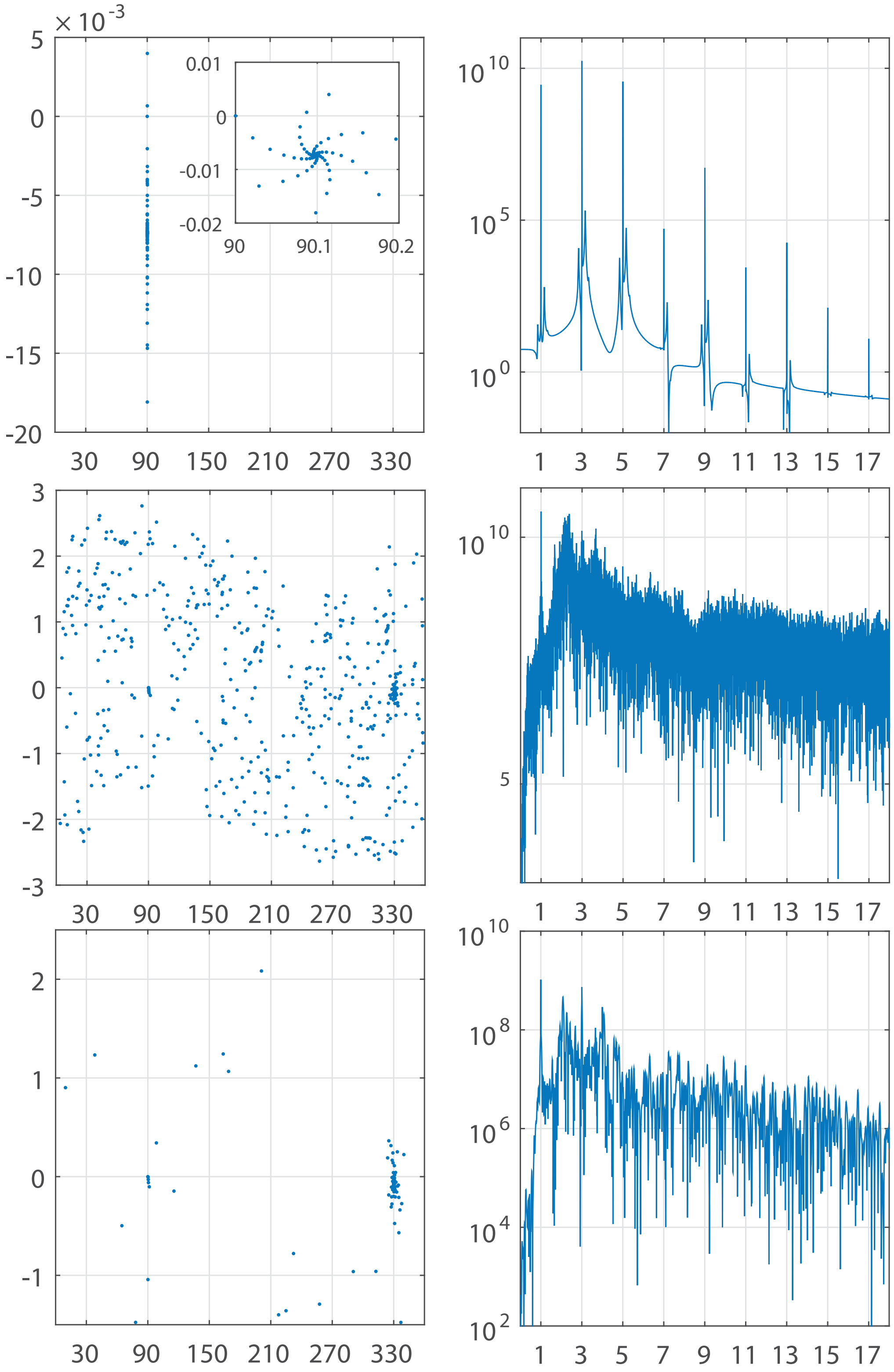

Figure 3.14: As Fig. 3.10, with $\phi_0 = 90°$, $a = 5 \cdot 10^{-3}$, $u = 2.4348$: in the top $v = 1.9771$, 300 o.c.; in the center $v = 1.9813$, 600 o.c.; in the bottom $v = 1.9855$, 600 o.c..

For simplicity sake, for any simulations in this part of the thesis we use a linearly polarized laser along the direction indicated by $\phi_L = 60^\circ$ (angle between polarization axis and x-axis). The latest section have clarified that the classical system is very sensible to the variations of the parameters of the equation. We want to observe if the quantum system is so parameters sensitive as the classic system and if we can use this to get control on the spectrum. In this section we are not interested in varying the laser parameters, thus we fix them: wavelength $\lambda = 780$ nm, intensity $I_0 = 4 \cdot 10^{14}\ \mathrm{W/cm^2}$ and trapezoidal shape of 32 optical cycles (o.c.), ramping up and down for 3 o.c..

The idea of the following study is to break the symmetry of the SQR and observe the variations that this produces on the emission properties. We want to make clear that when $\mathbb{V}_S$ (Eq. 2.5) and $\mathbb{V}_C$ (Eq. 2.6) share the same symmetry (called the symmetrical case), they present more or less the same eigenvalues with the same degeneracy chain (one non degenerate state, two twofold-degenerate states, one non degenerate state). This means that the solutions for the TISE using $\mathbb{V}_S$ are really close to the those for $\mathbb{V}_C$ reported in Sec. 2.1.2 and also showed in [62].

Initially, we study the symmetrical case as shown in Fig.(3.15), in the spectrum (first row), we indicate with dashed lines the energy difference between the excited states and the ground state, in addition we report in the bottom row the square modulus of the ground state, in order to clarify the symmetry of any observed case. To be thorough, in the bottom part of this figure it is easy to see that $V_S \cong V_0 \cos 6\phi$ up to an additive constant when $V_0 = 0.33$ au. This first spectrum contains both harmonic and non harmonic lines, the presence of close lines can be used to build short pulses.

Once we have explained the reference symmetrical case, we can explore the parameters of the ring to control some of the optical properties of the emitted radiation. Therefore we introduce modifications of V_S, and that means to solve the TDSE by varying η_1, K_1 and ϕ_1 (see Eq.2.5). The idea is to vary always one parameter, in Fig.s (3.16,3.17,3.18) we report the same quantities shown in Fig. (3.15) but with respectively $\frac{\eta_1}{\eta_0} = 0.97, 0.99$ and 1.03. As first sight, we see that the spectra present not only odd but also even harmonics, the appearance of which is a well known sign of reduced symmetry. The spectra are less dense than the one in Fig. (3.15), on the other hand, the plateau of the spectrum with $\frac{\eta_1}{\eta_0} = 0.99$ (Fig. (3.17)) is well resolved in harmonic lines.

The cutoff, is for any of the studied case, in agreement with that in Sec. 3.6.2 and [62, 91]. Although we do small variations of some parameters, by varying V_S, we actually change the observed system (see the plots of ground states in the bottom part of Fig.s (3.16,3.17,3.18)). The variation of the parameter η_1 are of the maximum order of 3 percent

Very small variations of the potential radically change the physical system, this is favorable to the goal of obtaining a tuning of the radiation properties, in addition the differences between the ground states can be used for better explaining some results. We note that (Fig. (3.18)) ($\eta_1 = 1.03\eta_0$) presents a ground state closer to the symmetrical system of (Fig.(3.15)) than the other cases; indeed we have significant variations in the ground state for $\eta_1 = 0.99\eta_0$ and a very different ground state for $\eta_1 = 0.97\eta_0$. Observing (Fig.s (3.16) and (3.17)) we note that both spectra present a rich plateau with only harmonic lines but the first one is less resolved. Moreover, have a look at the

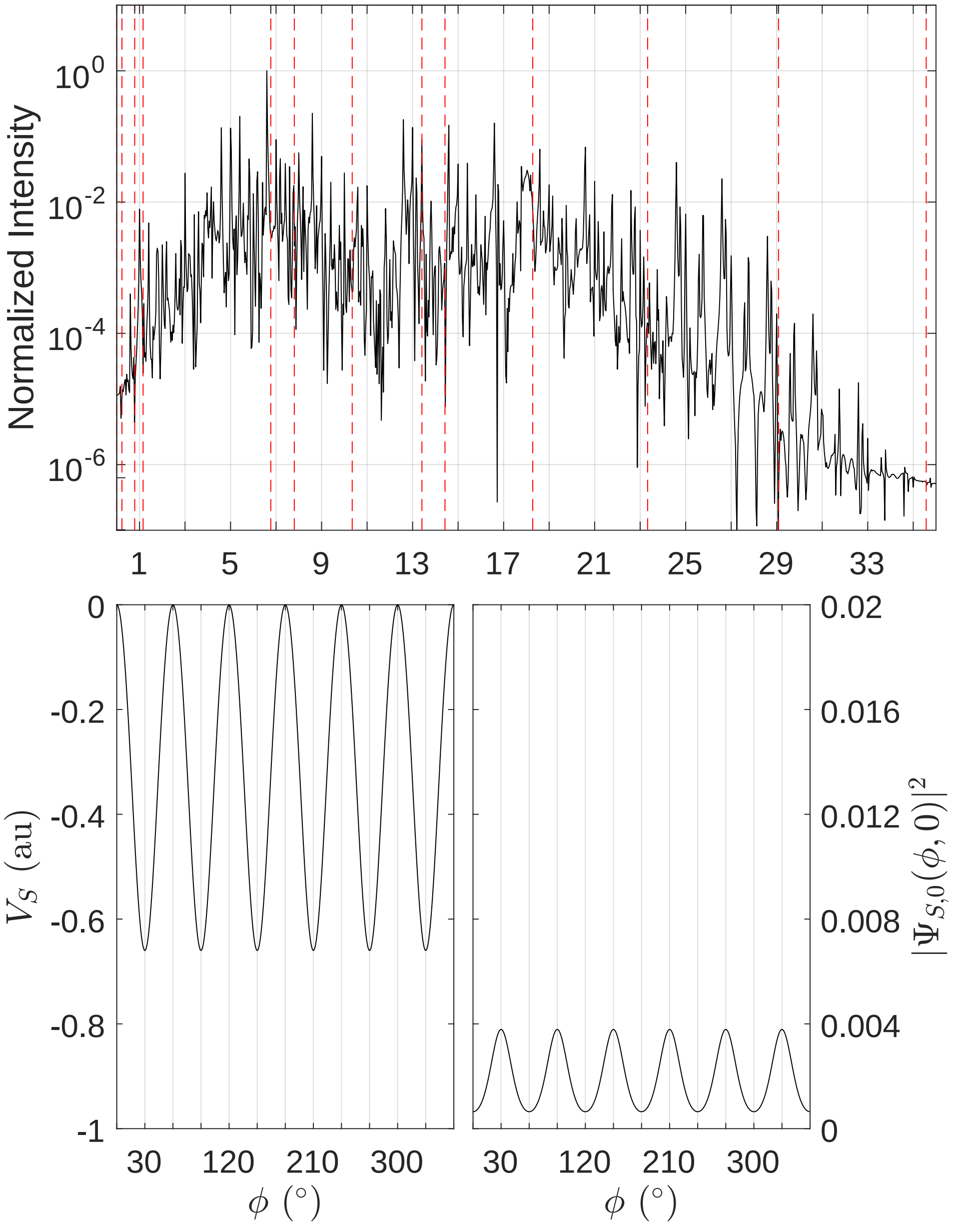

Figure 3.15: Top: Fourier spectrum with vertical dashed red lines indicating the energy differences between the ground-state and the excited states; bottom: in the left, V_S vs ϕ and in the right, square modulus of the ground state vs ϕ. With: $V_0 = 0.33$ au, $R = 5$ au, $\eta_1 = \eta_0 = 0.1333$, $K_1 = K_0 = 1.9420$ au, $\phi_i = 30°, 90°, 150°, 210°, 270°, 330°$, $\lambda = 780$ nm, $I_0 = 4 \cdot 10^{14} \mathrm{W/cm^2}$, trapezoidal shape($32$ o.c., 3 up, and 3 down) linearly polarized with $\phi_L = 60°$.

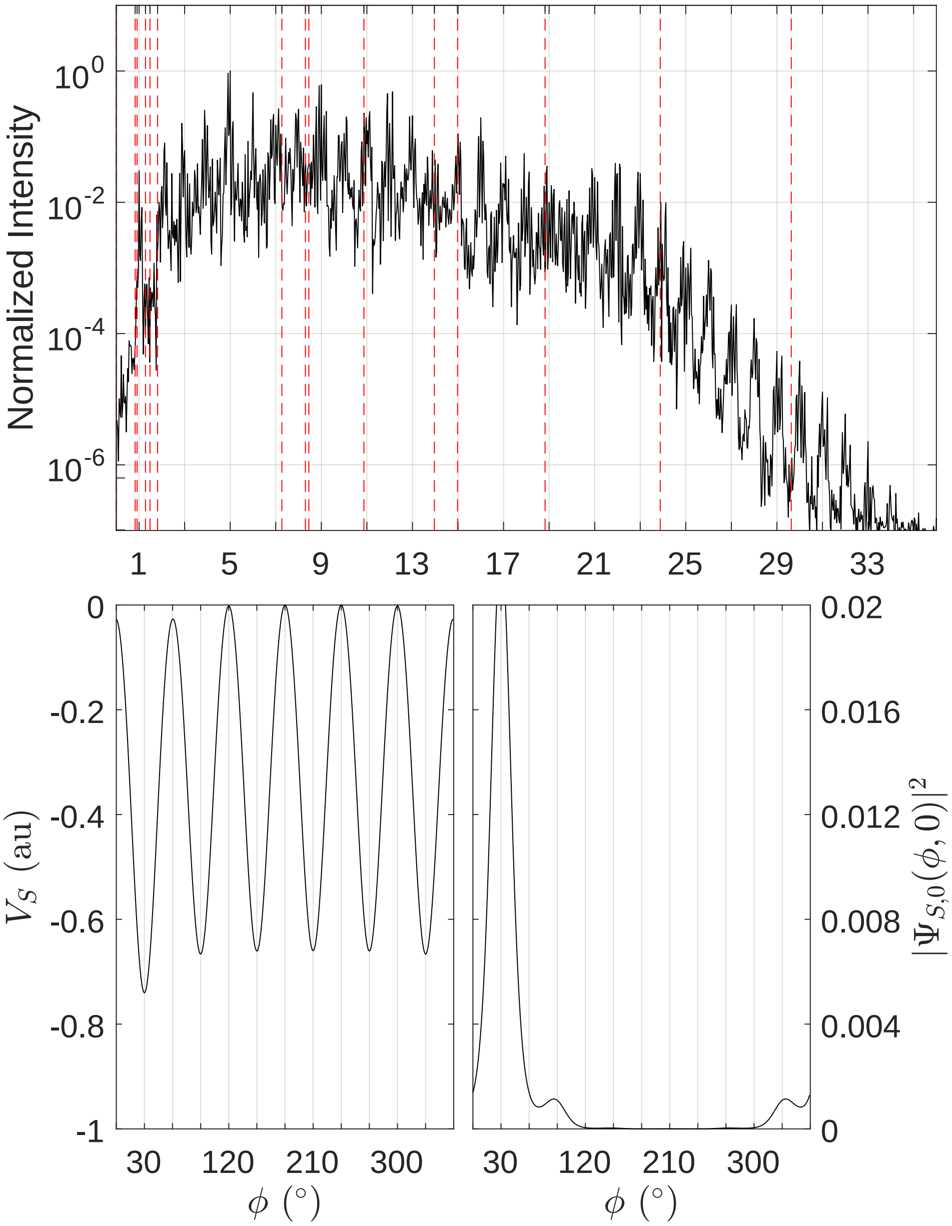

Figure 3.16: As Fig. (3.15) but with $\eta_1 = 0.97\eta_0 = 0.1293$.

ground states of Fig.s (3.16,3.17) we see that the population is mainly concentrated in the first dot, respectively we find in Fig. (3.17) $\frac{|\Psi_S(30^\circ,0)|^2}{|\Psi_S(90^\circ,0)|^2} \cong 3,5$ and in (Fig. (3.16)) $\frac{|\Psi_S(30^\circ,0)|^2}{|\Psi_S(90^\circ,0)|^2} \cong 22$, consequently the change of symmetry and in particular the unbalance of population are really important.

At this point, we analyze the results obtained by varying K_1, in particular in Fig.s (3.19, 3.20), we report respectively $\frac{K_1}{K_0} = 1.01, 1.02$, obviously, for comparison sake the other parameters are the same that the ones in Fig. (3.15). By focusing our

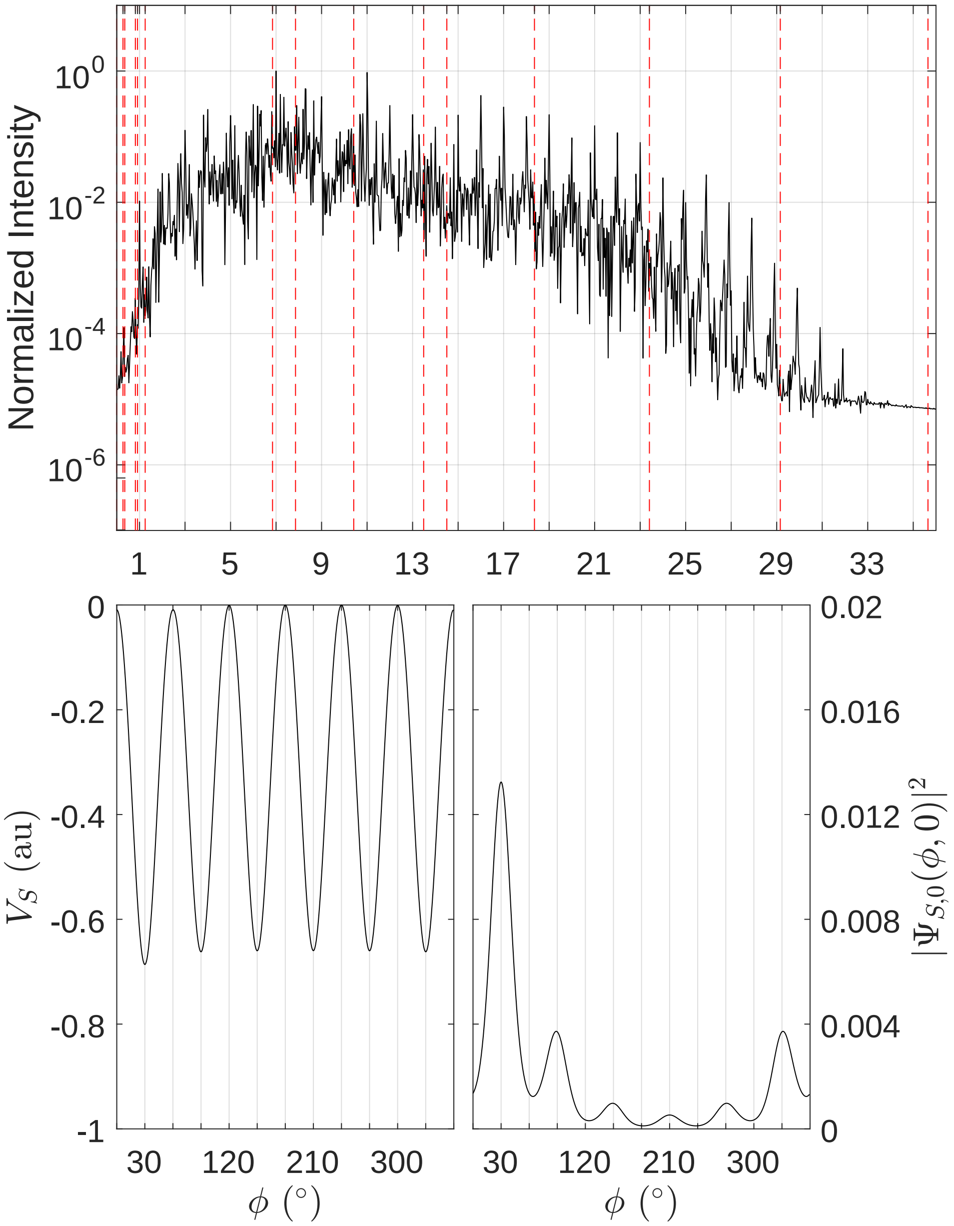

Figure 3.17: As Fig. (3.15) but with $\eta_1 = 0.99\eta_0 = 0.1320$.

analysis still on the ground state, we see that a small variation produces a spectrum more resolved in harmonics, but when the ground state is completely different, we get a spectrum unresolved.

The cases in Fig.s (3.19, 3.20) have the same symmetry, a specular one passing along $\phi_1 = 30°$. As next step, we want to break also this symmetry, thus we study the effects of varying ϕ_1 (Fig.s (3.21,3.22)). As interesting results of this case we find that for $\phi_1 = 32.5°$ Fig. (3.22), we get a larger cutoff. In any of the spectra we observe broad, resonant-like structures, for example in Fig. (3.15) at $7\omega_L$, $13\omega_L$, and $18\omega_L$, we guess that these are due to the Stark shift effect.

In order to make a consistent study, we plot in Fig. (3.23) the logarithm of the

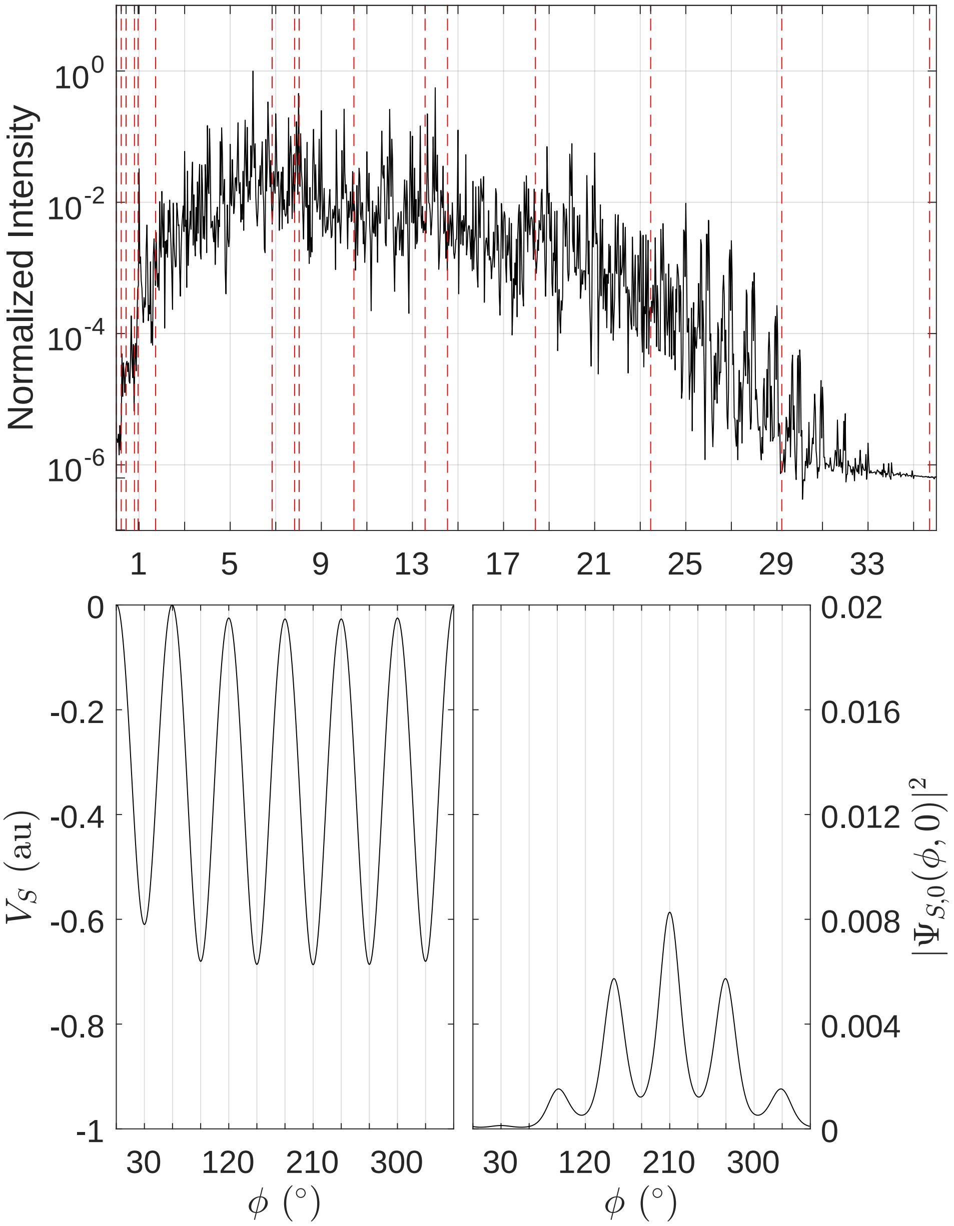

Figure 3.18: As Fig. (3.15) but with $\eta_1 = 1.03\eta_0 = 0.1373$.

spectra, by varying with continuity the previous three parameters. This analysis allows to observe clearly the variations of the cutoff and this is technologically important due to the fact that it has been found that the harmonics in the region of cutoff are important in the realizations of short pulses[99, 100]. Fig. (3.23) seems to not present a clear behaviour but by varying the parameters, we are able to increase the cutoff of 6 or 7 harmonics with respect the symmetrical case ($K_1 = 1.07K_0$, for $\eta_1 = 0.92\eta_0$ and for $\phi_1 = 32.5°$.)

The next phase of our analysis is based on the possibility to control the polarization of the emitted radiation. The main motivation of this is the fact that it is not easy to obtain circular short-wavelength sources in the 10–30 eV range close to the ionization energy of most atomic and molecular systems. Actually, there are several methods that allow to get

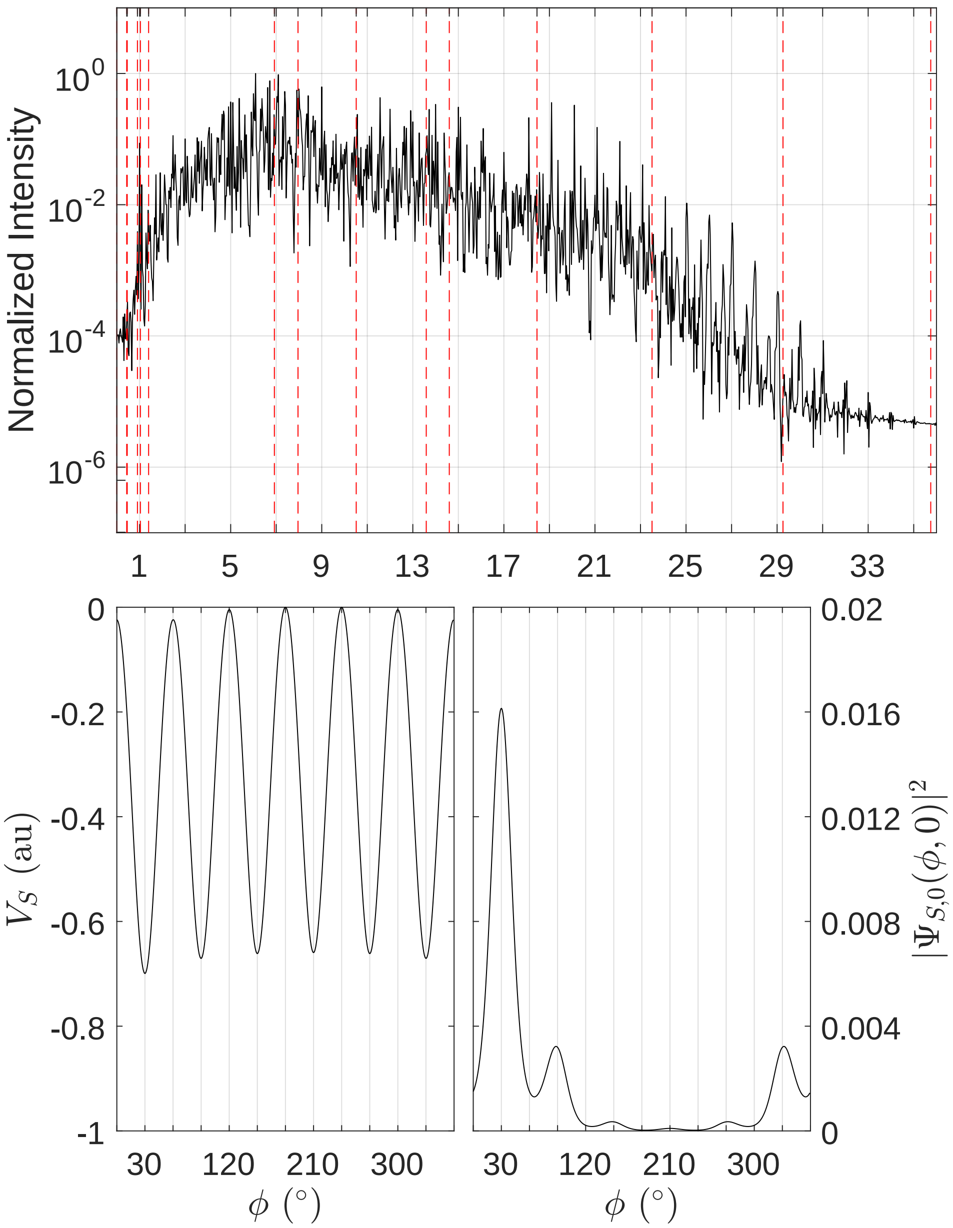

Figure 3.19: As Fig. (3.15) but with $K_1 = 1.01K_0 = 1.9614$ au.

circular polarized radiation, like, for example, the possibility to use multiple reflections on surfaces, but all these methods present a considerable reduction of the intensity, or do not allow to fine set the requested parameters [101]. One of the main problem to fix is the fact that, generally, the ellipticity of the harmonic radiation is lower than that of the driving laser. Actually, in the following we are going to show several times that it is possible to get elliptically polarized radiation with a linearly polarized probe laser field. The scope of realizing circular polarized laser with short-wavelength is that this radiation can be use to study the phenomenon of circular dichroism extended to the dynamical regime. The circular dichroism is the phenomenon of different absorption of some molecules of left and right handed light, and it depends on the spin angular momentum.

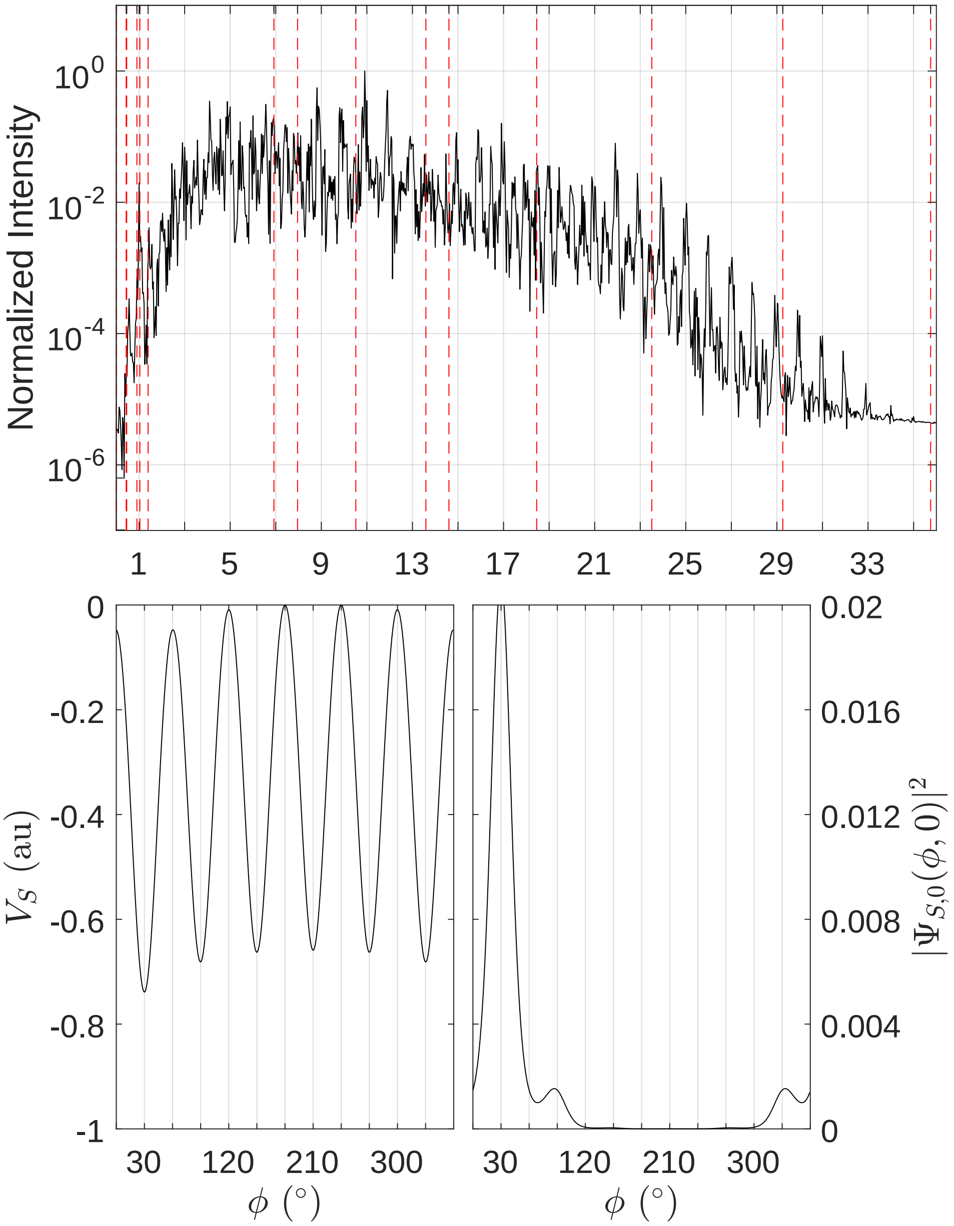

Figure 3.20: As Fig. (3.15) but with $K_1 = 1.02 K_0 = 1.9808$ au.

In Fig.s (3.24,3.25,3.26), we show the variations of the ellipticity and of the direction of the polarization of the emitted light by varying the three parameters (η_1, K_1 and ϕ_1). For the C_6 symmetrical system we observe that the emitted radiation has the same polarization of the driving laser, at the contrary for the other cases, we get different polarization, comparing Fig.s 3.18 and 3.24, we observe that for small variations of the ground state, small variations of the polarization, and for bigger variations very different ψ and χ.

For having information about the emission of an harmonic at time t we study the Morlet spectrum (Fig.s (3.27) and (3.28)) respectively for $\eta_1 = 0.97\eta_0$ and $\eta_1 = 0.99\eta_0$- As interesting feature, we see that in both cases, H20-H29 are emitted simultaneously in

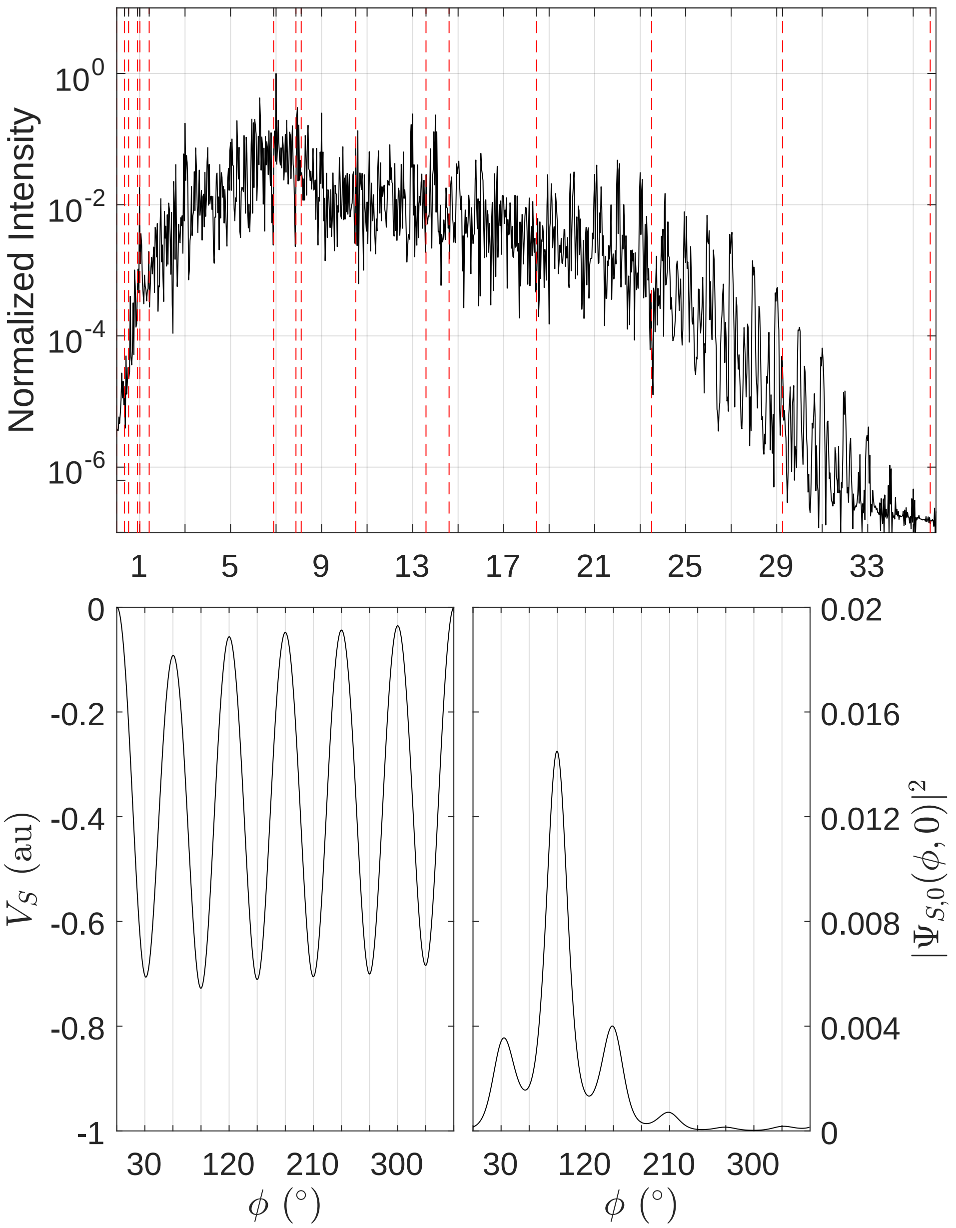

Figure 3.21: As Fig. (3.15) but with $\phi_i = 30.75°, 90°, 150°, 210°, 270°, 330°$.

different time intervals located after the 20-th o.c.. In order to correlated the emission of these higher harmonics and the total emitted power, we plot the averaged power $P(\mathcal{T})$ (where we use $\mathcal{T}_n = [\frac{n-1}{2}T_L, \frac{n}{2}T_L]$ with $n = 1, \ldots, 64$). As result, we see that in the time interval $[20.5, 21]$ o.c. at a maximum of $P(\mathcal{T})$ corresponds the emission of harmonics from 21-th to 27-th. We consequently get very intense simultaneous emission of the higher harmonics.

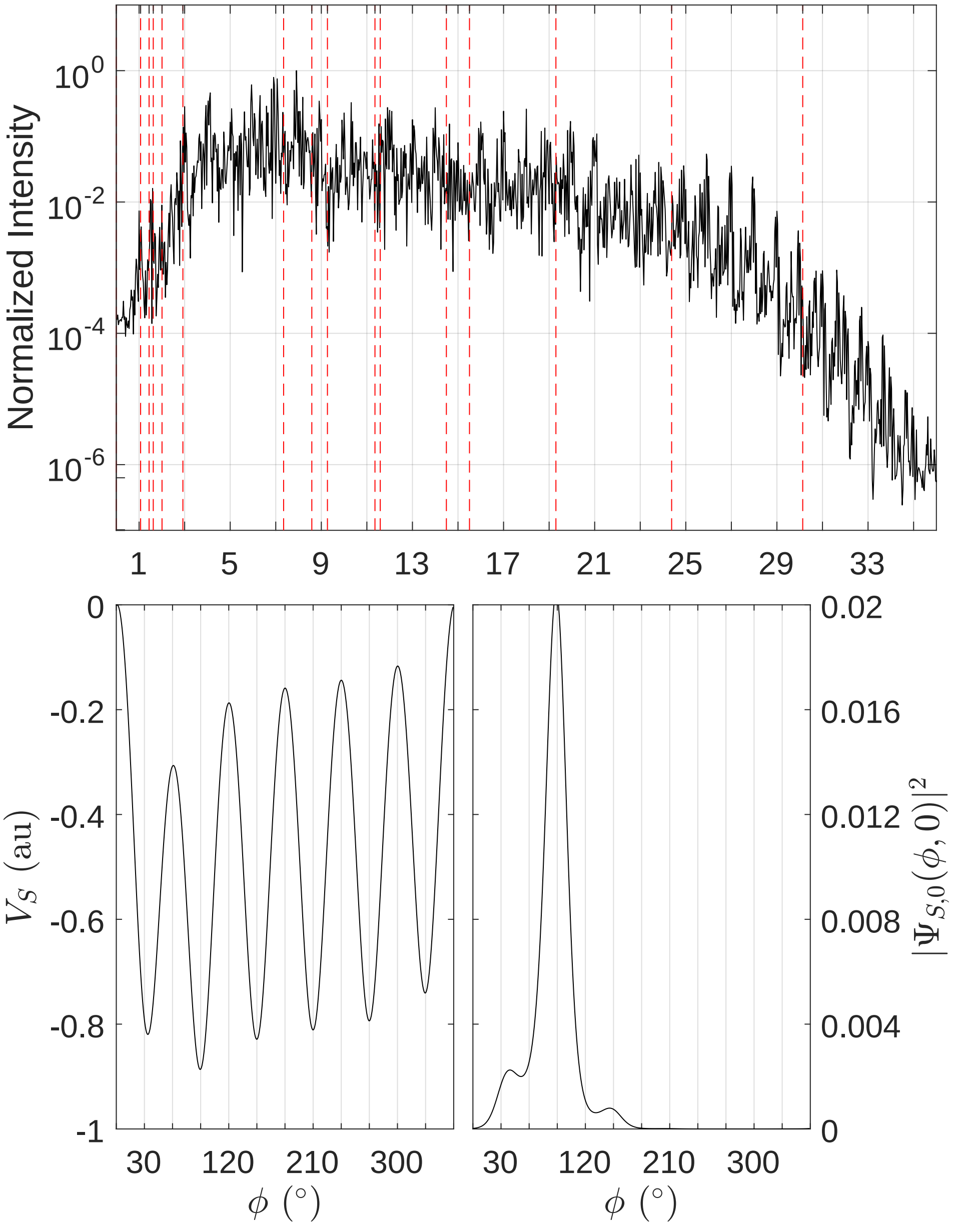

Figure 3.22: As Fig. (3.15) but with $\phi_i = 32.5°, 90°, 150°, 210°, 270°, 330°$.

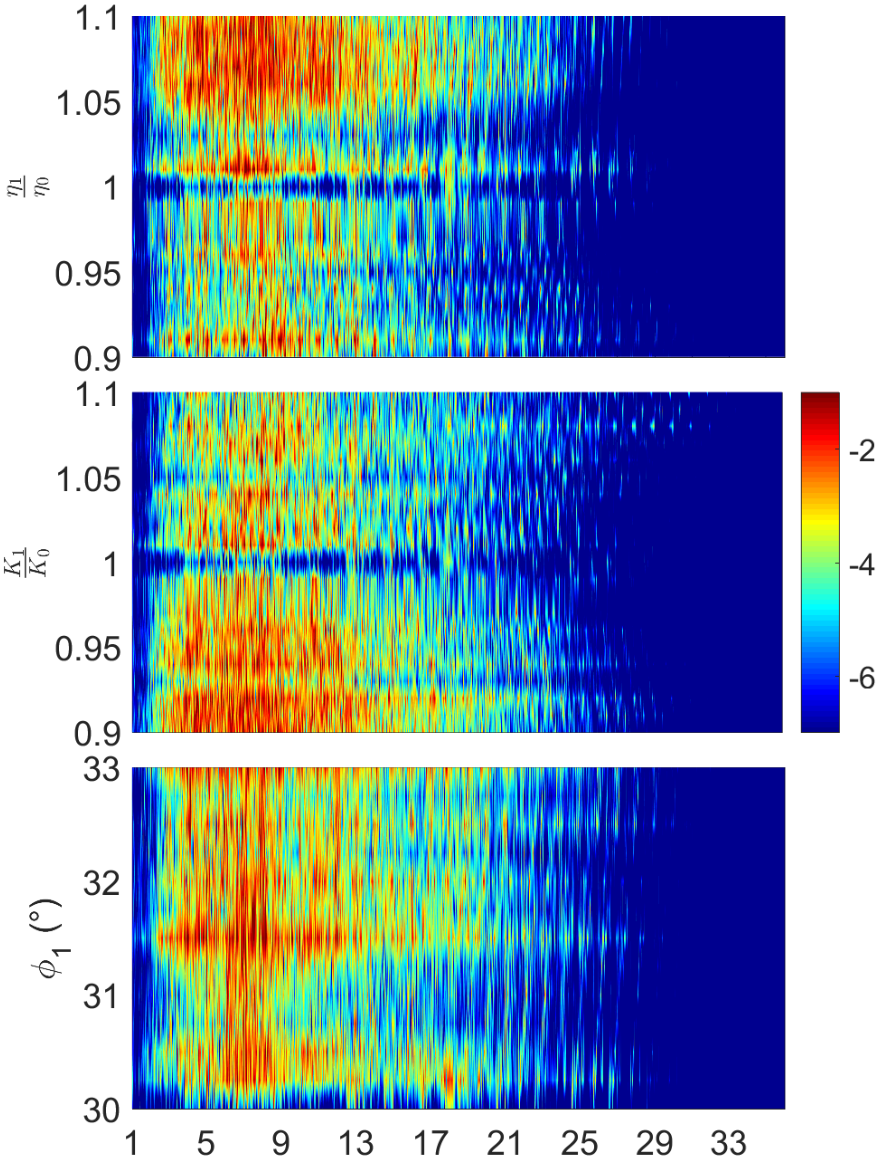

Figure 3.23: Top: logarithm of Fourier spectrum vs harmonic order vs η_1 with $K_1 = K_0 = 1.9420$ au and $\phi_i = 30°, 90°, 150°, 210°, 270°, 330°$; middle: Fourier spectrum vs harmonic order vs K_1 with $\eta_1 = \eta_0 = 0.1333$ and $\phi_i = 30°, 90°, 150°, 210°, 270°, 330°$; bottom: Fourier spectrum vs harmonic order vs ϕ_1 with $K_1 = K_0 = 1.9420$, $\eta_1 = \eta_0 = 0.1333$ and $\phi_{2,\dots,6} = 90°, 150°, 210°, 270°, 330°$. The others parameters are: $V_0 = 0.33$ au, $R = 5$ au, $\lambda = 780$ nm, $I_0 = 4 \cdot 10^{14} \mathrm{W/cm^2}$; trapezoidal shape ($32$ o.c. of duration with 3 o.c. of up and down ramping) and is linearly polarized with $\phi_L = 60°$.

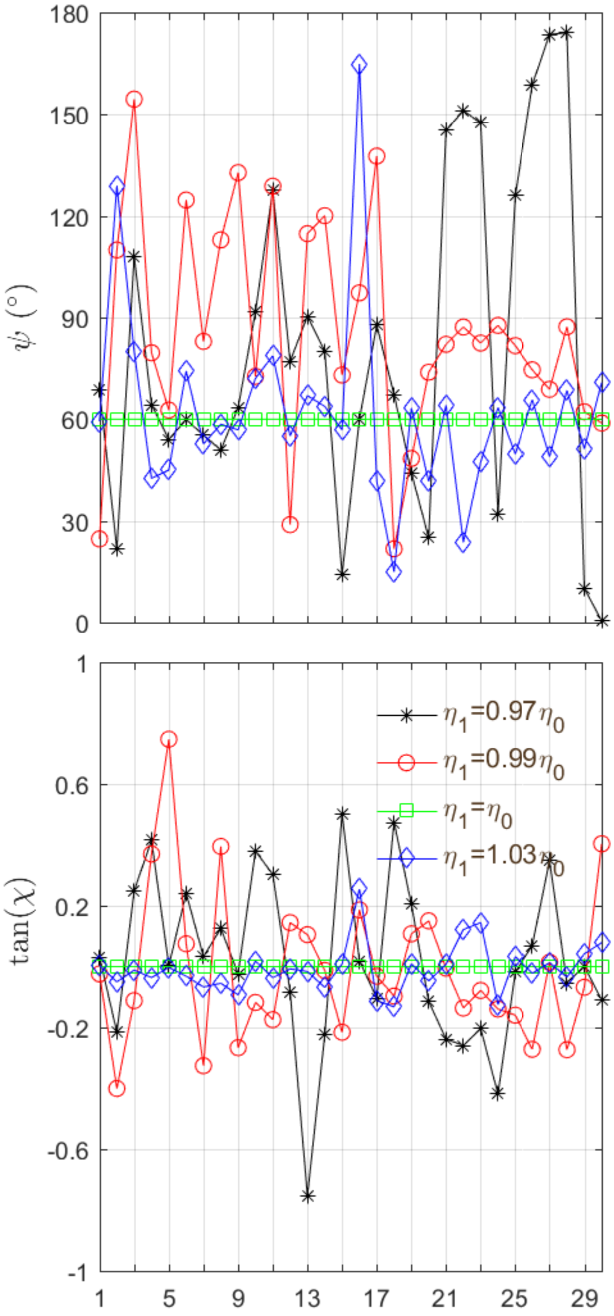

Figure 3.24: Top: ψ vs harmonic order (as function of η_1); bottom: $\tan\chi$ vs harmonic order (as function of η_1). With: $V_0 = 0.33$ au, $R = 5$ au, $K_1 = K_0 = 1.9420$ au, $\phi_i = 30°, 90°, 150°, 210°, 270°, 330°$, $\lambda = 780$ nm, $I_0 = 4 \cdot 10^{14}\mathrm{W/cm}^2$, trapezoidal shape(32 o.c., 3 up, and 3 down) linearly polarized with $\phi_L = 60°$.

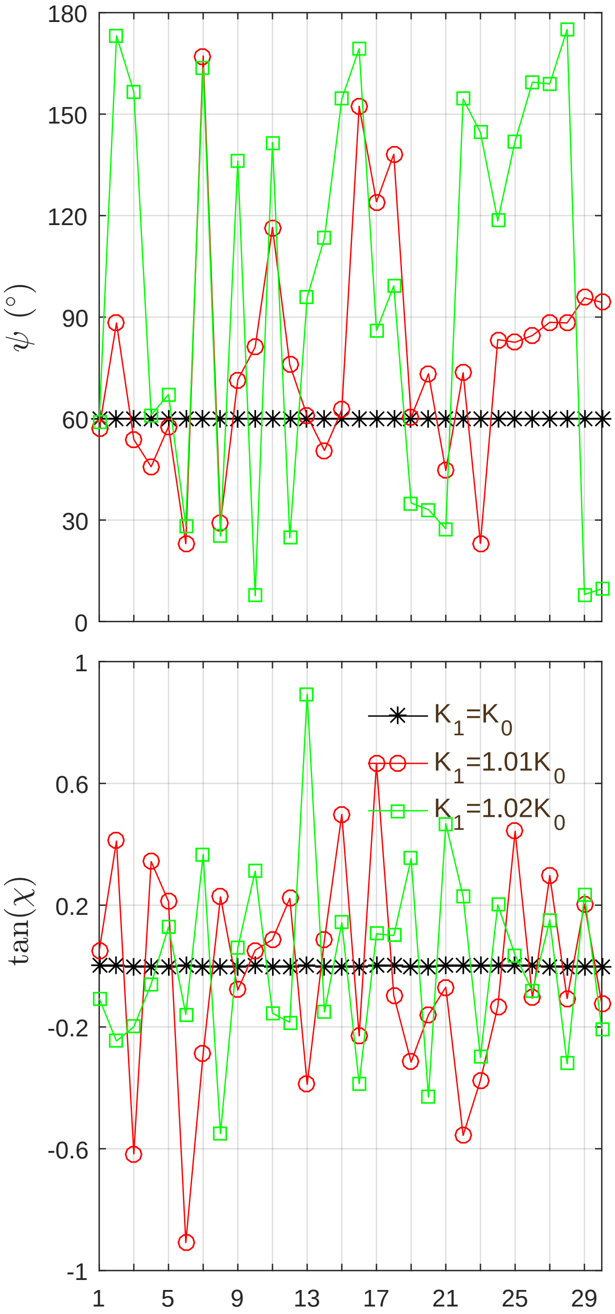

Figure 3.25: Top: ψ vs harmonic order (as function of K_1); bottom: $\tan\chi$ vs harmonic order (as function of K_1). With: $V_0 = 0.33$ au, $R = 5$ au, $\eta_1 = \eta_0 = 1333$, $\phi_i = 30°, 90°, 150°, 210°, 270°, 330°$, $\lambda = 780$ nm, $I_0 = 4 \cdot 10^{14}\mathrm{W/cm^2}$, trapezoidal shape($32$ o.c., 3 up, and 3 down) linearly polarized with $\phi_L = 60°$.

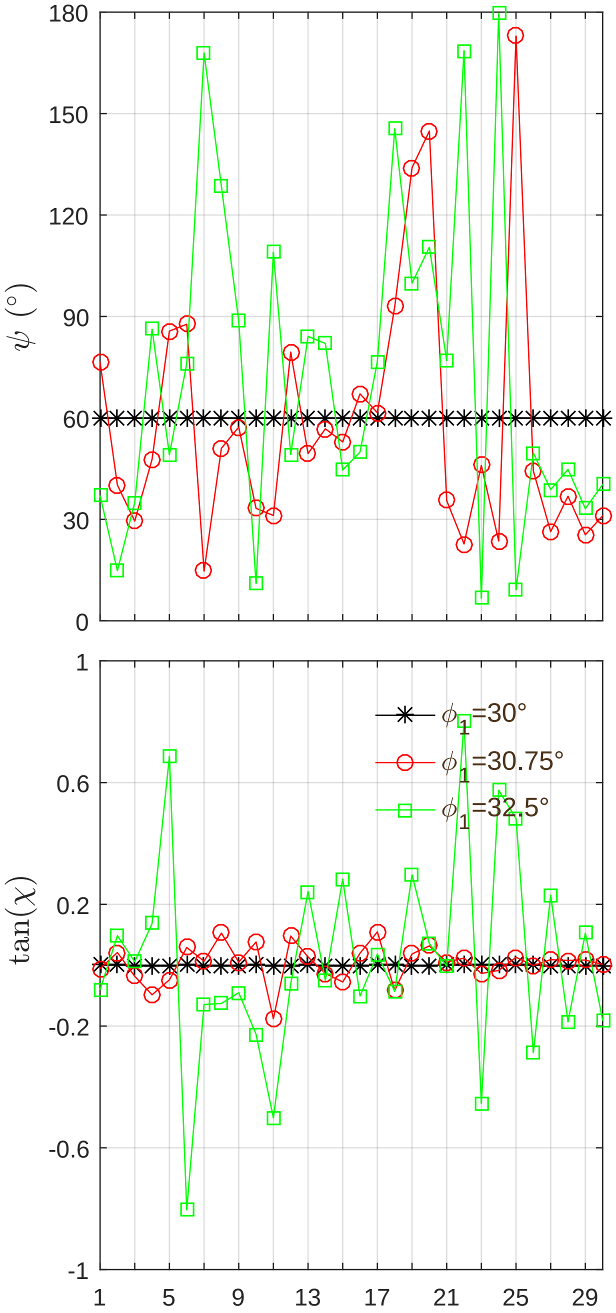

Figure 3.26: Top: ψ vs harmonic order (as function of ϕ_1); bottom: $\tan\chi$ vs harmonic order (as function of ϕ_1). With: $V_0 = 0.33$ au, $R = 5$ au, $\eta_1 = \eta_0 = 1333$, $K_1 = K_0 = 1.9420$ au, $\lambda = 780$ nm, $I_0 = 4 \cdot 10^{14}\mathrm{W/cm^2}$, trapezoidal shape($32$ o.c., 3 up, and 3 down) linearly polarized with $\phi_L = 60°$.

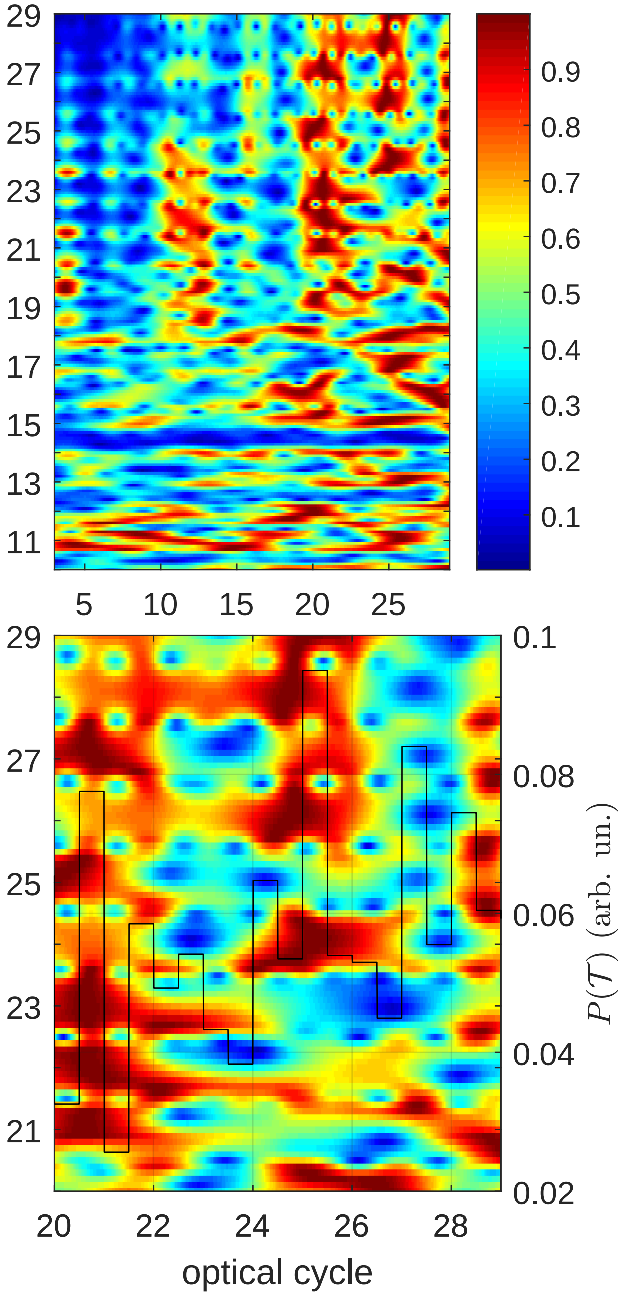

Figure 3.27: Top: Morlet spectrum vs t; bottom: zoom of the Morlet spectrum and, as black histogram, $P(\mathcal{T})$ vs t. With: $V_0 = 0.33$ au, $R = 5$ au, $\eta_1 = 0.97\eta_0 = 0.1293$, $K_1 = K_0 = 1.9420$ au, $\phi_i = 30°, 90°, 150°, 210°, 270°, 330°$, $\lambda = 780$ nm, $I_0 = 4 \cdot 10^{14}\mathrm{W/cm^2}$, trapezoidal shape($32$ o.c., 3 up, and 3 down)linearly polarized with $\phi_L = 60°$.

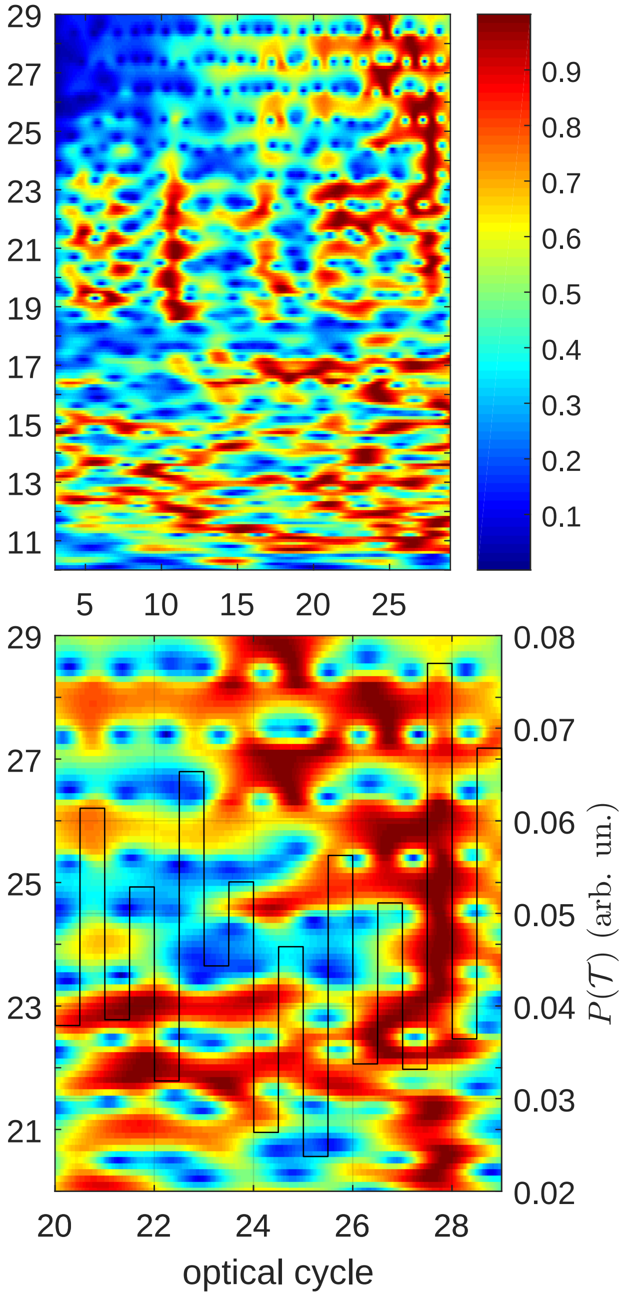

Figure 3.28: As (Fig.3.27) but with $\eta_1 = 0.99\eta_0 = 0.1320$.

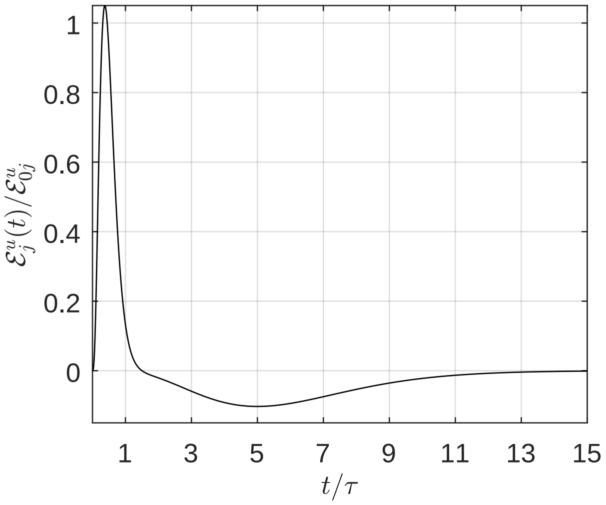

Figure 3.29: Example of unipolar pulse $\mathcal{E}_x^u(t)/\mathcal{E}_{0x}^u$ vs t/τ; with on switching at $t = 0$.

3.8 2D QRs.

Until now, we studied QRs from 1D point of view, thus we suppressed every possibility of radial motion and consequently ionization. In this section we focus on the possibility to have a system in which the electrons can go to the continuum as required by the three step model.

The guiding principle of this study is still the one underlined in Sec. 3.7. In order to get the goal of controlling the emission, instead of inserting different wells on the ring, we use another approach, always by using the idea of breaking symmetry, we play with the incident pulse acting on a plain rings. We underline that, also in this case, we are looking for the possibility to produce circular polarized radiation using linearly polarized probe laser field, for the motivation reported in Sec. 3.7 Thus, we add to the linear polarized laser, an unipolar pulse polarized along x or y according to the needs. An unipolar pulse present an intense first peak followed by a broad less intense one with opposite polarity. The peculiar properties of the unipolar pulse have interesting consequences on the emission, thus recently they are studied in a great amount of literature [102, 103, 104, 105, 106, 107].

We describe the electric field of the unipolar pulse with the expression

$$\mathcal{E}_j^u(t) = \mathcal{E}_{0j}^u \Theta(t - t_j) \left(\frac{\alpha}{\tau^3}(t - t_j)^3 e^{-8(t-t_j)/\tau} - \frac{\beta}{\tau^5}(t - t_j)^5 e^{-(t-t_j)/\tau} \right) \tag{3.2}$$

with $j = (x, y)$. In order to have a realistic pulse we must to impose that

$$\int_0^\infty \mathcal{E}_j^u(t)dt = 0; \tag{3.3}$$

and thus $\beta = \alpha/81920$, at the same time $\alpha = 400$ is chosen so that $\max\left(\mathcal{E}_j^u(t)\right) = \mathcal{E}_j^u(3\tau/8)) \cong 1.05\mathcal{E}_{0j}^u$, in Fig. 3.29 we show the described unipolar pulse.

If we drive a 2D QR with a unipolar pulse along x (Fig. 3.30), the spectrum presents two lines corresponding to the angular transitions $\{0, 0\} \leftrightarrows \{0, 1\}$ and $\{0, 1\} \leftrightarrows \{0, 2\}$,

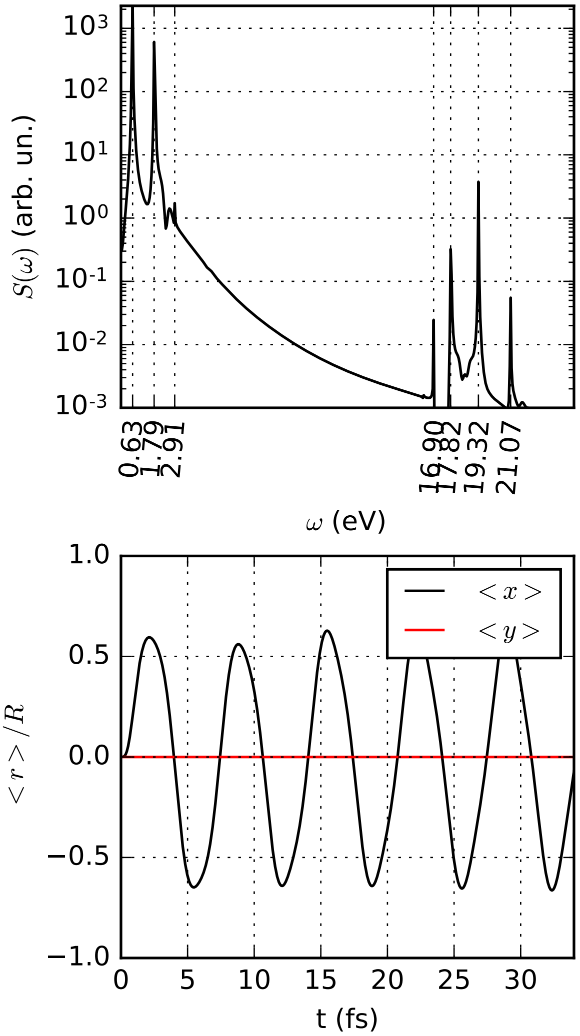

Figure 3.30: In the Top: $S(\omega)$ vs ω; in the Bottom: $\langle r\rangle/R$ vs t. The parameters are: $R = 5$ a.u. $= 2.6 \cdot 10^8$ cm, $U_0 = 2.0$ a.u. $= 54.42$ eV, $\mathcal{E}^u_{0x} = 5.34 \cdot 10^{-3}$ a.u. $= 2.74 \cdot 10^7$ V/cm, $\mathcal{E}^u_{0y} = 0$, $\alpha = 400$, $\beta = \alpha/81920$, $t_x = 0$, $\hbar\omega_L = 0.1139$ a.u. $= 3.10$ eV, $\tau = T_L$, $\mathcal{E}^L_{0x} = 0$, $\mathcal{E}^L_{0y} = 0$.

but in addition we see also, as expected, radial transition with different nodes k, for better understanding we report the transitions in Table 3.5 (see also Fig. 3.6).

		$m = 0$		$m = 1$		$m = 2$		$m = 3$	
		$k = 0$	$k = 1$	$k = 0$	$k = 1$	$k = 0$	$k = 1$	$k = 0$	$k = 1$
$m = 0$	$k = 0$	//	//	0.63 eV	19.32 eV	//	//	//	//
	$k = 1$	//	//	17.82 eV	××	//	//	//	//
$m = 1$	$k = 0$	0.63 eV	17.82 eV	//	//	1.79 eV	21.07 eV	//	//
	$k = 1$	19.32 eV	××	//	//	16.90 eV	××	//	//
$m = 2$	$k = 0$	//	//	1.79 eV	16.90 eV	//	//	2.91 eV	××
	$k = 1$	//	//	21.07 eV	××	//	//	××	××

Table 3.5: The transition energy of the Raman lines showed in Fig. 3.30. // indicate that the transition is forbidden and ×× the allowed transitions absent in the spectrum in Fig. 3.30.

As said before, by changing the symmetry of the system we can control the polarization of the emitted radiation. In this part, we are going to analyze the interaction between 2D QRs and two contemporaneous pulses. We use, an unipolar pulse along $\hat{x}$ and a strong laser field along $\hat{y}$. In addition, from other simulation (see also [101]) we know that a resonant laser could help to increase the ellipticity of the emitted radiation, thus we set ω_L to have 5 photons of resonance with $\{0,2\} \leftrightarrows \{1,1\}$.

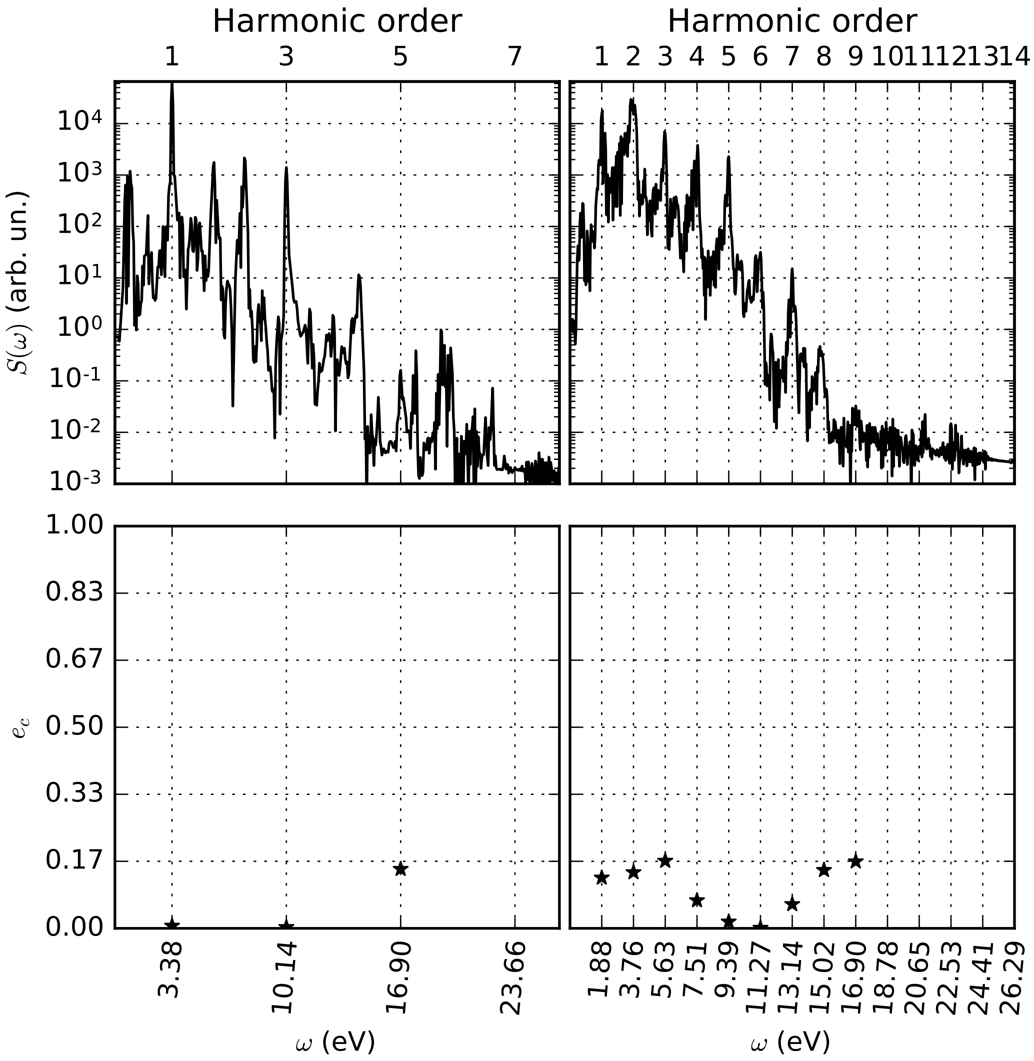

Figure 3.31: In the top: Fourier spectrum; in the bottom: e_c vs ω. The parameters of left side are $\hbar\omega_L = 0.621/5$ a.u. $= 3.38$ eV, $\mathcal{E}^L_{0y} = 3.38 \cdot 10^{-2}$ a.u. $= 1.74 \cdot 10^8$ V/cm, $N_c = 64$. In the right side $\hbar\omega_L = 0.621/9$ a.u. $= 1.88$ eV, $\mathcal{E}^L_{0y} = 4.47 \cdot 10^{-2}$ a.u. $= 2.30 \cdot 10^8$ V/cm, $N_c = 48$. In both cases: $R = 5$ a.u. $= 2.6 \cdot 10^8$ cm, $U_0 = 2.0$ a.u. $= 54.42$ eV, $\mathcal{E}^u_{0x} = 5.34 \cdot 10^{-3}$ a.u. $= 2.74 \cdot 10^7$ V/cm, $\mathcal{E}^u_{0y} = 0$, $\alpha = 400$, $\beta = \alpha/81920$, $t_x = 0$, $\tau = T_L$, $\mathcal{E}^L_{0x} = 0$, $\varphi = 0$.

As first result we look at Fig. 3.31 first column, the spectrum presents only odd harmonics, H1 and H3 are polarized in the same way as the strong laser field, instead H5 is elliptically polarized with $e_c = 0.2$. In addition, we see various lines derived by both radial and angular transitions. In the right column we report the spectrum and the ellipticity obtained by varying the resonance from 5 to 9 photons still with the transition $\{0,2\} \leftrightarrows \{1,1\}$. As matter of fact we note that in this case there is a quasi resonance with another transition ($\{0,1\} \leftrightarrows \{0,2\}$). This could be an explanation of the fact that the spectrum presents even and odd harmonics for largest elliptical polarization around 0.2.

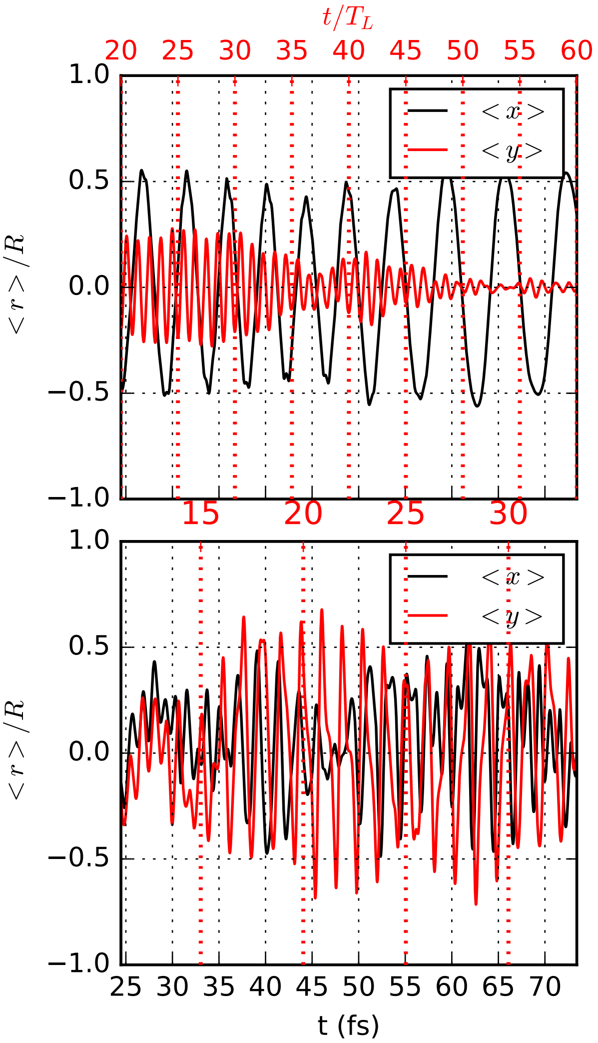

Figure 3.32: $\langle r\rangle/R$ vs t. The parameters are as (Fig. 3.31 left side) in the top, and as (Fig. 3.31 right side) in the bottom.

Another interesting feature to analyze, for the cases presented in Fig. 3.31, is the dipole moment. When we drive the system only with the unipolar pulse we get, more or less, a periodic current only oscillating along $\hat{x}$ (this figure is not reported). We find that for the case with 5-photons of resonance the component of the dipole moment along $\hat{x}$ (top part of Fig. 3.32) is more or less the same that, the one that we get by driving the system only with the unipolar pulse. Instead, in the bottom of Fig. 3.32, $\langle x\rangle$ is really influenced by the presence of the 9-photons resonance laser. It seems that, for our system, it is really important to change the dynamics in the $\hat{x}$-direction for improving the emission of elliptically polarized harmonics.

Thus, this first part of our analysis allows to conclude that working with 2D QRs can help to build device which emits a set of harmonics by selecting different transitions at k fixed as resonance frequency. Of course, it is important to have the possibility to set also the resonance frequency and not only the numbers of photons; by looking at Fig. 3.30 we can select, for $k = 1$, 4 different transitions. For this reason, we show in bottom part of Fig. 3.33 the variation of the polarization of H5 by varying the ω_L according to the 4 transitions in object by keeping fixed the number of photons (5) of resonance. The polarization of H5 is not strongly influenced by the selected frequency, thus we can use 2D QRs as a frequency tunable elliptically polarized radiation emitter.

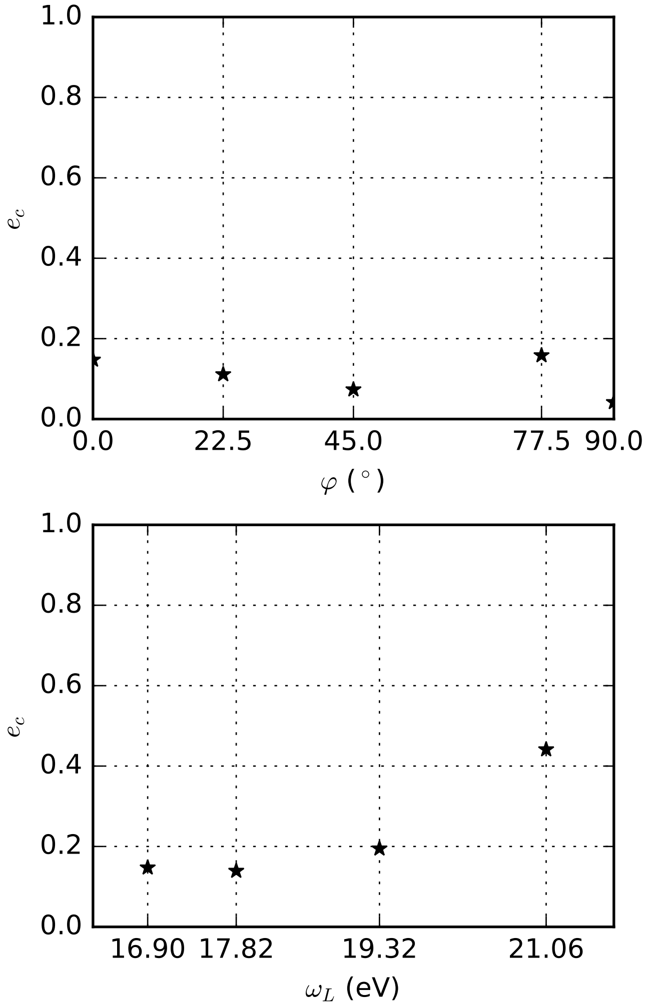

Figure 3.33: Top: e_c of H5 vs the carrier envelope phase φ with parameters as Fig. 3.31 left side; bottom: e_c of H5 vs ω_L with parameters as Fig. 3.31 left side.

We state that the use of two different pulses with different time dependence produces a time dependent polarization, thus we need to study the effect on the polarization of H5 by varying φ the carrier envelope phase of the laser (top part of Fig. 3.33, the other parameters are the same as the left side of Fig. 3.31). We get that it is possible to fine tune the ellipticity of H5 by changing the phase between the two pulses.

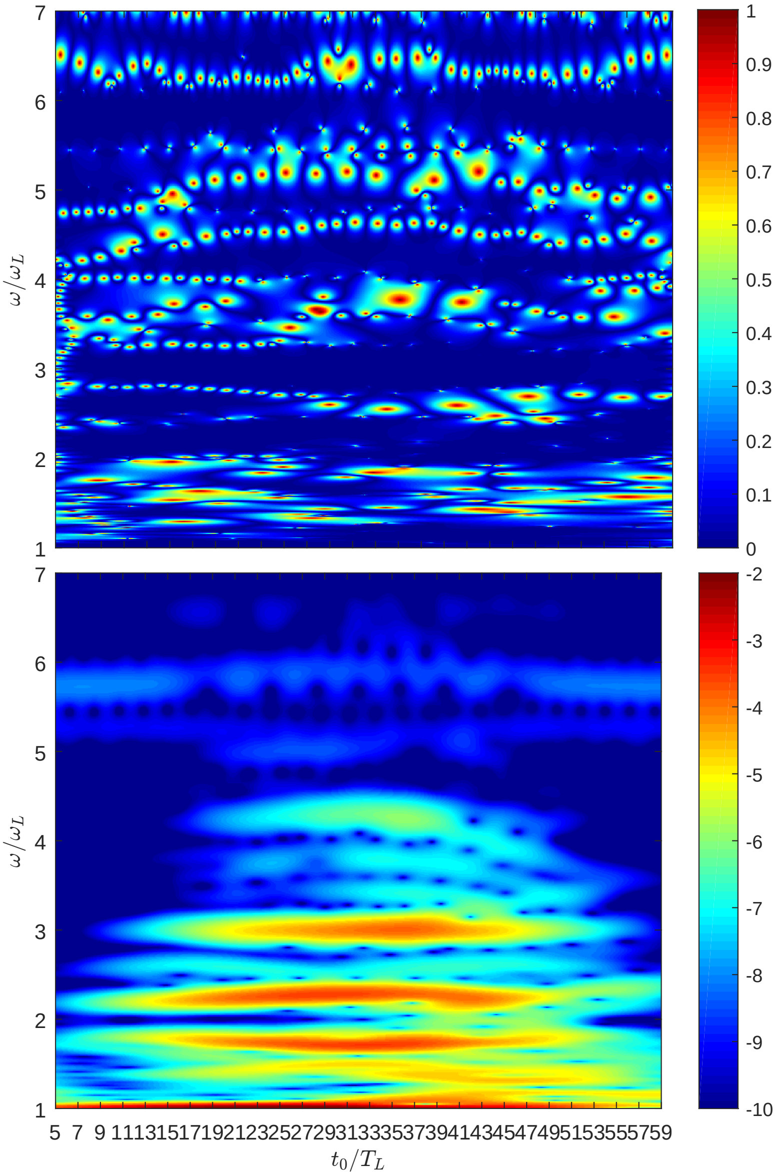

Figure 3.34: Top: $e_c(t_0, \omega)$ vs ω/ω_L vs t_0/T_L; Bottom: Morlet spectrum $\sigma_0 = 5$ with parameters as Fig. 3.31 left side.

In order to get temporal information about the evolution of the emitted radiation both for polarization and intensity, we study the wavelet transforms of the signal. In the top part of Fig.s (3.34,3.35), we look at the time evolution of the ellipticity evaluated by using the Morlet transform instead of the Fourier one $e_c(t_0,\omega)$ (see Sec. 2.7). Looking at Fig. 3.34 it is interesting to note that $e_c(t_0,\omega=\omega_L)=e_c(t_0,\omega=3\omega_L)=0\ \forall t_0$, this means that H1 and H3 has the same linear polarization of the incident strong laser for any time, at the contrary the ellipticity of H5 presents maxima and minima.

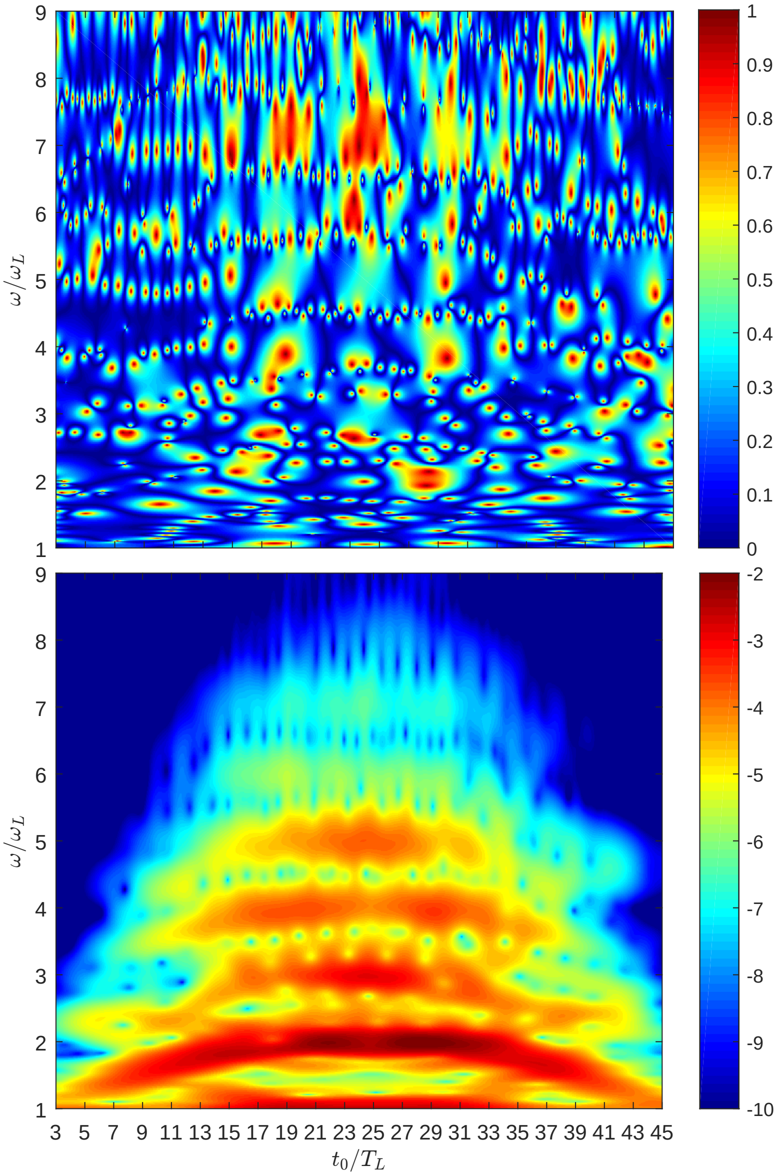

Figure 3.35: Top: $e_c(t_0,\omega)$ vs ω/ω_L vs t_0/T_L; bottom: Morlet spectrum $\sigma_0=5$ with parameters as Fig. 3.31 right side.

Also for this analysis we see that the case at 9 photons (Fig. 3.35) presents a time dependent ellipticity practically for any harmonic. It is interesting to note that when

H7 is at the maximum of emission, $t_0 \approx 24T_L$, the ellipticity $e_c(t_0 = 24T_L, \omega = 7\omega_L)$ is around 0.9 (see Fig. 3.36) Thus with a frequency and time filter it is possible to isolate a quasi circular emission at 13.14 eV.

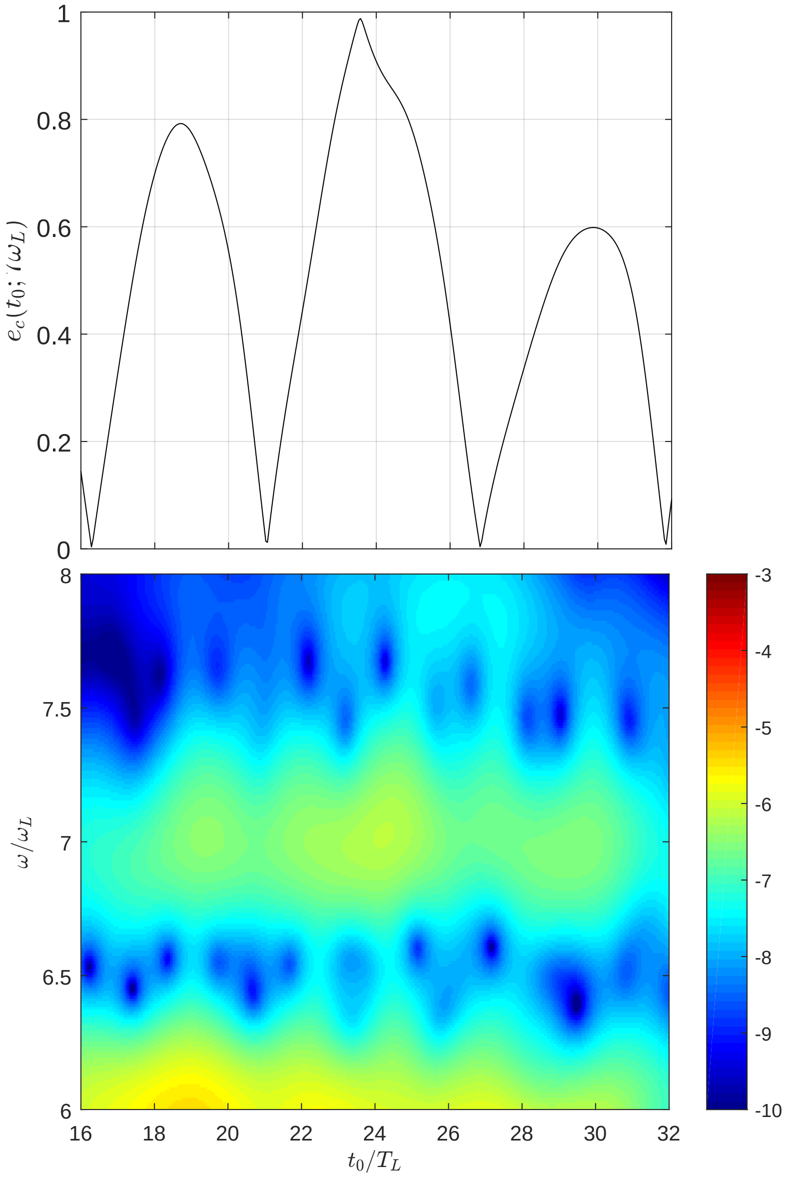

Figure 3.36: Top: $e_c(t_0, 7\omega)$ vs t_0/T_L; bottom: Morlet spectrum $\sigma_0 = 5$ with parameters as Fig. 3.31 right side.

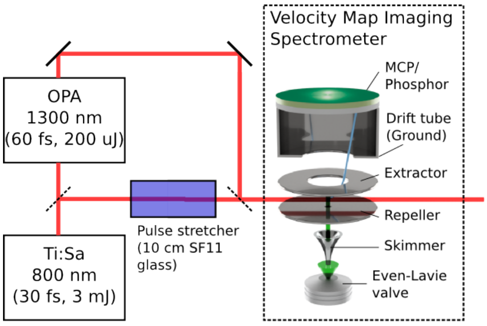

Figure 3.37: Picture of the experimental setup.

3.9 CF_3I

As said before, the goal of this thesis is to study the strong field phenomena from different points of view. In the previous part of this chapter, we characterized the emission of photons, but it is of paramount importance the study of the laser induced electron emission. In order to study the PAD we model CF_3I as described in Sec. 3.4.2. We are interested in reproducing an experiment, where the laser induced electron diffraction technique (LIED) is applied to get molecular and orbitals features of a complicated (containing a heavy atom as I) molecule like CF_3I (see [1, 94]). In order to probe the molecule in the experiment, we use two different ω_L 800 nm and 1300. The idea is to try to reproduce the experimental features by model and simulations in order to separate the contribution of different orbitals and to find some features derived by geometric properties of the molecule itself. To reach the goal, we use mainly three approach, TDDFT theory for finding the orbital contributions, QRT in order to have a simple explanation of the problem, and the modified QRT in order to include the laser contribution in the simple model.

3.9.1 Experimental setup

The scheme of the experiment setup is shown in Fig. 3.37, it has been used a commercially available Ti:Sapphire laser system delivering 2 mJ, 40 fs pulses at 1 kHz repetition rate. In order to align and probe the molecule the output of the Ti:Sapphire is divided in two by using a Mach-Zender, in one of the arm the 800 nm pulse is stretched to 1.2 ps pulse duration in a 10 cm long SF11 glass block, in order to have the pump or aligning laser. The other radiation going out the Mach-Zender, is spatially overlapped with the pump or for the case of 1300 nm is first converted to deliver 150 μJ of 1300 nm light using a commercial optical parametric amplifier (TOPAS-C from Light Conversion). At this point, the lasers are focused inside a Velocity Map Imaging (VMI) spectrometer [108] using a 20 cm lens. In addition, in order to neglect any ionization due to pump we set the waist of the pump with a telescope. The intensity of the probe pulse is setting in a range between $4 \cdot 10^{13}$ - $2 \cdot 10^{14}$ W/cm^2 by using a $\lambda/2$-wave-plate and polarizer. The radiation, described until now, interacts in the center of VMI with a cold molecular beam of CF_3I molecules seeded in helium (seeded ratio 1:100) obtained from an Even-Lavie valve running at 500 Hz. This interaction produces the emission

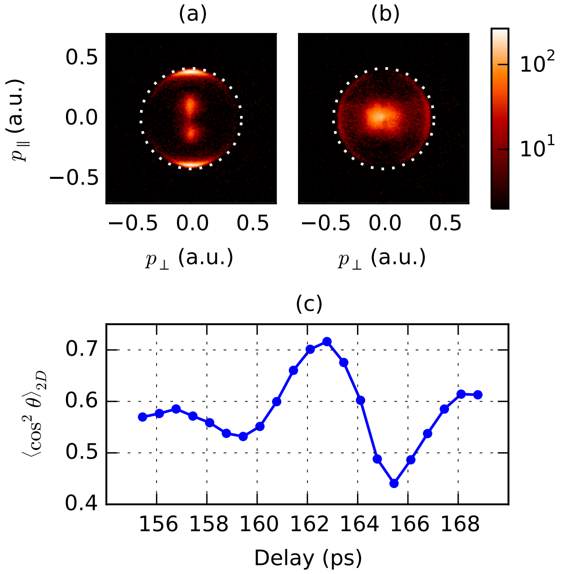

Figure 3.38: 2D PAD, (a) aligned (recorded at 163 ps) and (b) anti-aligned (recorded at 165.5 ps). The Coulomb explosion energy of the I^+/CF_3^+ pair from the equilibrium I–C distance of 2.14 is indicated by white iso-energy circles. (c) $\langle\cos^2\theta\rangle_{2D}$.

of charge particles that are detected by a microchannel plate/phosphor assembly and recorded with a charge-coupled device (CCD) camera. We note here that a high-energy VMI spectrometer specially designed to measure electrons kinetic energy up to 1500 keV is used. In a VMI measurement, a projection of the 3D momentum distribution (electrons and ions) is recorded a the CCD camera. Retrieval of the initial 3D momentum distribution is achieved by applying an Abel inversion based on the pbasex method [109].

3.9.2 Laser-induced molecular alignment

The Laser-induced molecular alignment consists on a strong rotational kick, given by the pump laser, that activates rotation by populating the rotational state, which re-phase periodically and as a result we see alignment revivals at regular interval $\frac{\tau_r}{2} = 163.7$ ps where τ_r is the period of rotation of CF_3I (symmetric top molecule) [110, 111]. Of course, as shown before, the interaction between two pulses and matter can depend on the variations of parameters, to be sure that the molecules are mostly aligned and that the electron is in the field-free conditions, we probe the laser when the alignment is in a maximum or a minimum. In order to measure the degree of alignment we record the I^+ momentum distribution, derived by the Coulomb explosion of the molecules by using the probe laser pulse (800 nm) [111], our system is built up in the way that the polarization of the probe is in the direction of the detector axis and at the same time perpendicular to the one of the pump. In this way, we know that if the molecules are not oriented, they have random positions, the momentum distribution has to be with circular symmetry. In Fig. 3.38 we show for two different times (delays) closed to the first alignment revival, the 2D I^+ momentum distributions. We see a distribution

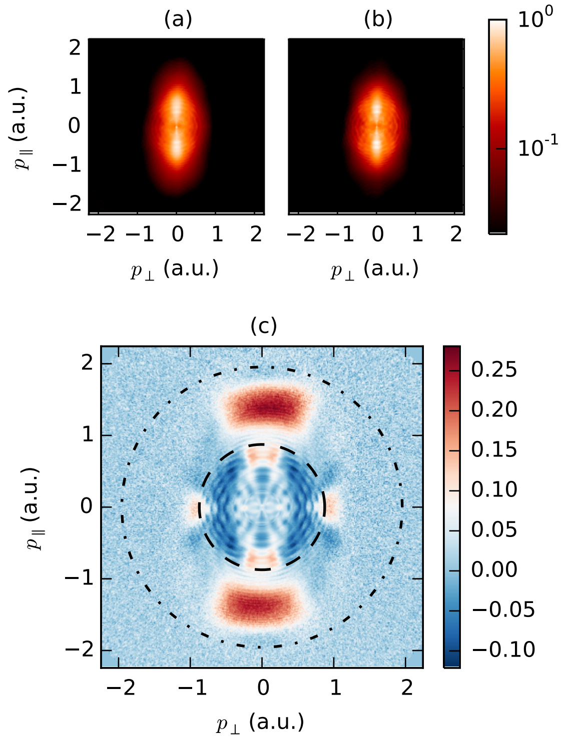

Figure 3.39: PAD evaluated with 800 nm probe at $8.7 \cdot 10^{13}$ W/cm^2: (a) in the left part aligned and in the right one anti-aligned, revival peak; (b) I_Δ, the dash-dotted energy lines indicate $2U_p$-$10U_p$.

presenting in the inner part a broad structure, due at the dissociating ionization of CF_3I molecules into CF_3 neutral fragments and I^+ ion, and later a sharp ring that has the correct correspondent kinetic energy of 2.37 eV as the one due to the Coulomb explosion of the I^+/CF_3^+ pair from the equilibrium I–C distance of 2.14 . In the part (a) of Fig. 3.38, we see that I^+ momentum distribution peaks in direction of the probe polarization, instead in the part (b) the distribution peaks at anti-alignment. In the (c) part of Fig. 3.38 we show the value of $\langle \cos^2 \theta_{2D} \rangle$, where θ_{2D} is the angle between the pump polarization axis and the recoil direction of the fragment ion. It is possible to estimate of θ, the angle between the laser polarization axis and the molecular axis, by fitting the results of the TDSE on temperature and intensity. The best fit leads a degree of alignment of 0.7 for temperature equal to 7 K and an intensity of 5.10^{12} W/cm^2.

3.9.3 Photoelectron angular distributions

In Figs. 3.39 and 3.40 are reported the PADs for both aligned and anti-aligned molecules (aligned in the direction perpendicular with respect the laser field polarization axis) respectively for 800nm and 1300nm. In addition, we plot in (c) of Figs. 3.39 and 3.40 the normalized difference given by

$$I_\Delta = \frac{I_{align} - I_{anti-align}}{I_{align} + I_{anti-align}} \tag{3.4}$$

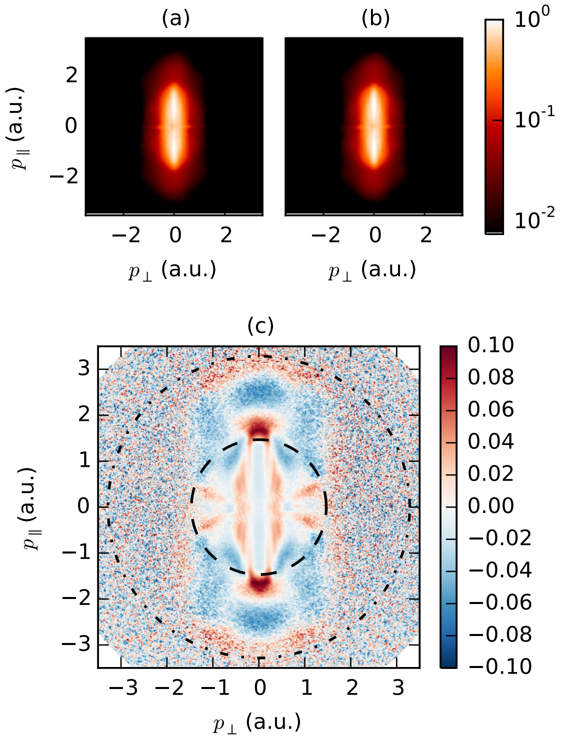

Figure 3.40: As Fig. 3.39, with 1300 nm probe at $9.3 \cdot 10^{13}$ W/cm^2.

this allows us to see differences that are non visible by looking at aligned and anti-aligned PADs. For instance, if we look at the 800 nm case we see that the aligned configuration in the high-momentum (energy) region shows an increase of 25 $\%$ compared to the anti-aligned case. Moreover the case of 1300 nm presents a $\pm 10\%$ oscillations of the electron yield in the direction of probe polarization. In addition, both at low and high momentum we see large oscillations. As explained in the introduction of this thesis, by a strong field point of view we can divide the PADs into two parts a direct part in the inner of the circles, indicated by the dashed and dash-dotted circles respectively in Figs. 3.39c and 3.40c, and a rescattering part outside, as matter of fact in the region $E_k < 2U_p$ both the direct and re-scattered electrons contribute (Figs. 3.39c and 3.40c).

As shown in various researches by looking at the low momentum region is possible to reconstruct the shape of the molecular orbitals (clearly the one from that the electron came out)[112, 113]. Indeed, our plots (Figs. 3.39c and 3.40c) show in the direct region a large blue (negative) zone in the direction of the laser polarization axis due to the nodal plan of the HOMO orbital of CF$_3$I molecules. In the second regions, both for the 800 nm than for the 1300 nm cases, we observe a pronounced oscillation, always along the laser polarization axis ($p_\parallel$), the contribution of photoelectrons that have experienced a hard re-collision (back-scattered photoelectrons) with the parent ion is dominant [7].

As we said before, classically the maximum energy at the momentum of recollision is $3.17U_p$, that, for an intensity of 9.10^{13} W/cm^2, is 17 eV and 45 eV (which correspond to a wavelenght of 300 pm and 180 pm) respectively for the 800 nm and 1300 nm. These last values are comparable with the I-F and C-I internuclear distances (270 and 214 pm, respectively), consequently we see features of the molecular structure in the high energy region of PAD.

3.9.4 Discussion and analysis

Time-dependent density functional theory

In order to reproduce, the experimental results and to include every contributions due to molecular and orbital structure, we have performed ab-initio calculation based on the time-dependent density functional theory [89]. We describe the dynamics of the valence electrons of CF_3I by means of TDDFT; as said before, we model the inner shell orbitals by pseudo-potentials in this case, we use a modified Fritz-Haber Institute (FHI). We use the adiabatic local-density approximation (ALDA) with an average-density SIC which corrects the tail of the Coulomb potential and yields an accurate ionization potential.

In general, simplified models do not consider the ionization from orbitals different from the HOMO, but previous experiments performed in aligned molecules (CO_2 [114, 115]) driven by strong laser field show that the ionization from the HOMO is suppressed when the molecules is aligned, and that the ionization from the HOMO-2 is enhanced. Thus, we expect that in the case of aligned molecules the contribution is mainly from HOMO-1.

If the simplified model based on the quantum rescattering theory allows to identify some of the features observed experimentally to diffraction of rescattered photoelectrons, it fails in reproducing quantitatively the results obtained at longer wavelength. In this model, it is assumed that ionization takes place from the highest occupied molecular orbital and that the returning electron wave-packet can be well approximated by a plan wave. Previous high harmonic generation experiments performed in aligned CO_2 molecules [115] and strong field ionization experiments performed in saturated (n-butane) and unsaturated (1,3-butadiene) linear hydrocarbons [114] have shown the important role of possible multiple electronic ionization channels in the process. In the former experiment, it was shown that high harmonic generation from the HOMO orbital is suppressed in CO_2 when the molecules are aligned along the laser polarization due to the presence of a nodal plan whereas ionization from the HOMO-2 orbital is enhanced. We expect a similar behaviour from CF_3I molecules where ionization from the HOMO orbital is suppressed when the molecule is aligned along the laser polarization.

In order to reproduce the experiments we use, in addition to the two different wavelength, two different laser intensities $I_1 = 3.4 \cdot 10^{13}\mathrm{W/cm^2}$, $I_2 = 7.7 \cdot 10^{13}\mathrm{W/cm^2}$, and $I_3 = 4.7 \cdot 10^{13}\mathrm{W/cm^2}$ with $\lambda_1 = \lambda_2 = 800\,\mathrm{nm}$, and $\lambda_3 = 1300\,\mathrm{nm}$ comparable to the experimental conditions. The pulse length is $N_c T_L = 26.68\,\mathrm{fs}$ for λ_1 and λ_2 and $N_c T_L = 43.38\,\mathrm{fs}$ for λ_3, linearly polarized along the z-axis. In order to get our goal, we do not consider possible oscillation of the ions thus we kept them frozen. We choose a Cartesian grid of spherical shape of radius $R = 80\,a_0$ which is large enough to accommodate the quiver length. Photoelectron spectra are analyzed with the time-dependent surface flux method with a spherical surface located at $R = 80\,\mathrm{au}$ (up to an angular momentum $L_{\max} = 40$), emitted electrons are absorbed by a complex absorbing potential of width $L = 30\,\mathrm{au}$ and height $\eta = 0.2\,\mathrm{au}$ located at $r > 50\,\mathrm{au}$.

As explained in the theory section, the TDDFT calculations yield a three dimensional momentum probability distribution $P(p, \vartheta, \varphi)$, in order to compare this distribution with the VMI image we have to consider some effects

- the delocalization effect of the molecule in the plane perpendicular to the laser,
- the projection of the 3D momentum distribution onto a plane perpendicular to the laser polarization axis, in order to mimic the action of the detector,
- the degree of alignment of the molecule with respect to the laser polarization axis, in order to consider that the molecules are not perfectly aligned but distributed around the alignment angle.

In order to consider the delocalization we average P in the angle φ (the angle in the plane X-Y), in order to mimic the action of the detector we integrate the data along an axis perpendicular to the laser polarization, and in this way we get a momentum distribution $I(p_{\parallel}, p_{\perp})$. Thus, similarly to the experiment we calculate I_{Δ}. And, at this point we can consider the distribution of the molecules in the space, for the degree of alignment we assume $\langle\cos^2\beta\rangle_{\text{align}} = 0.72$ for the aligned, and $\langle\cos^2\beta\rangle_{\text{anti-align}} = 0.45$ for the anti-aligned configuration, and for the average we suppose a distribution $n(\beta) = \frac{e^{-\frac{\sin^2\beta}{2\sigma^2}}}{N}$ with $\sigma^2 = 1 - \langle\cos^2\beta\rangle$ around the (aligned/anti-aligned) starting configuration.

In Fig. 3.41, we report the simulated total PADs I_{Δ}, by using the expedients described before, as a function of the momenta $p_{\parallel}$ and $p_{\perp}$ parallel and perpendicular to the laser (right part of the color maps), in comparison with experimental results (left part). As expected, for any consider laser the results match remarkably well with experiment, this confirms that TDDFT could describes the dynamics of the strong-field ionization appropriately.

At this point, relying on the fact that, our simulations correctly reproduces the experiment, we can analyze the contributions of each Kohn-Sham orbital to the total PADs, see Fig. 3.42. For any configuration, we find out that only the two highest orbitals (HOMO and HOMO-1) contribute to the total I_{Δ}, thus we do not need to consider ionization from the lower states. In addition, we see that they contribute in different zones and they produce different features on the PADs.

1. the HOMO-1 PAD is mainly structureless while the HOMO PAD shows features in particular in the low-energy region,
2. the orbital difference I_{Δ}^{HOMO} for the HOMO orbital (second row in Fig. 3.42) is, in general, dominated by the anti-aligned configuration (yielding negative values), while for the the HOMO-1 (third row) it is the opposite (yielding positive values)

Then, we can state that the red features in the total PAD come out by the HOMO-1, while blue features are dominated by the HOMO.

Actually, this distinction of the features in the total PAD can be most clearly seen for $\lambda_1 = 800\,\text{nm}$ and $I = 3 \times 10^{13}\,\text{W/cm}^2$. When the intensities is higher or the wavelengths is longer, the contribution of HOMO-1 is more structure-less, and both HOMO and HOMO-1 seem to have more or less the same contribution in the low-energy region. This means that for longer wavelengths/higher intensities we have to look at

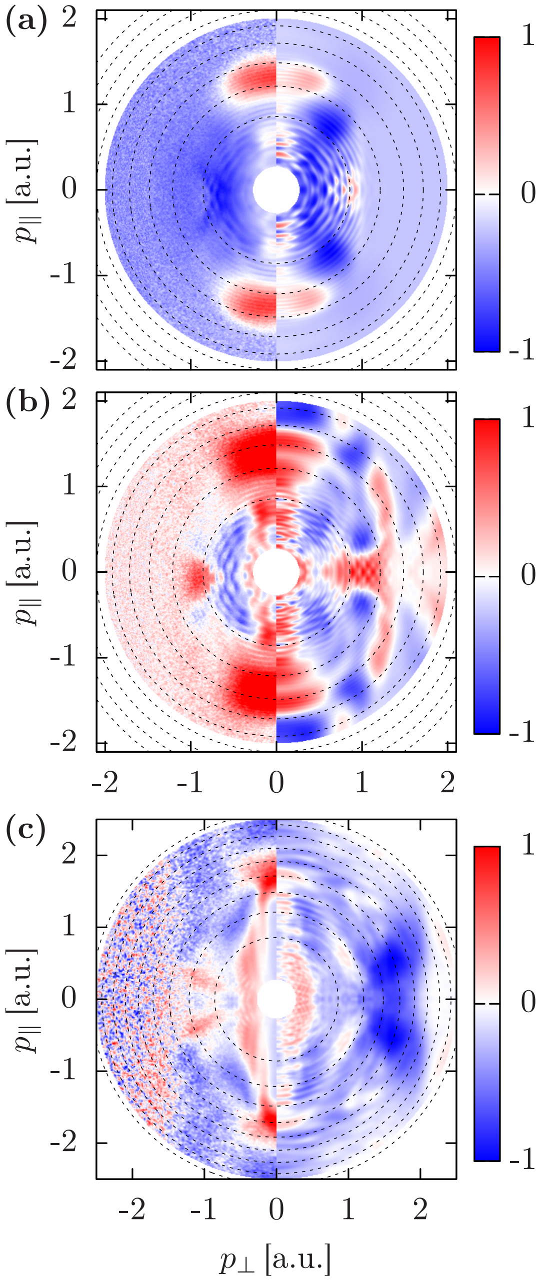

Figure 3.41: Comparison between the experiment and TDDFT for (a) $\lambda_1 = 800\,\mathrm{nm}$ and $I_1 = 3.4 \times 10^{13}\,\mathrm{W/cm^2}$, (b) $\lambda_2 = 800\,\mathrm{nm}$ and $I_2 = 7.7 \times 10^{13}\,\mathrm{W/cm^2}$, and (c) $\lambda_3 = 1300\,\mathrm{nm}$ and $I_3 = 4.7 \times 10^{13}\,\mathrm{W/cm^2}$. The left part shows the experiment, the right part the TDDFT result. Rings indicate kinetic energies of 10, 20, 30 eV, etc.x-axis: momentum perpendicular to laser polarization axis (in a.u.); y-axis: momentum parallel to laser polarization axis.

higher energy to distinguish, between the contribution of the two different orbitals. At first glance, this supports the idea that by setting the polarization of the laser along the nodal plane of the HOMO the probability of ionization from this orbital notebly decreases. The large contribution of the HOMO-1, however, is remarkable. In particular, the strong red scattering features in the total PAD around, $E = 1.3$

a.u. (800 nm), $E = 1.7$ a.u. (1300 nm), along the polarization axis originate from the HOMO-1. Instead, the HOMO-1 shows a nodal plane for the anti-aligned case, thus the ionization in this case is suppressed.

By looking at the forth row of Fig. 3.42, showing the comparison of experimental and simulating data along the laser polarization axis, we clearly see that the big pump in the PADs are originated by HOMO-1 and that the position of the peaks is well determined especially for 800 nm and higher intensity.

We conclude that we can ascribe significant parts of the PAD to the HOMO and HOMO-1 orbitals justifying our theoretical multi-electron approach based on TDDFT.

The quantitative rescattering theory

As next step, we want analyze the features of the PADs from the point of view of a simple model based on the quantitative rescattering theory from Refs. [116, 7]. This model is in general used for high energy as explained in Sec. 1.5.2, but its applicability to low energy electron diffraction may be justified by the fact that the momentum transfer value is relatively large for the *back-scattered* electrons that we are considering by looking at the $2\text{-}10U_p$ energy range [6]. To begin with we evaluate the scattering amplitudes by using the elastic electron-atom scattering code (ELSEPA) by [117]. We generate the aligned and the anti-aligned PADs and later we evaluate the normalized difference.

In the simulation we consider CF_3I molecule at its equilibrium geometry and, as first, we consider a simplified two-center scattering model considering only the C–I bond. The results thus obtained are shown in the Fig. 3.43 and 3.44. In the case of the two-center scattering model, from the QRT theory (Eq. 1.73) we obtained that

$$I_M = |f(q)|^2 \left(2 + 2\cos\vec{q}\cdot\vec{R}\right). \tag{3.5}$$

where $\vec{R}$ is the characteristic distance between iodine and carbon center. Of course, in this simple model we neglect the contribution of the total geometry of the molecule and we study only the contribution of C–I distance, the results will elucidate if the total geometry of the molecule plays a role. Fig. 3.43 shows the simulation for 800 nm probe laser and an intensity of $7\cdot10^{13}\ \mathrm{W/cm^2}$, both for the QRT considering the full molecule that for the two atoms scattering center model. As said before, in the inner part there is the dominating contribution of direct electrons that is not described by QRT, thus as expected the inner comparison is not good, actually the higher energy region (momenta above 1.0 a.u., i.e. above $2U_p$) the simulations are in relatively good agreement with the experimental data. The model reproduces a clear maximum along the polarization axis ($p_{||}$) in the back-scattering region which is due to diffraction effects. Looking at the second row of Fig. 3.43, we see that the position of the maximum and overall shape of the re-collision electron momentum distribution in our experiment is well reproduced by the model that considers the CF_3I molecule at its equilibrium geometry. As matter of fact, the two-center model show a maximum shift at 1.7 a.u. from 1.45 a.u. A simple calculation of the oscillation period expected from diffraction due to the I–F pair gives 1.15 a.u.. And this is in perfect agreement with the idea that the first maximum will be shifted to lower momentum as observed in the model including all fluorine atoms.

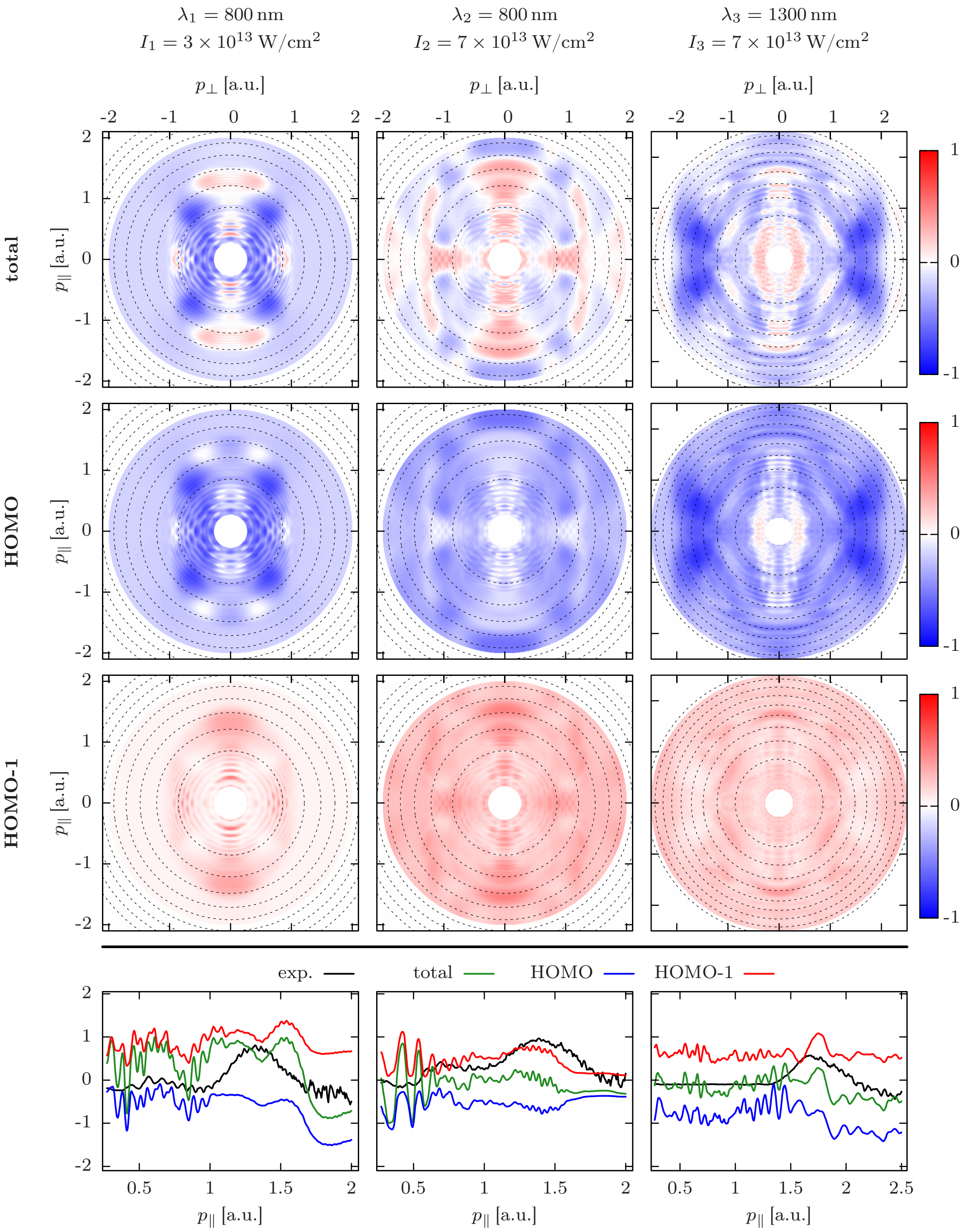

Figure 3.42: First row: Total PADs I_Δ from TDDFT for 800 nm (first and second column) and 1300 nm (third column). Second row: contributions I_Δ^{HOMO-1} from $HOMO-1$. Third row: contributions I_Δ^{HOMO} from $HOMO$. Fourth row: cuts along the laser polarization axis.

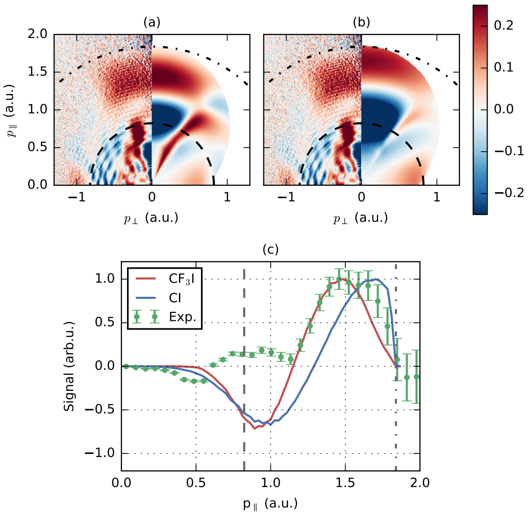

Figure 3.43: Experiment (800 nm probe) vs QRT model: (a) CF_3I molecule simulation, (b) C–I simulation, and (c) cut along the polarization axis $p_\parallel$ (experiment green dots and simulating red and blue lines, respectively). The $2U_p$ (dashed) and $10U_p$ (dash-dotted) iso-energy circles are shown in order to underline the energy zone.

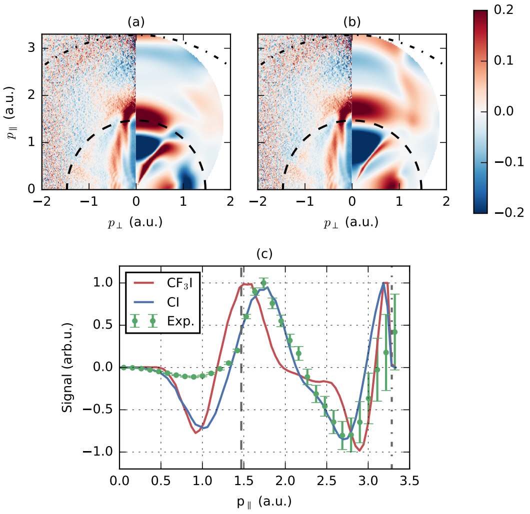

Figure 3.44: As Fig. 3.43 but with 1300 nm.

In Fig. 3.44 we report the PADs simulated for 1300 nm, in this case we observe that the pronounced oscillations is around 1.8 a.u./2.7 a.u. and shifted by 0.2 a.u. for the simplified two-center model. Remarkably, the simulation performed using the simplified two-center model (see Fig. Fig. 3.44b and c) reproduces this time very well both the two big red features in the high-energy re-collision plateau. This suggests that the contribution from the fluorine atoms are overestimated in our model when considering electrons with higher collision kinetic energy.

3.10 OCS

In this section, we compare data from an experiment about aligned molecules and simulations. Here we are going to probe a gas of molecules of OCS that is a linear molecule, thus with a strong dipole moment, which allows a degree of alignment higher than CF_3I (see [95]).

3.10.1 Configuration.

As said before we consider the molecule "aligned" when the molecular axis is *parallel* to the probe laser polarization axis ($= z$-axis), and "anti-aligned" when the molecular axis is perpendicular to the z-axis. To include the "anti-aligned" delocalization of the molecule we average in the angle φ. All calculations are performed in a spherical box. After excitation of the system, we get the ARPES as a function of $\sigma = \sigma(k, \vartheta, \varphi)$. We transform the averaged distribution into Cartesian coordinates and integrate along an axis perpendicular to the laser polarization (here the x-axis). This yields a distribution $\sigma = \sigma(k_y, k_z)$, see Fig. 3.45.

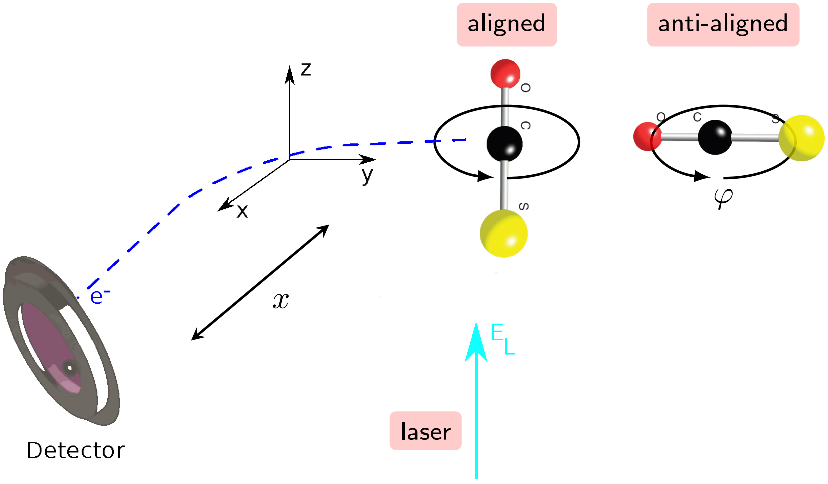

Figure 3.45: Schematic representation of configuration A.

3.10.2 A sample TDDFT calculation

In analogy with the result in Sec. 3.9.4 we expect that the HOMO contribution in the aligned configuration should be suppressed. In this case the contribution of the total aligned ionization of HOMO-1 is less important than for CF_3I, then only the HOMO orbital contributes and the anti-aligned configuration presents a higher ionization than the aligned one (note: recently we found that for larger wavelenghts and intensities the contribution of HOMO-1 is important also for the PAD of OCS [95]). We consider a pulse of $\omega_L = 1.55\,$eV and pulse length of $N_c T_L = 35\,$fs with a $\sin^2$ envelope. An example of the ionization as a function of time is shown in the right panel of Fig. 3.46 for a laser intensity of $I = 3.41 \times 10^{13}\,\mathrm{W/cm^2}$.

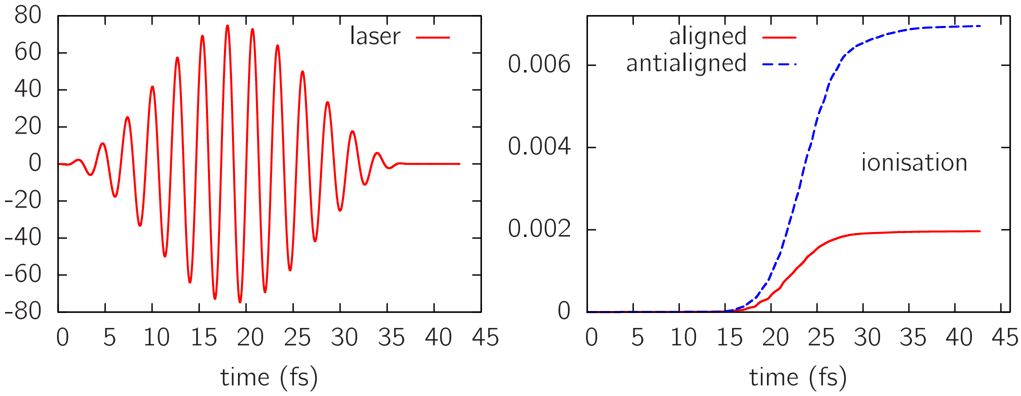

Figure 3.46: Left side: laser vs t; Right side: ionization vs t (for aligned and anti-aligned molecules). With $I_0 = 3.41 \times 10^{13}$, $\mathrm{W/cm^2}$, $\omega_L = 1.55\,\mathrm{eV}$, pulse duration $= 35\,\mathrm{fs}$.

Figure 3.47 shows the corresponding spectrum. For this configuration, we can clearly observe the ATI peaks.

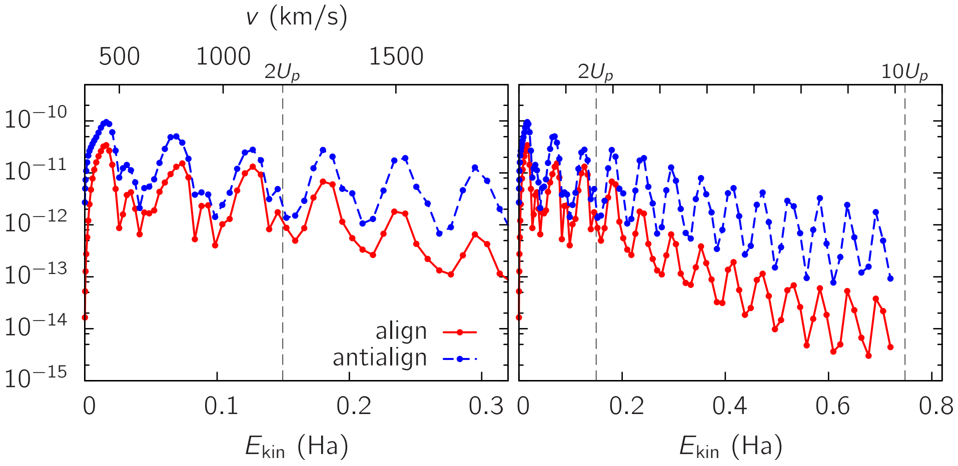

Figure 3.47: Photoelectron spectrum for aligned and anti-aligned case for the laser parameters as in Fig. 3.46.

Figure 3.48 shows the ARPES of this calculation (left: aligned; right: anti-aligned). Both pictures have the same color scale, hence the anti-aligned case dominates (as can be seen also in the spectra).

A comparison to experimental results is shown Fig. 3.49. Here and in the following, we consider the distribution

$$I_D = (I_{\text{antialigned}} - I_{\text{align}})$$

(in order to remove the isotropic background). The experimental data agrees well with the TDDFT calculations. However, the main discrepancy is that some features are strongly washed out in the experiment. In this figure we observe the presence of a big washed out peaks around $k_z \approx 500$ and $k_y = 0$, and a cross-like structure passing from the center of the axis and with a maximum velocity around 300. There are two

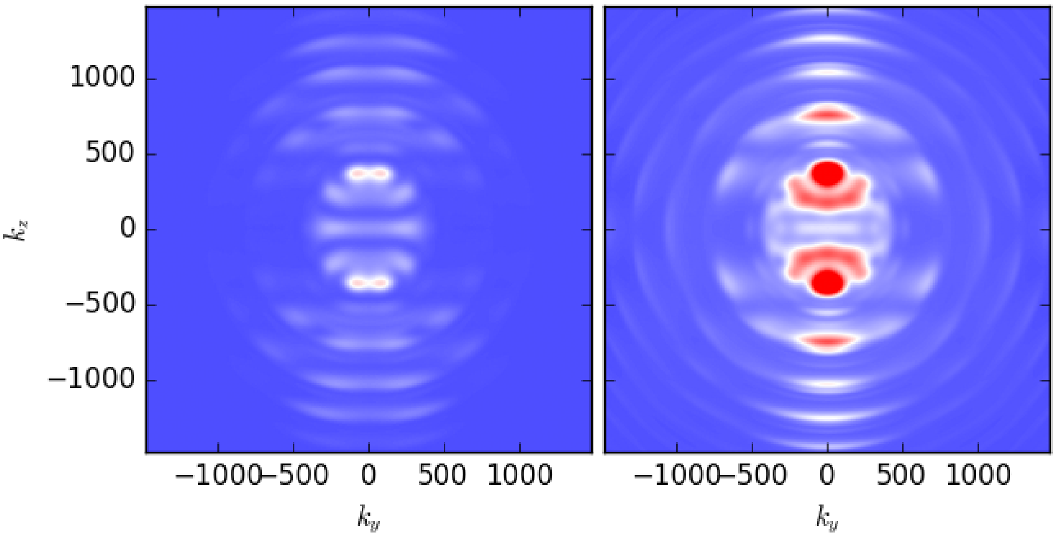

Figure 3.48: Angle-resolved photoelectron spectra for aligned and anti-aligned cases. Left: aligned; Right: anti-aligned configuration.

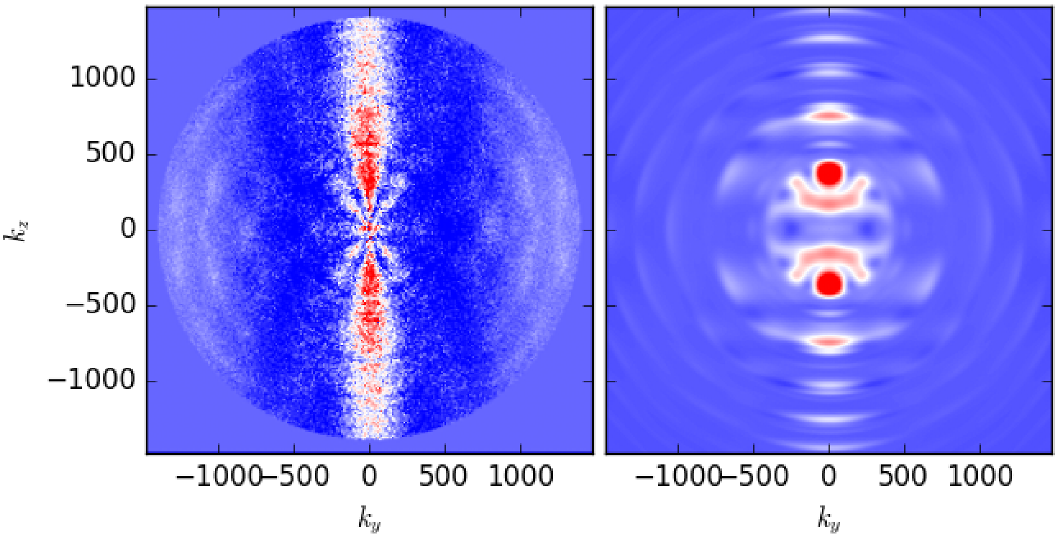

Figure 3.49: Comparison of ARPES from experiment and theory.

main effects that one has to consider working on comparison with simulations and experiments. The first is the fact that the experimental molecules are not perfectly aligned, as said before, we name the effect misalignment, and the second is that the value that we use as intensity of the laser is an estimation of the experimental value, measured by calculating the average value of the intensity distribution.

3.10.3 Misalignment effect

For the misalignment, we use a Gaussian distribution which provides a good approximation, as above, [30]:

$$n(\vartheta) = \exp(-\sin^2(\vartheta)/(2\sigma^2)) \,,$$

with $\sigma^2 = 1 - \langle\cos^2(\vartheta)\rangle$.

Figure 3.50 shows the spectra for aligned/anti-aligned cases, we see that now the intensities of the two spectra are closer.

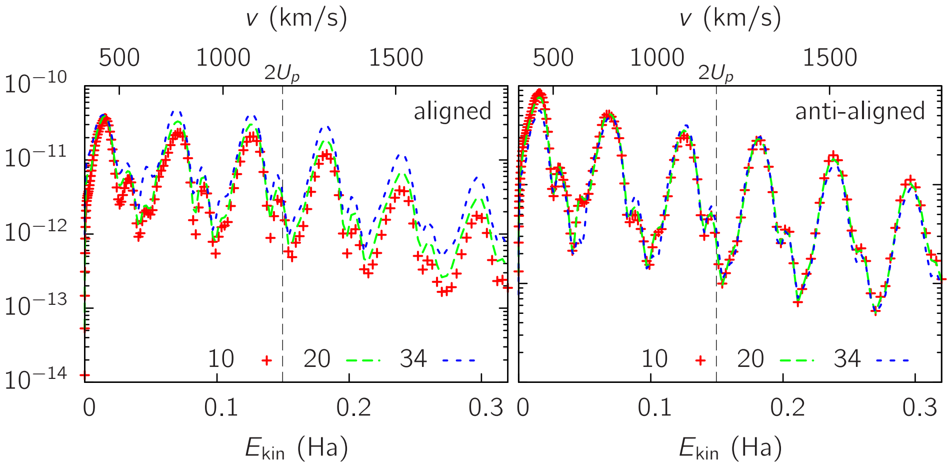

Figure 3.50: Photoelectron spectra for the different misalignment angles $\vartheta_1 = 10°$ (red), $\vartheta_2 = 20°$ (green), and $\vartheta_3 = 34°$(blue) for fixed laser intensity of $I = 3.41 \times 10^{13}\,\mathrm{W/cm^2}$. The other parameters are as in Fig. 3.46

The right panel in Fig. 3.51 shows the ARPES summed over all misalignment angles (considering the proper weight factors) compared with the experimental result (left panel). The misalignment decreases the contribution of the anti-aligned configuration (which is largest) and weakens the strong feature along the laser polarization axis.

3.10.4 Volume effect

Besides the misalignment, there exist also the volume effect, meaning that the experimental intensity is not known exactly. Therefore, we investigate different laser intensities:

- $I_1 = 2.84 \times 10^{13}\,\mathrm{W/cm^2}$
- $I_2 = 2.98 \times 10^{13}\,\mathrm{W/cm^2}$

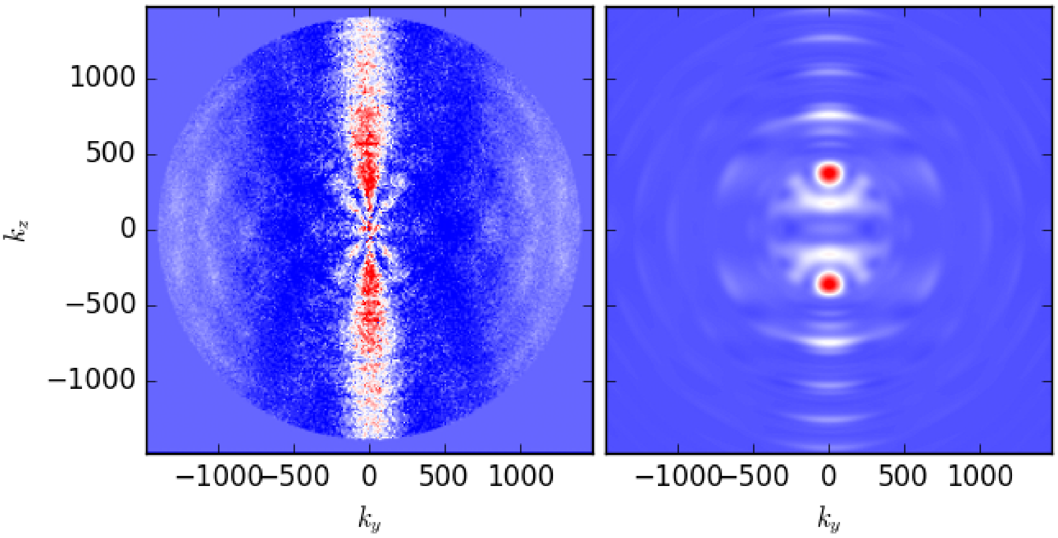

Figure 3.51: Comparison of PAD from experiment and theory by considering the misalignment effect.

- $I_3 = 3.13 \times 10^{13}\,\mathrm{W/cm^2}$
- $I_4 = 3.27 \times 10^{13}\,\mathrm{W/cm^2}$
- $I_5 = 3.41 \times 10^{13}\,\mathrm{W/cm^2}$

Figure 3.52 shows the spectra for aligned/anti-aligned cases.

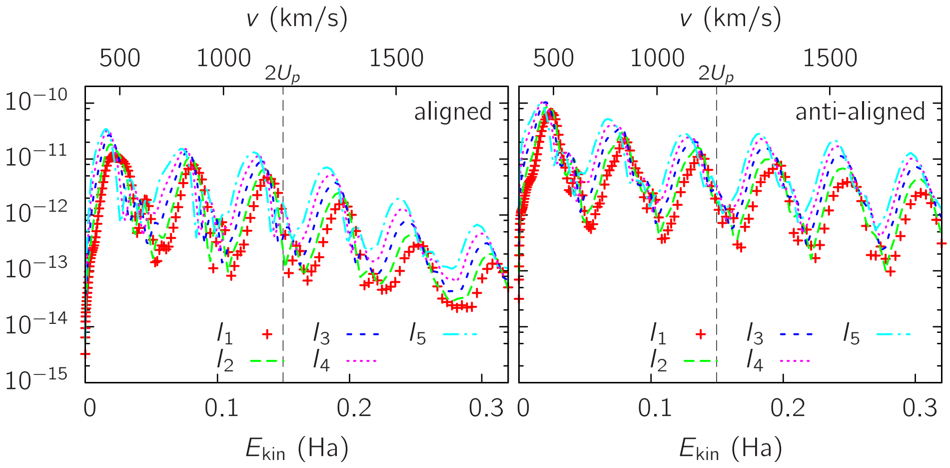

Figure 3.52: Photoelectron spectra for the different laser intensities, $I_1, \ldots, I_5$ for the "perfectly" aligned and anti-aligned cases (i.e., no misalignment included). The others parameters are as in Fig. 3.46

The right panel in Fig. 3.53 shows the ARPES summed over all laser intensities compared with the experimental result (left panel). The volume effect underlines the cross-like structure.

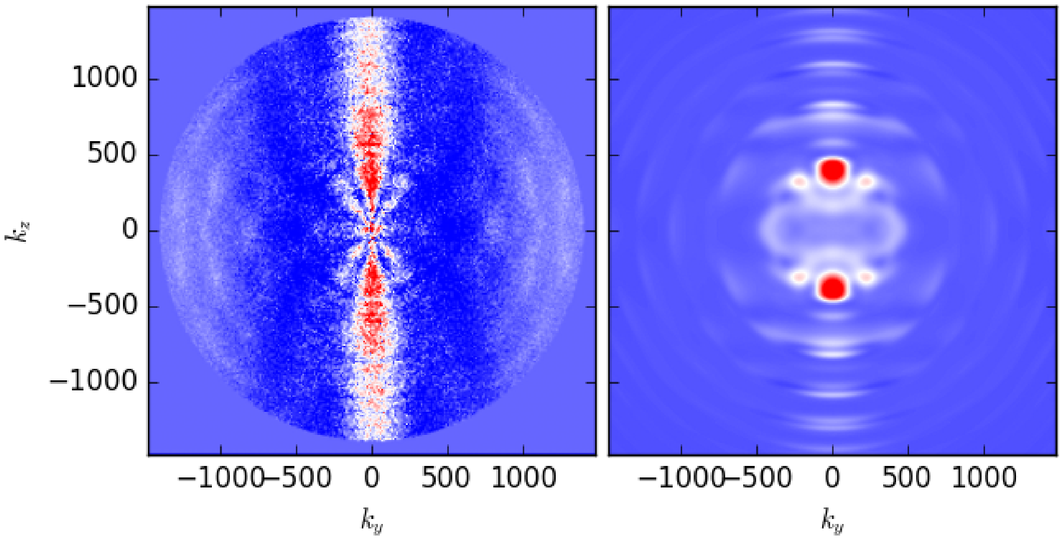

Figure 3.53: Comparison of PAD from experiment and theory by considering the volume effect.

3.10.5 Orbital contributions

Having explored misalignment and volume effect, we now turn to the contribution of each orbital to the total result. Figure 3.54 compares the total theoretical result from Fig. 3.49 (right panel) to the one obtained only for the HOMO orbital (Fig. 3.49 and Fig. 3.54 are normalized differently). As one can see, the main contributor to the total PAD is the HOMO orbital.

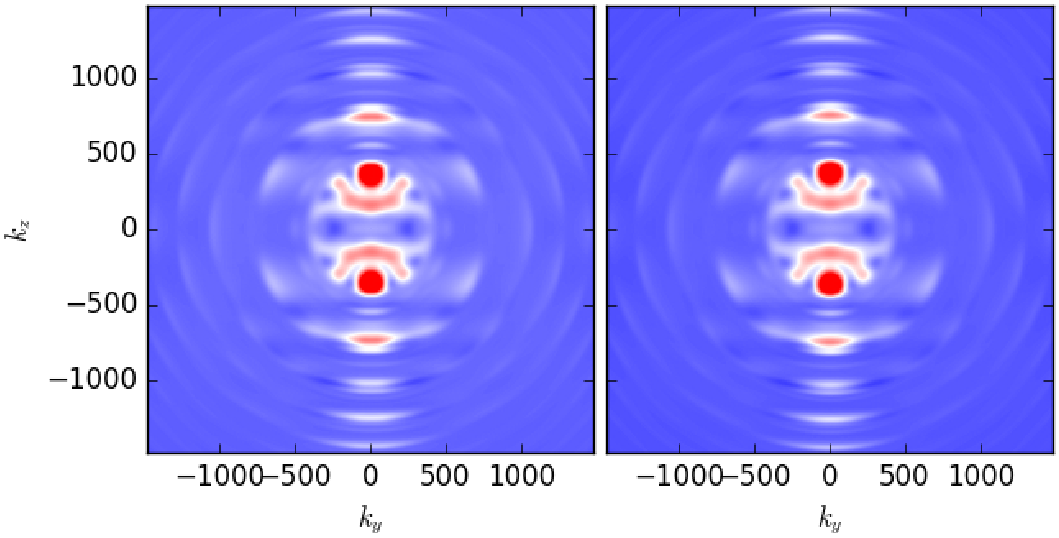

Figure 3.54: Left side: TDDFT-HOMO. Right side: Total TDDFT.

The HOMO orbital is twofold degenerate (hosting four electrons). In the aligned case, the laser polarization is located in the mirror plane for both HOMO orbitals as shown in Fig. 3.55. In the anti-aligned case, the laser polarization axis is located in the mirror plane of only one HOMO orbital (denoted as HOMO 2). Therefore, we expect a difference between HOMO 1 and HOMO 2 only for the anti-aligned configuration. Particularly, in the anti-aligned case only HOMO 1 contributes to the PAD, the HOMO 2 contribution has practically the same distribution than in the aligned case, but is negligible in the anti-aligned case (is this due to the different extension of the orbital).

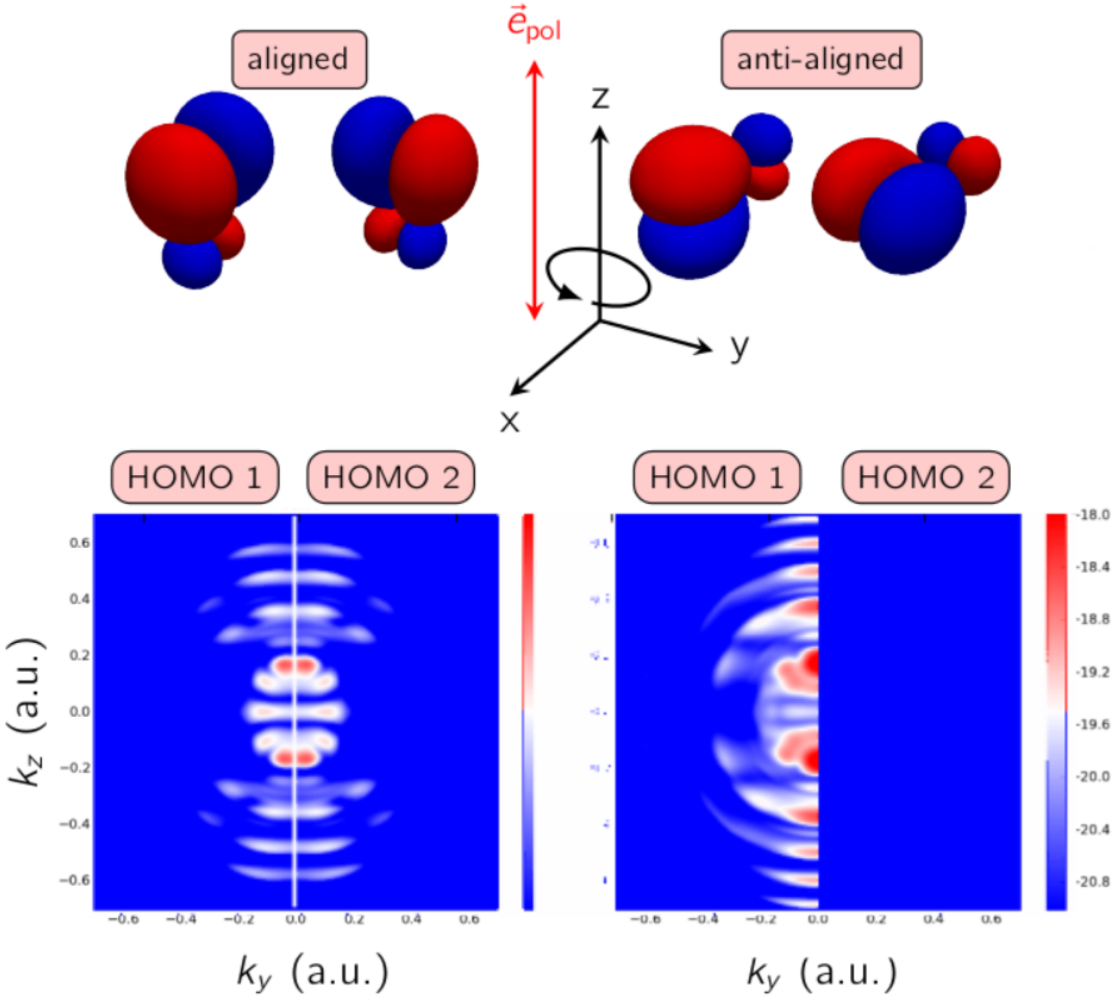

Figure 3.55: Orbitals and PAD for the laser intensity of $I = 3.41 \times 10^{13}\,\mathrm{W/cm^2}$.

Figure 3.56 shows the photoelectron spectrum (PES) of the HOMO orbitals as a function of misalignment angle ϑ. For the HOMO 1, $\vartheta = 0$ means that the laser polarization lies in the mirror plane, while for $\vartheta = 90$ the polarization is perpendicular to the mirror plane of the orbital. This causes a difference of approximately 2 orders of magnitude in the ionization cross section, i.e., ionization increases from $\vartheta = 0$ to $90°$. For the HOMO 2, the polarization axis remains in the mirror plane for all ϑ and variation of ϑ changes the ionization only little.

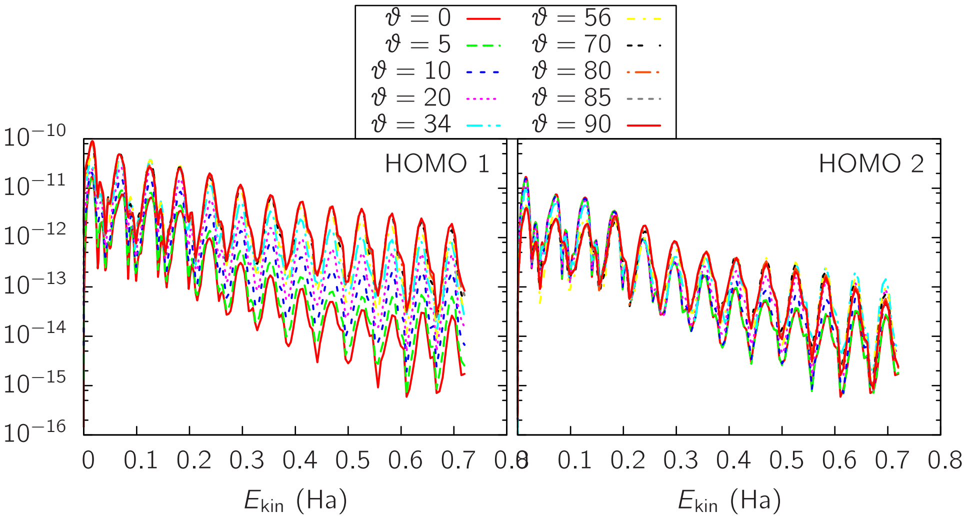

Figure 3.56: Photoelectron spectra for the HOMO orbitals (HOMO 1 and 2) as a function of the misalignment angle ϑ. $\vartheta = 0$ corresponds to the aligned configuration, $\vartheta = 90$ corresponds to the anti-aligned configuration as depicted in Fig. 3.55.

3.10.6 SAE calculations

In this section we explore the effect of multi-electron correlations. Therefore, we make calculations for fixed K.S. potential (a way to use SAE in TDDFT). The right panel of Fig. 3.57 shows the (total) ARPES obtained at this level of theory. We note, that again only the HOMO contributes.

Note, we again use the same color scale than for all previous plots. In the SAE, the ionization yield seems to be larger than in normal TDDFT and the picture appears to be closer to the experimental result. This is mainly due to the fact that the total ionization comes only from HOMO.

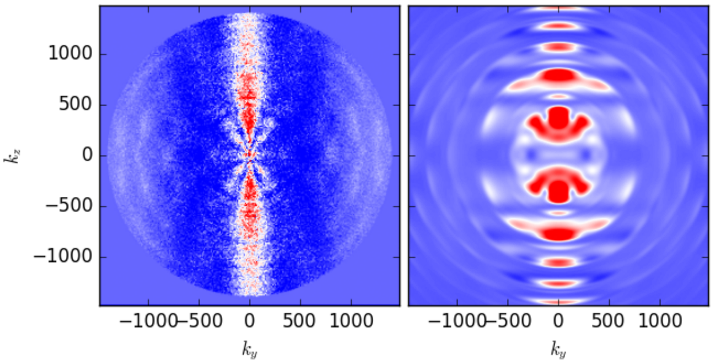

Figure 3.57: Comparison of PAD for experiment and theory on the level of SAE.

3.11 HHG OCS

In this section we investigate from the point of view of TDDFT the emission of radiation of a OCS molecule perfectly aligned. It has already been proved that the HHG spectra obtained by aligned molecules present an enhancement of the intensities of the emitted harmonics [118]. Here, the idea is to use different angle between pump and probe in order to break the symmetry and to get elliptically polarized laser, starting from a linearly polarized one.

3.11.1 Laser

We use an electric field of frequency $\omega_L = 0.0567$ a.u. with squared sinusoidal shape $f(t)$:

$$f(t) = \sin^2\left(\frac{\omega_L t}{2N_c}\right); \tag{3.6}$$

where the duration N_c is $N_c = 12$.

The laser is plotted in Fig. 3.58 and the parameters are tabulated in Tab. 3.6.

	Atomic units	Regular units
U_p	0.0749 a.u.	2.037 eV
z_p	9.609 a.u.	0.5085 nm
ω_L	0.0567 a.u.	1.550 eV
T_L	110.3 a.u.	2.670 fs
ε_0	0.03117 a.u.	$1.602 \cdot 10^8$ V/cm

Table 3.6: Laser parameters.

where U_p is the ponderomotive energy, z_p is the oscillation length or quiver length and ε_0 is the maximum intensity of the electric field.

$$\varepsilon_z = \varepsilon_{0z} f(t)\cos(\omega_L t) \tag{3.7}$$

$$\varepsilon_{0z} = \sqrt{I_0} \tag{3.8}$$

$$U_p = \frac{I_0}{4\omega_L^2}(\mathrm{a.u.}) \tag{3.9}$$

$$z_p = \frac{\varepsilon_0}{\omega_L^2}(\mathrm{a.u.}) \tag{3.10}$$

For any other quantities evaluated in this section we refer to the theory section.

3.11.2 System configuration

In Fig. 3.59 we show a representation of the system formed by OCS and the linearly polarized laser. Our idea is to break the cylindrical symmetry by varying the angle between the polarization axis of the probe laser and the molecular axis θ_L. We fix the polarization axis in $\hat{z}$-direction and we change the orientation of the molecule in the plan (XOZ).

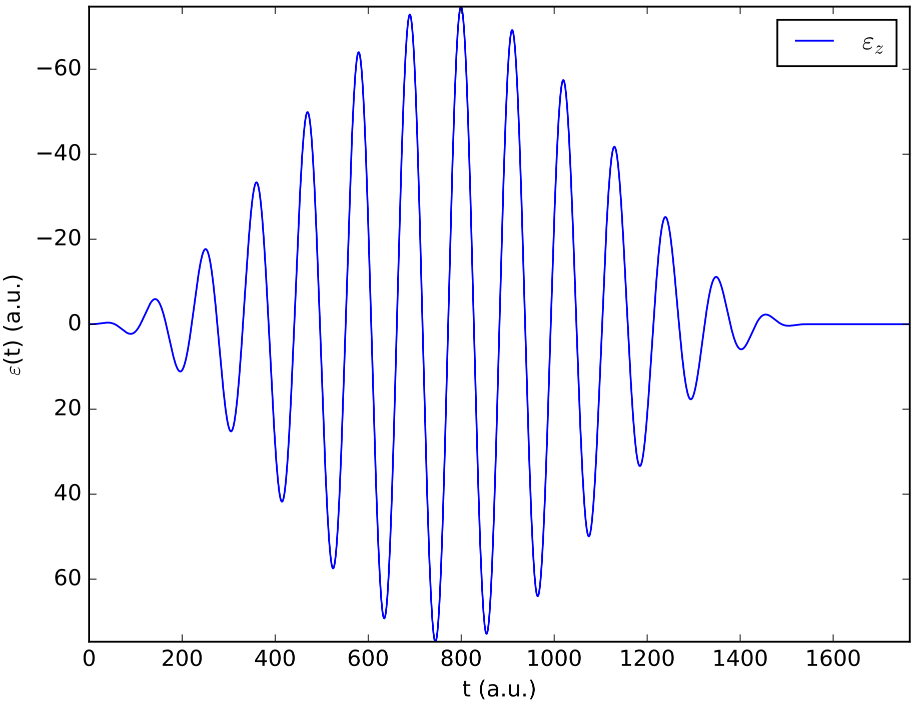

Figure 3.58: $\varepsilon_z(t)$ vs t a.u.

.

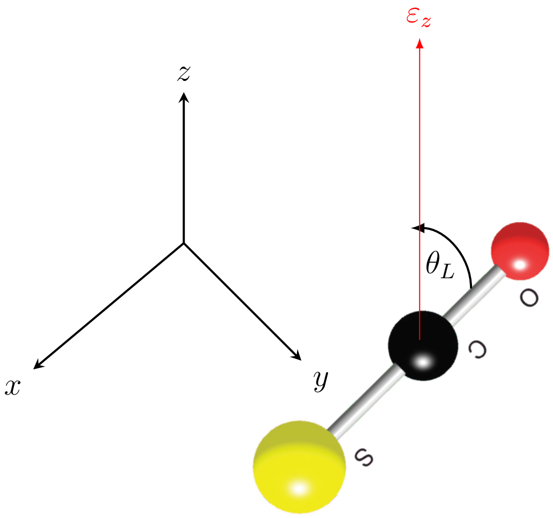

Figure 3.59: Picture of the OCS molecule driven by a linear polarized laser in the direction that forms an angle θ_L with respect the molecular axis.

3.11.3 Results

In Fig.3.60 we show the spectrum and the polarization of the emitted radiation by a OCS molecule driven by a linearly polarized laser along the z-axis, when the molecule is also along z ($\theta_L = 0$). We observe that the polarization is linear, as the polarization of the probe laser; actually, this behaviour is not surprising due to the fact that the cylindrical symmetry of the system forces the emission to be polarized along the z-axis. As expected, the spectrum shows both even and odd harmonics, because the molecule has not circular symmetry.

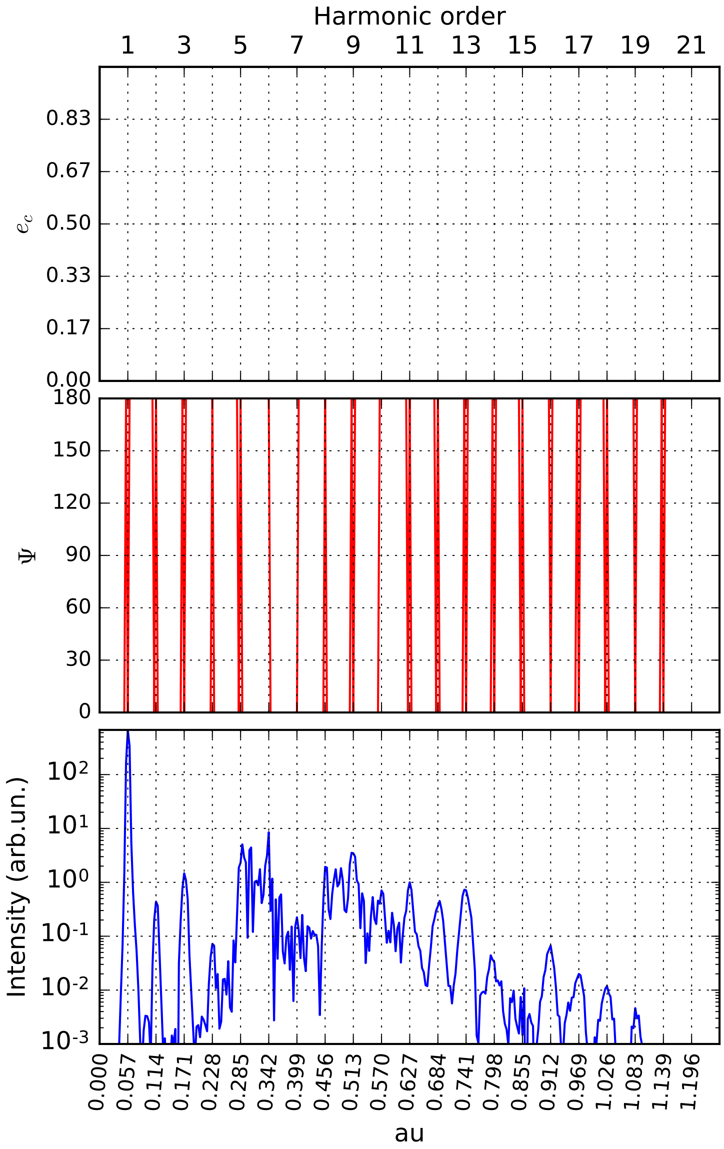

Figure 3.60: First row: e_c vs E au. Second row: Ψ ($^\circ$) vs E eV. Third row: $\frac{\mathrm{d}I(\omega)}{\mathrm{d}\omega}$ vs E a.u.. ($\theta_L = 0$, $\mathrm{d}x = 0.4$ a.u.., $L = 80$ a.u.)

Instead, the emission is elliptically polarized when the molecular axis is not aligned with the driven field, as a result of the breaking of cylindrical symmetry. This is evident in

Fig. 3.61, evaluated with $\theta_L = 35°$; particularly interesting are H6 and H11 that present a very high emission yield and that have an ellipticity greater than 0.5.

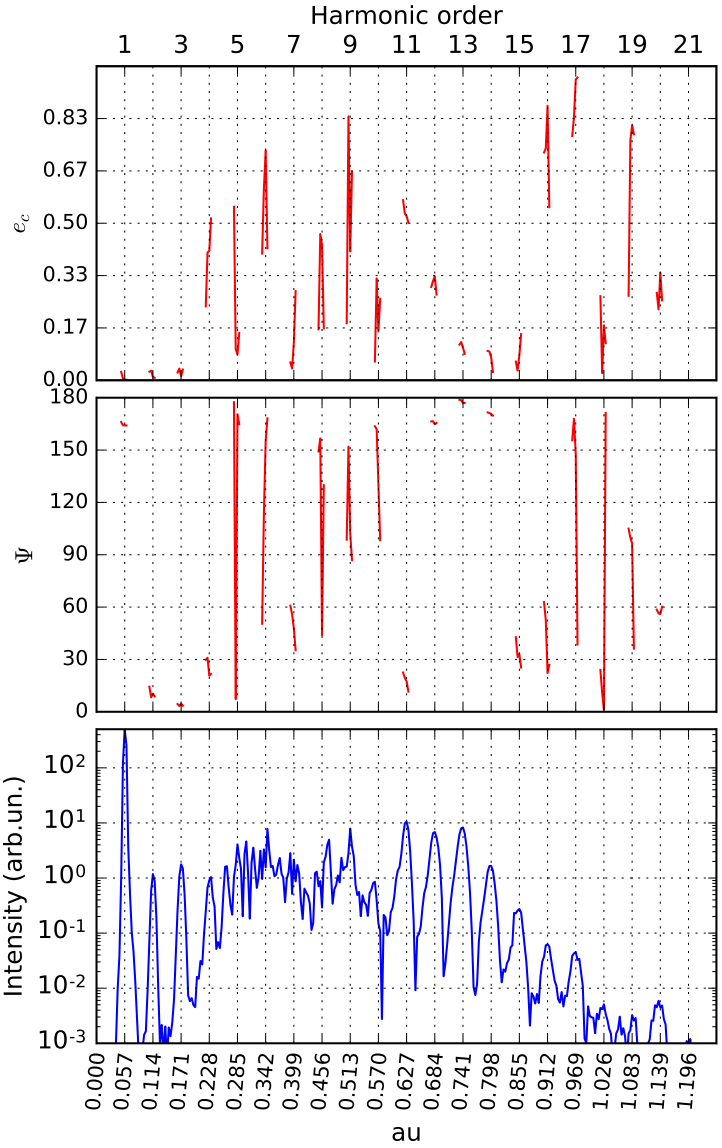

Figure 3.61: First row: e_c vs E au. Second row: Ψ (°) vs E eV. Third row: $\frac{\mathrm{d}I(\omega)}{\mathrm{d}\omega}$ vs E a.u.. ($\theta_L = 35°$, $\mathrm{d}x = 0.4$ a.u.., $L = 80$ a.u.)

As said before, the aim of this work is to obtain in the range between 15 and 30 eV significant emission with high ellipticity. For this reason, a general view of the yield and the ellipticity of the emitted harmonics by varying θ_L is shown in Fig. 3.62. The fact that H11 presents a high intensity and an ellipticity greater than 0.4 in the range from $\theta_L = 35°$ to $\theta_L = 55°$ is a nice result.

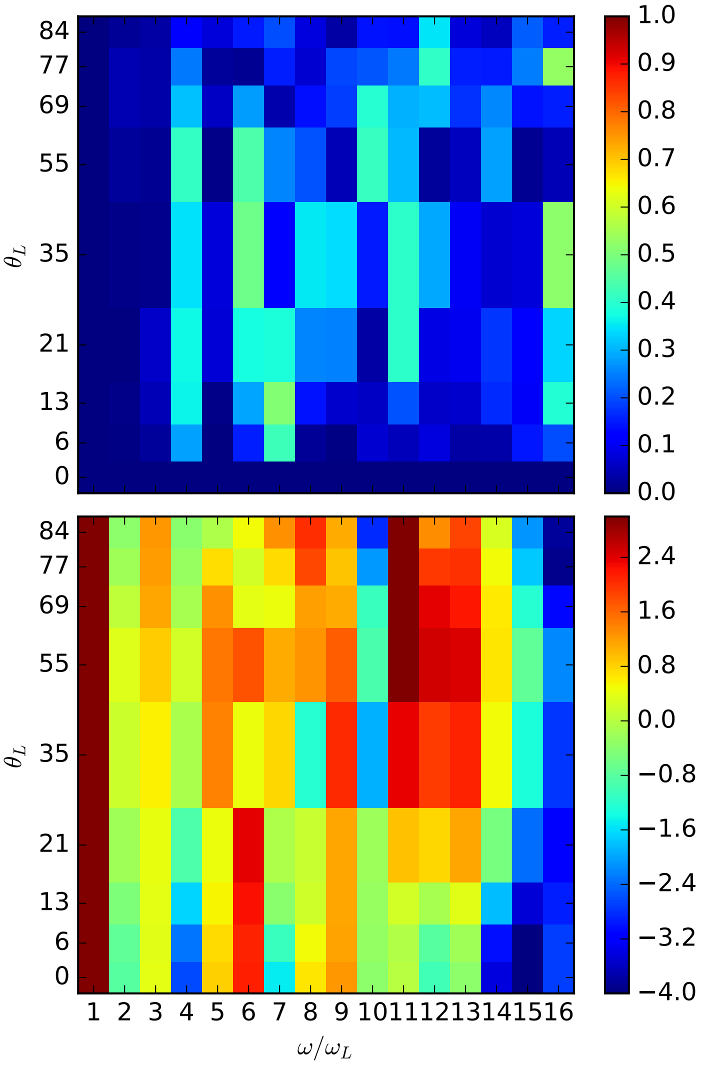

Figure 3.62: First row: e_c vs E au vs θ_L. Second row: $\frac{\mathrm{d}I(\omega)}{\mathrm{d}\omega}$ vs E au vs θ_L (°). ($\mathrm{d}x = 0.4$ a.u.., $L = 80$ a.u.)

4

Conclusion.

4.1 Overview.

As for every physics research, the scope of this work, initially, was to discover new features and to improve our knowledge of nature. Of course, as a careful reader knows at this point, our main goal was to study the possibility to develop new technologies by using some peculiar properties of matter interacting with strong laser fields. Every different targets that we probed and every different lasers that we used, were chosen for getting this goal. For that reason, we investigate several different systems, and we try to play with the symmetry of the total system (matter plus laser). The idea of this kind of control is justified by the advances in the experiments, which allows to align molecules, to control the properties of the pump laser, to fine analyze the emissions of photons or particles. Thus, in this context, it is justified the idea of looking for ways of controlling the emission. In this thesis, we mainly focused on nanorings. The peculiar properties of these systems impose that the properties of the emission mainly depends on the angular motion of the electrons. Thus by varying the angular properties of these settable emitters we modified the emitted radiation. The main issue of our work was focused on the quest for techniques that permit the control of the emission by modification of the physical parameters of laser and matter.

4.2 Classical Rings.

In Sec. 3.6 we classically studied the motion of an electron bound to rotate in a circle and at the same time driven by a linearly polarized laser field. We compared the classic results with the quantum-mechanical ones [62] and we looked for additional information about it. The main property that we studied for this part of the thesis was the Fourier power. The spectra, as found, present very different features depending on the initial parameters of the system. From a point of view, this means that we can try to set some properties of the emitted radiation by varying the initial parameters of the classic ring, on the other hand, to control a system, really sensitive to the variation of the parameters, can be really hard. We found with our classical analysis that the presence of HHG in the classical spectra (both for SQRs and plain rings) depends on the presence of the chaotic behaviour in the classical motion, and in particular the insurgence of a chaotic behaviour affects HHG. In any case, in order to fine define, the chaotic limits of our study we should conduct a deeper sampling of the initial parameters, and this could allow us to maybe find some clear relation between HHG and chaos, in any case, just looking at the literature, we can clearly see a correlation [119, 120, 25].

In this work, we showed that the TISE for a single electron in a SQRs could be rewritten as Mathieu equations [62, 48], which describes the classic parametric oscillations induced by a small non resonant excitation where the physical systems quickly become chaotic [51]. Thus, although the classic equations are very different from the Mathieu functions, the fact that both presents chaotic behaviour could be considered very interesting. Maybe, in analogy to the possibility to derive some properties of the quantum system from the study of the classical counterpart, we could think about the existence of a class of quantum chaotic problems emerging from the chaoticity of the corresponding Newton's Laws [121, 122].

Although, we state that classical chaotic systems and their quantum equivalent are correlated, it is important to note that this correlation is not, as yet, clear. In any case, we think that we were able to unveil some main aspects of the correlation between classic and quantum rings.

4.3 Quantum ring as settable HHG emitter.

As next step, we worked to the construction of a home-made nano-system, in particular we studied theoretically the possibility to control the properties of the emission by varying the confinement potential felt by an electron in the nanostructure. We studied the interaction between a SQR and a strong laser field by varying its rotational symmetry, and we found that for small changes in the potential there are important variations of the properties of the emitted radiation. Thus, we can conclude that this system is really interesting in order to realize home-made emitters which allow a fine tuning of the emission.

The choice of SQR is also motivated by the fact that the spectrum of the symmetrical case is already rich Fig. (3.15). The final part of the spectrum can be used to realize attosecond pulses. In addition, we proved that by a fine tuning of the potential, we can obtain different emission, for example, spectra with only harmonic lines. In our work, we found that is possible to increase the cutoff, but a spectrum with a large cutoff presents also a decreased resolution, in addition, a system without circular symmetry emits both even and odds harmonics, like we found for example in Fig. (3.17)

A requested figure of merit, is to product an emitter of circular polarized laser working in the 10-30 eV range. In our simulations, we were able to get in the region of $\approx 39 \rightarrow 30$ nm (27th-20th harmonics), emission with different polarizations. Thus, the idea of using SQR as emitter of circular polarized laser is not the worst one.

The designed SQR is very promising as a device which can produce finely tuned radiation, and in particular as HHG emitter. The high tunability of this system can allow the realization of very fine devices, which can be used to analyze new properties of molecules and atoms.

4.4 2D Quantum ring.

As final step, in our study of quantum rings we analyze a 2D quantum ring model, which allows the electron to be ionized. We analyze the emission of this system driven by two different incident pulses.
We probed a 2D plain ring with an unipolar pulse polarized perpendicularly to a linear polarized laser. We used the unipolar pulse to break the symmetry of the system laser + plain ring.
We found that the unipolar pulse activates a current in the plain ring, oscillating with frequency corresponding both with angular than radial transition Table 3.5. From the literature we know that the use of resonant lasers influences the emitted spectrum. Analogously, we set the laser frequency resonant with one of the transition energies which are presents in the spectrum when we drive the system with the unipolar pulse alone. By playing with the frequency and the intensity of the laser we get elliptically polarized emission up to ellipticity of $e_c = 0.2$, but the strong result is that we are able to control the frequency of the emitted radiation, by setting different resonances. Thus a 2D quantum ring is a frequency tunable elliptically polarized radiation emitter, and it is not sensible to the carrier envelope phase.
In addition, by using the Morlet transformation we studied as the emitted radiation properties changes with the time. We found large time intervals with elliptically polarized emission, also with very high e_c. As an interesting results, we see that by varying the numbers of photons of resonance the features notably change. In particular with 9 photons of resonance, instead than 5, the emission presents ellipticity different from zero for every harmonics. As remarkable achievement, the emission of H7 is maximum at $t_0 \approx 24T_L$ and the time windowed ellipticity $e_c(t_0 = 24T_L, \omega = 7\omega_L)$ is around 0.9 (see Fig. 3.36). This means that our system produces a quasi circular polarized emission at 13.14 eV, that with some filtering process can be use as probe for others systems.

4.5 CF_3I PADs

The improvements of the instrumentation in the strong field physics allow various discoveries, in particular the possibility to fine align molecules permits to study high symmetric systems. Thus, nowadays we are able to see features deriving by the symmetry of the system, and in particular we observe peculiar characteristics in the HHG spectrum and in the PAD. This part of our research is devoted to the comparison between theory and experiments by studying a top symmetric molecule, with an high dipole moment, CF_3I driven by a strong linear polarized laser field.
We observe that when the laser and the molecules are aligned there is a strong decrease in the contribution of the HOMO orbital to the PAD, this is due to the fact that the HOMO presents along the laser polarization axis a nodal plane, this reduces the contribution of HOMO to the total ionization of the system with respect the one of the antialigned case. At the contrary, HOMO-1 presents the nodal plane perpendicular

to the laser polarization axis thus the ionization from HOMO-1 is maximum in the aligned case, and we can see it in the PAD.

As we can see already in the experimental normalized difference maps, there are several features that can be uniquely assigned to the HOMO and HOMO-1. In conclusion, we reported various comparison between experiments on LIED of aligned CF_3I molecules, and by using a TDDFT method, we were able to decouple the contributions of the orbitals and then to prove that some features comes from HOMO-1 and the other from HOMO. By combining the experimental and theoretical results we are able to conclude that the PAD are influenced by the orbital of ionization, and that the final image is affected by different orbitals in different regions. This underlines the importance of a multiple orbitals method to describe the phenomenon of the electron emission from matter driven by a strong laser, and consequently shows the limits of the standard sae and one orbital approach.

4.6 OCS PADs.

The following analysis was devoted to study a molecule with an higher dipole moment than CF_3I. OCS is a top symmetric molecule that can be highly aligned.

As we found for the previous case the HOMO contribution in the aligned configuration is suppressed, actually also OCS presents a nodal plan in the laser polarization axis in the HOMO orbital. In this case the ionization from the HOMO-1 is still negligible in the energy region of the study, thus, by varying the polarization axis we clearly observed how the variation of the total ionization depends on the angle between nodal plane of HOMO and the laser polarization axis. We saw that the total ionization is maximum for the anti-aligned configuration and minimum for the aligned configuration and that it increases for the angle in the middle.

Actually, in the experiment the total ionizations for aligned and anti-aligned cases are close each other. This is due to the fact that in the experiment there is a distribution of molecules with different angles mainly aligned in one direction. Thus, the PES measured for a configuration have also contributions from a certain number of molecules with different alignment. Being the PES of the anti-aligned configuration the most intense the contribution of the molecules not perfectly aligned is negligible, at the contrary, the aligned configuration presents the less intense PES thus, the contribution of the misaligned molecules becomes very important and increases the total ionization of this latest configuration.

Thus, in order to compare the experimental aligned configuration to the theoretical one we analyzed the misalignment contribution. Another, important difference between theory and experiment is the angle in the cross-like structure in the inner part of the PAD, this angle is sensitive to the intensity of the laser, of course, the experimental intensity is a mean value of a distribution, thus in order to improve the agreement we studied the volume effects.

As an interesting issue, we found that, from a theoretical point of view,it is possible to isolate the contribution of one of the two degenerate HOMOs as shown in Fig. 3.55. In Fig. 3.56, we studied the contribution to the PES of HOMOs by varying the angle between the molecule and the laser. We observe a variation of 2 orders of magnitude for the contribution of the total ionization of HOMO 1 (in the range from $\vartheta = 0$ to

$90°$) at the contrary the contribution of HOMO 2 does not present strong variation. In conclusion, OCS allows a finer study compared to CF_3I; we were able to separate the contribution of the degenerate HOMO.

4.7 OCS HHG.

In this final part of our work, using the information previously acquired by studying the photoemission, we made a systematic study of the properties of the emitted radiation by aligned molecules. In particular, we study the radiation emitted by OCS driven by a linearly polarized laser by varying the angle θ between molecule and laser polarization axis. In this way, we change the symmetry of the system laser+molecule and thus we are able, as we know from the research about QRs, to get different characteristic of the emitted HHG spectrum.

As important result, we observed that the ellipticity of the emission depends on the angle θ. As said before, this can be understood by looking at the fact that by varying that angle we break the cylindrical symmetry, thus it can be explained in analogy with the emission of elliptically polarized light from SQRs.

At the contrary of the case of SQRs here also the symmetrical case $\theta_L = 0$ presents even and odd harmonics, this is due to the fact that only a system with circular symmetry presents exclusively odd harmonics.

OCS seems to be a very nice converter of linear polarized light in elliptical, as we can see for example at Fig. 3.61, where we saw H6 and H11 with high ellipticity and with a high yield of intensity. As said before, the range of interest in this kind of research is between 15 and 30 eV, that is the energy range of ionization of the most common molecules and atoms. For this reason, we examined in depth the effect of varying θ_L and we found as important results that H11 presents a high intensity and an ellipticity greater than 0.4, in the range from $\theta_L = 35°$ to $\theta_L = 55°$, thus maybe to have a perfect alignment is not necessary.

4.8 Summary.

In this thesis, we analyzed several aspects of the interaction between matter and really intense radiation. We worked on the possibility to control the photons emission, with the idea of finding systems which allows this control. In addition, the increased accuracy of the recent experiments allows us to understand with an high detail level the emission features.

These improvements allow us to think that any suggestions that we can do from a theoretical point of view can be used experimentally for understanding more effects and features.

Bibliography

[1] T Zuo, AD Bandrauk, and PB Corkum. Laser-induced electron diffraction: a new tool for probing ultrafast molecular dynamics. *Chemical Physics Letters*, 259(3):313 – 320, 1996. 13, 104

[2] M Lein. Attosecond probing of vibrational dynamics with high-harmonic generation. *Phys. Rev. Lett.*, 94:053004, Feb 2005. 13, 25

[3] T Kanai, S Minemoto, and H Sakai. Ellipticity dependence of high-order harmonic generation from aligned molecules. *Phys. Rev. Lett.*, 98:053002, Feb 2007. 13, 28

[4] RF Lu, PY Zhang, and KL Han. Attosecond-resolution quantum dynamics calculations for atoms and molecules in strong laser fields. *Phys. Rev. E*, 77:066701, Jun 2008. 13, 25

[5] X Zhou, Z Chen, T Morishita, A-T Le, and CD Lin. Retrieval of electron-atom scattering cross sections from laser-induced electron rescattering of atomic negative ions in intense laser fields. *Physical Review A*, 77(5):053410, 2008. 13, 17

[6] Z Chen, A-T Le, T Morishita, and CD Lin. Quantitative rescattering theory for laser-induced high-energy plateau photoelectron spectra. *Physical Review A*, 79(3):033409, 2009. 13, 27, 28, 111

[7] J Xu, Z Chen, A-T Le, and CD Lin. Self-imaging of molecules from diffraction spectra by laser-induced rescattering electrons. *Physical Review A*, 82(3):033403, 2010. 13, 27, 107, 111

[8] G Castiglia, P P Corso, D Cricchio, R Daniele, E Fiordilino, F Morales, and F Persico. High-order-harmonic generation in dimensionally reduced systems. *Physical Review A*, 88(3):033837, 2013. 13, 33

[9] G Castiglia, P P Corso, R Daniele, E Fiordilino, B Frusteri, and F Morales. The influence of the quantum nature of nuclei in high harmonic generation from h + 2 -like molecular ions. *Laser Physics*, 23(9):095301, 2013. 13, 25

[10] LV Keldysh. Ionization in the field of a strong electromagnetic wave. *Sov. Phys. JETP*, 20(5):1307–1314, 1965. 15, 17

[11] F H M Faisal. Collision of electrons with laser photons in a background potential. *Journal of Physics B: Atomic and Molecular Physics*, 6(11):L312, 1973. 16, 17

[12] PW Milonni and JR Ackerhalt. Keldysh approximation, a 2, and strong-field ionization. *Physical Review A*, 39(3):1139, 1989. 16, 17

[13] H R Reiss. Effect of an intense electromagnetic field on a weakly bound system. *Physical Review A*, 22(5):1786, 1980. 17

[14] PH Bucksbaum, M Bashkansky, and DW Schumacher. Above-threshold ionization in helium. *Phys. Rev. A*, 37:3615–3618, May 1988. 17

[15] PB Corkum, NH Burnett, and F Brunel. Above-threshold ionization in the long-wavelength limit. *Phys. Rev. Lett.*, 62:1259–1262, Mar 1989. 19

[16] JL Krause, KJ Schafer, and KC Kulander. High-order harmonic generation from atoms and ions in the high intensity regime. *Phys. Rev. Lett.*, 68:3535–3538, Jun 1992. 19

[17] U Mohideen, MH Sher, HWK Tom, GD Aumiller, OR Wood, RR Freeman, J Boker, and PH Bucksbaum. High intensity above-threshold ionization of he. *Phys. Rev. Lett.*, 71:509–512, Jul 1993. 19

[18] PB Corkum. Plasma perspective on strong field multiphoton ionization. *Physical Review Letters*, 71(13):1994, 1993. 19

[19] M Lewenstein, Ph Balcou, M Y Ivanov, A L'huillier, and PB Corkum. Theory of high-harmonic generation by low-frequency laser fields. *Physical Review A*, 49(3):2117, 1994. 20

[20] B Yang, KJ Schafer, B Walker, KC Kulander, P Agostini, and LF DiMauro. Intensity-dependent scattering rings in high order above-threshold ionization. *Phys. Rev. Lett.*, 71:3770–3773, Dec 1993. 22

[21] GG Paulus, W Nicklich, H Xu, P Lambropoulos, and H Walther. Plateau in above threshold ionization spectra. *Phys. Rev. Lett.*, 72:2851–2854, May 1994. 22

[22] G G Paulus, W Becker, W Nicklich, and H Walther. Rescattering effects in above-threshold ionization: a classical model. *Journal of Physics B: Atomic, Molecular and Optical Physics*, 27(21):L703, 1994. 22

[23] Z Chen, T Morishita, A-T Le, and CD Lin. Analysis of two-dimensional high-energy photoelectron momentum distributions in the single ionization of atoms by intense laser pulses. *Physical Review A*, 76(4):043402, 2007. 24

[24] A Giusti-Suzor, F H Mies, L F DiMauro, E Charron, and B Yang. Dynamics of h 2 + in intense laser fields. *Journal of Physics B: Atomic, Molecular and Optical Physics*, 28(3):309, 1995. 25

[25] G Castiglia, G Camiolo, PP Corso, R Daniele, E Fiordilino, and F Morales. Probing the dynamics of a molecular ion with laser pulses. *LASER PHYSICS-LAWRENCE-*, 14(9):1185–1190, 2004. 25, 130

[26] JH Posthumus. The dynamics of small molecules in intense laser fields. *Reports on Progress in Physics*, 67(5):623, 2004. 25

[27] IS Anderson, PJ Brown, JM Carpenter, G Lander, R Pynn, JM Rowe, O Schärpf, VF Sears, and BTM Willis. *International Tables for Crystallography*. Wiley Hoboken, New Jersey, New York, 2006. 27

[28] T Suzuki, S Minemoto, T Kanai, and H Sakai. Optimal control of multiphoton ionization processes in aligned i_2 molecules with time-dependent polarization pulses. *Phys. Rev. Lett.*, 92:133005, Apr 2004. 28

[29] W Boutu, S Haessler, H Merdji, P Breger, G Waters, M Stankiewicz, LJ Frasinski, R Taieb, J Caillat, A Maquet, et al. Coherent control of attosecond emission from aligned molecules. *Nature Physics*, 4(7):545, 2008. 28

[30] B Friedrich and D Herschbach. Alignment and trapping of molecules in intense laser fields. *Physical Review Letters*, 74(23):4623, 1995. 28, 118

[31] M Abramowitz, I A Stegun, et al. *Handbook of mathematical functions*, volume 1046. Dover New York, 1965. 29, 35, 38

[32] JD Jackson. *Classical electrodynamics*. AAPT, 1999. 30, 57

[33] B Sutherland. Quantum many-body problem in one dimension: Ground state. *Journal of Mathematical Physics*, 12(2):246–250, 1971. 31

[34] A.K Kerman and S.E Koonin. Hamiltonian formulation of time-dependent variational principles for the many-body system. *Annals of Physics*, 100(1):332 – 358, 1976. 31

[35] RG Parr. Density functional theory. *Annual Review of Physical Chemistry*, 34(1):631–656, 1983. 31

[36] EKU Gross and RM Dreizler. *Density functional theory*, volume 337. Springer Science & Business Media, 2013. 31

[37] F Giustino. *Materials modelling using density functional theory: properties and predictions*. Oxford University Press, 2014. 31

[38] JC Ahn, KS Kwak, BH Park, HY Kang, JY Kim, and O'Dae Kwon. Photonic quantum ring. *Physical review letters*, 82(3):536, 1999. 33

[39] H Pettersson, RJ Warburton, A Lorke, K Karrai, JP Kotthaus, JM Garcia, and PM Petroff. Excitons in self-assembled quantum ring-like structures. *Physica E: Low-dimensional Systems and Nanostructures*, 6(1-4):510–513, 2000. 33

[40] RJ Warburton, C Schäflein, D Haft, F Bickel, A Lorke, K Karrai, JM Garcia, W Schoenfeld, and PM Petroff. Optical emission from a charge-tunable quantum ring. *Nature*, 405(6789):926, 2000. 33

[41] SS Li and JB Xia. Electronic states of inas/gaas quantum ring. *Journal of Applied Physics*, 89(6):3434–3437, 2001. 33

[42] UF Keyser, S Borck, RJ Haug, M Bichler, G Abstreiter, and Werner Wegscheider. Aharonov–bohm oscillations of a tuneable quantum ring. *Semiconductor Science and Technology*, 17(5):L22, 2002. 33

[43] M Bayer, Marek Korkusinski, Pawel Hawrylak, T Gutbrod, M Michel, and A Forchel. Optical detection of the aharonov-bohm effect on a charged particle in a nanoscale quantum ring. *Physical review letters*, 90(18):186801, 2003. 33

[44] UF Keyser, C Fühner, S Borck, RJ Haug, Max Bichler, Gerhard Abstreiter, and Werner Wegscheider. Kondo effect in a few-electron quantum ring. *Physical review letters*, 90(19):196601, 2003. 33

[45] T Kuroda, T Mano, T Ochiai, S Sanguinetti, K Sakoda, G Kido, and N Koguchi. Optical transitions in quantum ring complexes. *Phys. Rev. B*, 72:205301, Nov 2005. 33

[46] D Cricchio and E Fiordilino. Harmonic generation from nanorings driven by a two-color laser field. *Laser Physics Letters*, 11(6):066002, 2014. 33

[47] D Cricchio and E Fiordilino. Wavelet analysis and hhg in nanorings: their applications in logic gates and memory mass devices. *Nanoscale*, 8:1968–1974, 2016. 33

[48] E Fiordilino and B Frusteri. Defects in quantum ring to control high-harmonic spectrum. *Laser and Particle Beams*, 35(1):126–136, 2017. 34, 77, 130

[49] É Mathieu. Mémoire sur le mouvement vibratoire d'une membrane de forme elliptique. *Journal de mathématiques pures et appliquées*, 13:137–203, 1868. 35

[50] PM Morse and H Feshbach. Methods of theoretical physics. *International Series in Pure and Applied Physics, New York: McGraw-Hill, 1953*, 2, 1953. 35

[51] AH Nayfeh and DT Mook. *Nonlinear oscillators*. 1979. 35, 130

[52] IS Gradshteyn, IM Ryzhik, Alan Jeffrey, YV Geronimus, MY Tseytlin, and YC Fung. *Table of Integrals, Series, and Products*. American Society of Mechanical Engineers, 1981. 35

[53] J Killingbeck. Hill determinants and 1/n theory. *Journal of Physics A: Mathematical and General*, 18(16):L1025, 1985. 35

[54] L Ruby. Applications of the mathieu equation. *American Journal of Physics*, 64(1):39–44, 1996. 35, 38

[55] GB Arfken and HJ Weber. *Mathematical Methods For Physicists International Edition*. Academic press, 2005. 35

[56] W Magnus et al. Infinite determinants associated with hill's equation. *Pacific J. Math*, 5:941–951, 1955. 35, 38

[57] W Magnus and Abe Shenitzer. *Hill's Equation. Part I. General Theory*. Courant Institute of Mathematical Sciences, New York University, 1957. 35, 38

[58] R Denk. Hill's equation systems and infinite determinants. *Mathematische Nachrichten*, 175(1):47–60, 1995. 35, 38

[59] L Chaos-Cador and E Ley-Koo. Mathieu functions revisited: matrix evaluation and generating functions. *Revista mexicana de física*, 48(1):67–75, 2002. 35, 38

[60] JC Gutiérrez-Vega, RM Rodrıguez-Dagnino, MA Meneses-Nava, and S Chávez-Cerda. Mathieu functions, a visual approach. *American Journal of Physics*, 71(3):233–242, 2003. 35, 38

[61] FWJ Olver, DW Lozier, RF Boisvert, and CW Clark. *NIST handbook of mathematical functions, US Department of Commerce, National Institute of Standards and Technology*. Washington, DC, 2010. 40

[62] G Castiglia, PP Corso, U De Giovannini, E Fiordilino, and B Frusteri. Laser driven structured quantum rings. *Journal of Physics B: Atomic, Molecular and Optical Physics*, 48(11):115401, 2015. 40, 50, 72, 80, 129, 130

[63] P Hohenberg and W Kohn. Inhomogeneous electron gas. *Physical review*, 136(3B):B864, 1964. 42

[64] TL Gilbert. Hohenberg-kohn theorem for nonlocal external potentials. *Physical Review B*, 12(6):2111, 1975. 42

[65] ES Kryachko. Hohenberg-kohn theorem. *International Journal of Quantum Chemistry*, 18(4):1029–1035, 1980. 42

[66] H Englisch and R Englisch. Hohenberg-kohn theorem and non-v-representable densities. *Physica A: Statistical Mechanics and its Applications*, 121(1-2):253–268, 1983. 42

[67] PW Ayers, S Golden, and M Levy. Generalizations of the hohenberg-kohn theorem: I. legendre transform constructions of variational principles for density matrices and electron distribution functions. *The Journal of chemical physics*, 124(5):054101, 2006. 42

[68] R Gaudoin and K Burke. Lack of hohenberg-kohn theorem for excited states. *Physical review letters*, 93(17):173001, 2004. 42

[69] W Kohn and LJ Sham. Self-consistent equations including exchange and correlation effects. *Physical review*, 140(4A):A1133, 1965. 44

[70] Q Zhao, RC Morrison, and RG Parr. From electron densities to kohn-sham kinetic energies, orbital energies, exchange-correlation potentials, and exchange-correlation energies. *Physical Review A*, 50(3):2138, 1994. 44

[71] A Seidl, A Görling, P Vogl, JA Majewski, and M Levy. Generalized kohn-sham schemes and the band-gap problem. *Physical Review B*, 53(7):3764, 1996. 44

[72] TA Wesolowski and J Weber. Kohn-sham equations with constrained electron density: an iterative evaluation of the ground-state electron density of interacting molecules. *Chemical physics letters*, 248(1-2):71–76, 1996. 44

[73] AC Scheiner, J Baker, and JW Andzelm. Molecular energies and properties from density functional theory: Exploring basis set dependence of kohn-sham equation using several density functionals. *Journal of computational chemistry*, 18(6):775–795, 1997. 44

[74] JP Perdew and A Zunger. Self-interaction correction to density-functional approximations for many-electron systems. *Physical Review B*, 23(10):5048, 1981. 46

[75] DC Langreth and MJ Mehl. Beyond the local-density approximation in calculations of ground-state electronic properties. *Physical Review B*, 28(4):1809, 1983. 46

[76] JP Perdew. Unified theory of exchange and correlation beyond the local density approximation. *Electronic structure of solids' 91*, 11, 1991. 46

[77] AD Becke. A new mixing of hartree–fock and local density-functional theories. *The Journal of chemical physics*, 98(2):1372–1377, 1993. 46

[78] JMT Thompson and HB Stewart. *Nonlinear dynamics and chaos*. John Wiley & Sons, 2002. 50, 72

[79] E Runge and EKU Gross. Density-functional theory for time-dependent systems. *Physical Review Letters*, 52(12):997, 1984. 51

[80] R van Leeuwen. Beyond the runge-gross theorem. *Time-Dependent Density Functional Theory*, pages 17–31, 2006. 54

[81] M AL Marques, N T Maitra, FMS Nogueira, EKU Gross, and A Rubio. *Fundamentals of time-dependent density functional theory*, volume 837. Springer Science & Business Media, 2012. 54

[82] M Born and E Wolf. *Principles of optics: electromagnetic theory of propagation, interference and diffraction of light*. Elsevier, 2013. 57, 58

[83] CK Chui. *An introduction to wavelets.*, volume 1. Academic press, Boston, 2014. 58

[84] S De Luca and E Fiordilino. Wavelet temporal profile of high-order harmonics emitted by a two-level atom in the presence of a laser pulse. *Journal of Physics B: Atomic, Molecular and Optical Physics*, 29(14):3277, 1996. 58

[85] L Tao and A Scrinzi. Photo-electron momentum spectra from minimal volumes: the time-dependent surface flux method. *New Journal of Physics*, 14(1):013021, 2012. 58

[86] V Mosert and D Bauer. Photoelectron spectra with qprop and t-surff. *Computer Physics Communications*, 207:452–463, 2016. 58

[87] P Wopperer, U De Giovannini, and A Rubio. Efficient and accurate modeling of electron photoemission in nanostructures with tddft. *The European Physical Journal B*, 90(3):51, 2017. 58, 59

[88] A Pohl, PG Reinhard, and E Suraud. Towards single-particle spectroscopy of small metal clusters. *Physical review letters*, 84(22):5090, 2000. 59

[89] U De Giovannini, D Varsano, MAL Marques, H Appel, EKU Gross, and A Rubio. Ab initio angle-and energy-resolved photoelectron spectroscopy with time-dependent density-functional theory. *Physical Review A*, 85(6):062515, 2012. 59, 108

[90] PM Dinh, P Romaniello, PG Reinhard, and E Suraud. Calculation of photoelectron spectra: A mean-field-based scheme. *Physical Review A*, 87(3):032514, 2013. 59

[91] G Castiglia, PP Corso, D Cricchio, U De Giovannini, B Frusteri, and E Fiordilino. Classical chaos and harmonic generation in laser driven nanorings. *Journal of Physics B: Atomic, Molecular and Optical Physics*, 49(24):245601, 2016. 72, 77, 80

[92] H Goldstein, C Poole, and J Safko. *Classical mechanics*. AAPT, 2002. 72

[93] V Averbukh, N Moiseyev, B Mirbach, and HJ Korsch. Dynamical tunneling through a chaotic region. *Zeitschrift für Physik D Atoms, Molecules and Clusters*, 35(4):247–256, 1995. 73

[94] F Krecinic, P Wopperer, B Frusteri, F Brauße, J-G Brisset, U De Giovannini, A Rubio, A Rouzée, and MJJ Vrakking. Multiple orbital effects in laser-induced electron diffraction of aligned molecules. *under review: physical review letters*, 2017. 73, 104

[95] A Trabattoni, S Trippel, U De Giovannini, J F Olivieri, J Wiese, T Mullins, A Rouzée, S-K Son, B Frusteri, A Rubio, and J Küpper. Setting the clock of photoelectron emission through molecular alignment. *under consideration: Nature*, 2017. 73, 115

[96] T Millack and A Maquet. Hyper-raman lines produced during high harmonic generation. *Journal of Modern Optics*, 40(11):2161–2171, 1993. 73

[97] A Di Piazza and E Fiordilino. Why hyper-raman lines are absent in high-order harmonic generation. *Physical Review A*, 64(1):013802, 2001. 73

[98] A Di Piazza, E Fiordilino, and MH Mittleman. Pulse shape control of the spectrum emitted by a two level atom. *Journal of Physics B: Atomic, Molecular and Optical Physics*, 34(18):3655, 2001. 73

[99] RF Lu, HX He, YH Guo, and KL Han. Theoretical study of single attosecond pulse generation with a three-colour laser field. *J. Phys. B-At. Mol. Opt.*, 42(22):225601, 2009. 84

[100] F Krausz and M Ivanov. Attosecond physics. *Rev. Mod. Phys.*, 81(1):163, 2009. 84

[101] A Ferré, C Handschin, M Dumergue, F Burgy, A Comby, D Descamps, B Fabre, GA Garcia, R Géneaux, L Merceron, et al. A table-top ultrashort light source in the extreme ultraviolet for circular dichroism experiments. *Nature Photonics*, 9(2):93–98, 2015. 85, 98

[102] G Orlando, PP Corso, E Fiordilino, and F Persico. Generation of isolated attosecond pulses using unipolar and laser fields. *Journal of Modern Optics*, 56(16):1761–1767, 2009. 95

[103] Y Pan, S-F Zhao, and X-X Zhou. Generation of isolated sub-40-as pulses from gas-phase co molecules using an intense few-cycle chirped laser and a unipolar pulse. *Physical Review A*, 87(3):035805, 2013. 95

[104] L Feng and H Liu. Attosecond extreme ultraviolet generation in cluster by using spatially inhomogeneous field. *Physics of Plasmas*, 22(1):013107, 2015. 95

[105] FX Kärtner, F Ahr, A-L Calendron, H Çankaya, S Carbajo, G Chang, G Cirmi, K Dörner, U Dorda, A Fallahi, et al. Axsis: exploring the frontiers in attosecond x-ray science, imaging and spectroscopy. *Nuclear Instruments and Methods in Physics Research Section A: Accelerators, Spectrometers, Detectors and Associated Equipment*, 829:24–29, 2016. 95

[106] RM Arkhipov, AV Pakhomov, IV Babushkin, MV Arkhipov, Yu A Tolmachev, and NN Rosanov. Generation of unipolar pulses in a circular raman-active medium excited by few-cycle optical pulses. *JOSA B*, 33(12):2518–2524, 2016. 95

[107] AV Pakhomov, RM Arkhipov, IV Babushkin, MV Arkhipov, Yu A Tolmachev, and NN Rosanov. All-optical control of unipolar pulse generation in a resonant medium with nonlinear field coupling. *Physical Review A*, 95(1):013804, 2017. 95

[108] ATJB Eppink and DH Parker. Velocity map imaging of ions and electrons using electrostatic lenses: Application in photoelectron and photofragment ion imaging of molecular oxygen. *Review of Scientific Instruments*, 68(9):3477–3484, 1997. 104

[109] GA Garcia, L Nahon, and I Powis. Two-dimensional charged particle image inversion using a polar basis function expansion. *Review of Scientific Instruments*, 75(11):4989–4996, 2004. 105

[110] T Seideman. Revival structure of aligned rotational wave packets. *Physical Review Letters*, 83(24):4971, 1999. 105

[111] F Rosca-Pruna and MJJ Vrakking. Experimental observation of revival structures in picosecond laser-induced alignment of i 2. *Physical Review Letters*, 87(15):153902, 2001. 105

[112] M Meckel, D Comtois, D Zeidler, A Staudte, D Pavičić, HC Bandulet, H Pépin, JC Kieffer, R Dörner, DM Villeneuve, et al. Laser-induced electron tunneling and diffraction. *Science*, 320(5882):1478–1482, 2008. 107

[113] L Holmegaard, JL Hansen, L Kalhøj, SL Kragh, H Stapelfeldt, F Filsinger, J Küpper, G Meijer, D Dimitrovski, M Abu-Samha, et al. Photoelectron angular distributions from strong-field ionization of oriented molecules. *Nature Physics*, 6(6):428–432, 2010. 107

[114] AE Boguslavskiy, J Mikosch, A Gijsbertsen, M Spanner, S Patchkovskii, N Gador, MJJ Vrakking, and A Stolow. The multielectron ionization dynamics underlying attosecond strong-field spectroscopies. *Science*, 335(6074):1336–1340, 2012. 108

[115] O Smirnova, Y Mairesse, S Patchkovskii, N Dudovich, D Villeneuve, P Corkum, and MY Ivanov. High harmonic interferometry of multi-electron dynamics in molecules. *Nature*, 460(7258):972–977, 2009. 108

[116] M Spanner, O Smirnova, PB Corkum, and MY Ivanov. Reading diffraction images in strong field ionization of diatomic molecules. *Journal of Physics B: Atomic, Molecular and Optical Physics*, 37(12):L243, 2004. 111

[117] F Salvat, A Jablonski, and CJ Powell. Elsepa—dirac partial-wave calculation of elastic scattering of electrons and positrons by atoms, positive ions and molecules. *Computer physics communications*, 165(2):157–190, 2005. 111

[118] R Velotta, N Hay, MB Mason, M Castillejo, and JP Marangos. High-order harmonic generation in aligned molecules. *Phys. Rev. Lett.*, 87:183901, Oct 2001. 123

[119] E Fiordilino and V Miceli. Laser pulse shape effects in harmonic generation from a two-level atom. *Journal of Modern Optics*, 41(7):1415–1426, 1994. 130

[120] E Fiordilino, F Morales, and R Daniele. Phase control of the harmonic yield in a two color laser driven two level atom. *LASER PHYSICS-LAWRENCE-*, 10(1):111–115, 2000. 130

[121] JNL Connor, T Uzer, RA Marcus, and AD Smith. Eigenvalues of the schrödinger equation for a periodic potential with nonperiodic boundary conditions: A uniform semiclassical analysis. *The Journal of chemical physics*, 80(10):5095–5106, 1984. 130

[122] JC Gutiérrez-Vega, RM Rodrıguez-Dagnino, MA Meneses-Nava, and S Chávez-Cerda. Mathieu functions, a visual approach. *American Journal of Physics*, 71(3):233–242, 2003. 130